University of Pisa

"Galileo Galilei" Graduate School

Applied Physics

Ph.D. Thesis

Excited State Dynamics of Individual Single–Walled Carbon Nanotubes

Hayk Harutyunyan

Advisors: Prof. Dr. Maria Allegrini (University of Pisa)
Prof. Dr. Achim Hartschuh (University of Munich)

February, 2009

Contents

Acknowledgements

This work would be impossible to accomplish without support and contribution of many people. First of all, I thank my co–supervisor Prof. Maria Allegrini for giving me this opportunity to work in the field of nanotechnology, for her support and many valuable advises. Next, I would like to thank my second co–supervisor from LMU, Prof. Achim Hartschuh, who hosted me in Munich for nearly the half of the period of my PhD studies. Our numerous discussions, his continuous support and endless scientific enthusiasm that inspired me many times, were crucial for the completion of this thesis. I express my appreciation to Prof. Francesco Pegoraro for a very well organized G.Galilei graduate school and to Prof. Francesco Fuso for his kind readiness to be helpful every time when his support was needed.

I thank also my first scientific advisor Prof. Tigran Kurtikyan from MSRC, Yerevan, for helping me with my first steps in science.

Further I would like to thank the whole Hartschuh group at the University of Munich for a very nice scientific atmosphere and for all the (mega)liters of the Bavarian beer we had together. Particularly, I am very thankful to Tobias Gokus for sharing with me all the moments of success and failure in the lab, to Carsten Georgi for many intersecting and stimulating discussions and to Nicolai Hartmann for the help with the sample preparation. I would also like to thank Dr. Cinzia Casiraghi, Free University of Berlin, for the joint work on graphene and for encouraging me many times.

I am very much indebted to all of my friends in Yerevan, Pisa, Munich and all over the Europe. Without you, guys, it would be much more difficult

to carry on during the last three years.

My very special thanks are due to Dr. Grigor Ghazaryan, who was always there for me right from the very beginning of this long journey.

And finally, I would like to express my gratitude to my family. I thank my sister for being a good friend, my father for teaching me "the difference between knowing the name of something and actually knowing something", my mother for always cheering me up and all of them for their love.

Chapter 1

Introduction

An ideal carbon nanotube can be considered as rolled-up sheet of 2D graphite (graphene). Hollow, seamless cylinders formed as a result of this wrapping possess many unique properties owing to their quasi 1–dimensional structure and exceptional properties of carbon–based materials. Their discovery by Iijima in early 90s [1, 2] prompted extensive and fascinating research in this new area of nanotechnology in an attempt to reveal all the fundamental properties and making a way for new promising applications.

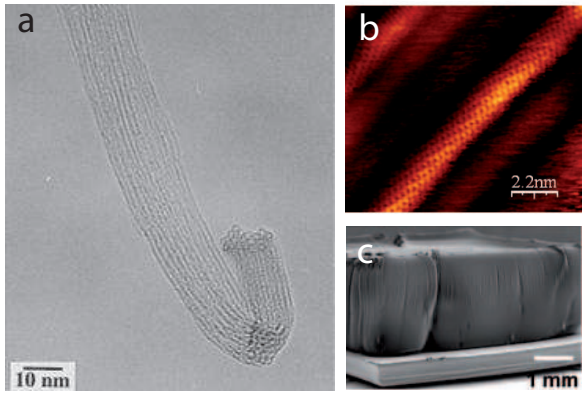

Figure 1.1: (a)TEM image of Single-walled carbon nanotube bundle, (b) STM image of an individual SWNT where single atoms can be identified and the chirality of the nanotube can be determined, (c) SEM image of milimeter long nanotube forest (from [3]).

Depending on the growth technique carbon nanotubes can be single–walled (SWNT) or multi–walled (MWNT) containing several coaxial SWNTs with common axis and increasing diameter. Single–walled carbon nanotubes typically have diameters in the range of 0,7– ∼3nm and therefore can be regarded as single molecules but on the other hand they can have macroscopical lengths reaching for some samples up to several milliliters [3]. As a result some properties of carbon nanotubes can be explained within the model of a macroscopic homogeneous cylinder while others, e.g. electronic properties, are heavily influenced by the way the graphene monolayer is rolled up. The resulting macro and micro(nano) properties of these materials are indeed outstanding.

Mechanical properties of CNTs are a result of strong sp^2 bonds of the graphene honeycomb lattice. Though having light weight they can sustain extremely high tension force up to 130 GPa compared to steel at 5 GPa, which makes them the strongest material known. Variety of schemes have been proposed to make use of these extraordinary properties ranging from everyday items like clothes and sports gear to combat jackets and space elevators. They are also highly flexible, even at low temperature, therefore these compounds are potentially suitable for applications in composite materials that need anisotropic properties such as AFM or STM tips.

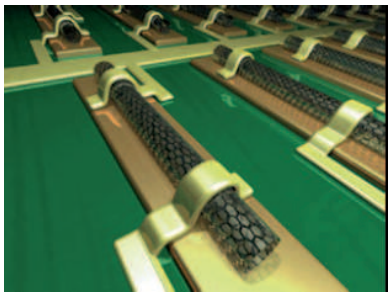

Figure 1.2: Schematics of CNT electronic circuit.

Chemical reactivity of carbon nanotubes is based on the properties of graphene sheet and is enhanced by curvature effects of CNT's surface. Pi–orbital mismatch owing to increased curvature can result in higher reactivity

for small diameter tubes. Covalent chemical modification of either sidewalls or end caps has shown to be possible. For example, the solubility of CNTs in different solvents can be controlled in this way. Chemical functionalization of the CNTs makes it possible to tailor macromolecular structures trough attachment of organic functional groups on the surface of nanotubes. On the other hand wrapping of the tubes by other polymers mediated by van der Waals interactions opens a way to investigate the effect of different dielectric environments on the electronic structure of the CNTs.

Depending on the angle of wrapping chiral vector carbon nanotubes can be either semiconductors or metals. As it will be shown later, differences in conducting properties are caused by the molecular structure that results in a different band structure and thus a different band gap. They can sustain high current densities, 1000 times higher than copper wires. This makes CNTs an ideal candidate for nanoscale electronic circuits, field emission devices or single molecule transistors (Fig. 1.2, 1.3) [4].

Figure 1.3: Field emission flat panel based on CNTs from Samsung.

The discovery of photoluminescence (PL) from CNTs opened up new perspectives for their application as narrow band emitters or biosensors [4, 5, 6, 7]. The PL intensity and the emission wavelength is shown to be sensitive to the local environment. Other applications include the use of CNTs in energy storage and energy conversion devices, actuators, electronic devices, production of nanorods using CNTs as reacting templates, catalysis, and hydrogen storage media [4].

However, many of these applications require the full knowledge of the electronic processes and interactions of the nanotubes. While the extensive research during the last 15 years have answered to many intriguing questions there are still some important gaps in our understanding of these systems. One of them is the exact mechanism governing the excited state dynamics of the carbon nanotubes. It has been established that elementary excitations in carbon nanotubes constitute strongly bound excitons and is commonly agreed that their relaxation to the ground state is dominated by non–radiative decay channels [8, 9]. Nevertheless, the exact mechanism of this non–radiative relaxation is still a matter of debate.

In this work we tried to shed light on this issue by combining the photoluminescence (PL) spectroscopy with the time–resolved PL studies from *single* carbon nanotubes at room temperature. To understand the behavior of the excitations in SWNTs a profound knowledge of their electronic structure is needed. We devote Chapter 2 to the review of electronic and optical properties of the nanotubes. First, in the framework of free carrier approximation the Brillouin zone and the band structure of the nanotubes is constructed based on the graphene structure. Second, it is shown how the reduced dimensionality of the system and its unique and symmetry properties give rise to strongly bound excitonic states with different optical properties. And last, the existing literature on the research of excited state dynamics, including theoretical and experimental works using different methods and samples, is reviewed. In Chapter 3 the description of the experimental setup of confocal microscopy for investigating single molecules is given along with a brief explanation of the time–resolved PL measurement method. In Chapter 4 we present the measurements of the exciton lifetimes in single carbon nanotubes at room temperature for the first time. The extremely low quantum yield (QY) of the nanotubes ($\sim 10^{-3}$)is one of the main difficulties hindering the experimental investigation of their emission properties on a "single molecule" level where usually QY values orders of magnitude larger are required ($\sim 10\%$). However, we succeeded in obtaining good signal to noise

ratio by optimizing the components of the confocal experimental setup. We find that unlike many other fluorescent materials the excited state in the carbon nanotubes is depopulated by non-radiative relaxation channels. Our experiments show how the local phonon modes and the nanotube length affect this radiationless relaxation of the exciton. The correlated electron–hole pairs in carbon nanotubes as all the excited systems have selection rules for a photon emission imposed on them by quantum mechanics and the symmetry of their host lattice structure. In Chapter 5 by locally changing the electronic structure of the nanotube we show how some of this selection rules can be relaxed. For the first time, we report on the observation of an intersystem crossing and a triplet state emission in carbon nanotubes.

Chapter 2

Properties of Carbon Nanotubes

2.1 Geometry and Nomenclature

In the classification of the well-known carbon allotropes regarding their dimensionality, 1D carbon nanotubes can be placed after the sp^3 bonded three–dimensional diamond structures and the individual two–dimensional layers of graphite, thus closing the gap between the latter and quasi zero–dimensional Fullerenes [10]. As mentioned above the ideal SWNT can be described as a rolled up cylinder of graphene sheet. As there are infinitely many ways to wrap the hexagonal honeycomb lattice with respect to its basis vectors the resulting variety of nanotube species will also be different. Due to the close similarity of the microscopic geometrical structure of the CNTs with the graphene the lattice vectors of the latter are used to label the tube structures. Each SWNT is specified by the chiral vector

$$\mathbf{C}_h = n\mathbf{a}_1 + m\mathbf{a}_2 = (n, m) \tag{2.1}$$

which is often described by the pair of indices (n, m) that denote the number of unit vectors $n\mathbf{a}_1$ and $m\mathbf{a}_2$ in the hexagonal honeycomb lattice contained in the vector $\mathbf{C}_h$. The graphene sheet is rolled up in such a way

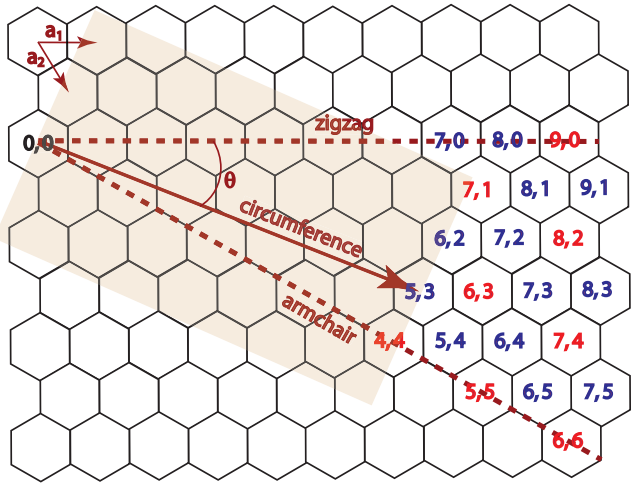

Figure 2.1: Graphene honeycomb lattice and its wrapping into carbon nanotube. If rolled-up, the shaded area would correspond to a (5,3) nanotube. a_1 and a_2 denote the graphene lattice vectors and chiral angle θ determines the structure of the nanotube. Chiral indexes indicated in red correspond to metallic tubes, in blue to semiconducting tubes.

that the chiral vector becomes the circumference of the nanotube. The nanotubes are uniquely described by this vector and many of their fundamental properties like electronic band structure or spatial symmetry group vary dramatically with their chiral vector even for tubes with similar diameter and direction of the vector. As shown in Fig. 2.1, the chiral vector $\mathbf{C}_h$ makes an angle θ, called the chiral angle, with the so-called zigzag or $\mathbf{a}_1$ direction. The chiral angle θ can be calculated from

$$\theta = \arccos \frac{\mathbf{a}_1 * \mathbf{C}_h}{|\mathbf{a}_1| * |\mathbf{C}_h|} = \arccos \frac{n + m/2}{\sqrt{n^2 + nm + m^2}} \tag{2.2}$$

Thus, not only tubes with different diameters can be designed but also the orientation of the carbon chains with respect to the cylinder axis can vary, resulting in three groups of nanotube structures Fig. 2.2: (i) armchair

tubes, with carbon atom chains parallel to cylinder axis $\theta = 0°$, (ii) zigzag tubes with chiral angle 30° and (iii) third group with $\theta \in (0° - 30°)$ called chiral tubes. For the structures belonging to first two achiral groups a mirror plane exists in contrast to the third one where mirror symmetry is removed and respective tubes form optical enantiomers.

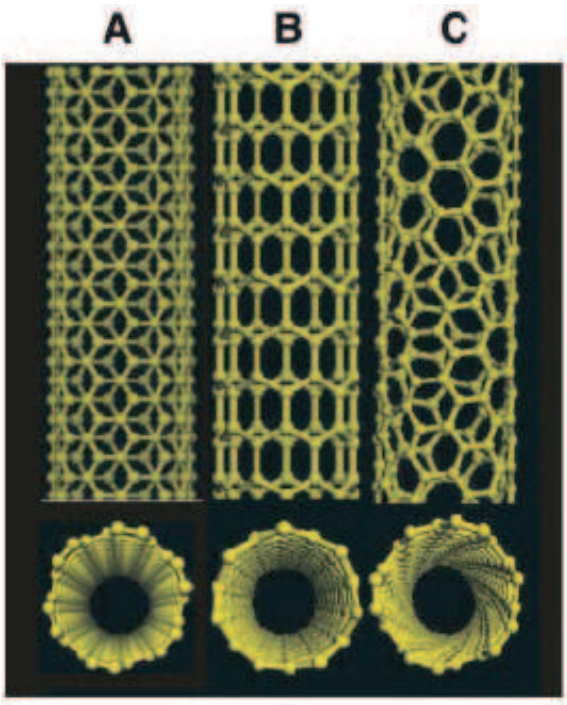

Figure 2.2: Three groups of nanotube structures. (a) armchair tube, (b) zigzag tube, (c) chiral tube from [11].

All the structural parameters of the nanotubes like diameter, unit cell and also the size and shape of the Brillouin zone are determined by the chiral vector. The diameter of the tube can be computed from the length of the $\mathbf{C}_h$:

$$d = \frac{|\mathbf{C}_h|}{\pi} = \frac{a_0}{\pi}\sqrt{n^2 + nm + m^2} \tag{2.3}$$

where $a_0 = 2,461\mathring{A}$ is the length of the basis vectors.

Raman spectroscopy is one of the powerful tools to verify the structure of the material. As we claim that the CNTs have a structure that is in

many aspects closely related to the structure of graphene, it is natural to expect that the Raman spectrum of CNTs should have similarities with the graphene spectrum.

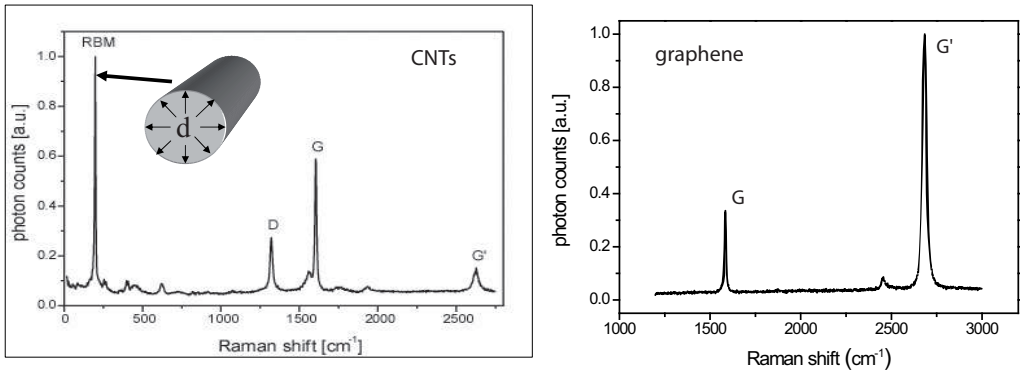

Figure 2.3: Typical Raman spectrum of SWNTs showing the most prominent first order D and G mode and the second order G' mode (left panel). The diameter dependent Radial Breathing Mode characteristic for carbon nanotubes is indicated by an arrow. The spectrum of the graphene monolayer (left panel), from [12]

As it is shown in Fig. 2.3 this is, indeed, the case. The main difference is the appearance of a new mode at low frequencies called Radial Breathing Mode (RBM). As the name of the band indicates the phonon mode associated with it could not be realized in the case of carbon sheets and it is a specific, diameter dependant signature of carbon nanotubes. Although one would expect a large number of phonon modes in the Raman spectrum of carbon nanotubes due to the confinement, there are in fact only three major bands in the first-order spectrum. This is a consequence of the high symmetry of the nanotube, leading to selection rules that prohibit most of the phonon modes in the Raman process. Because of the small mass of the carbon atoms combined with strong carbon-carbon bonds, the phonon frequencies are much larger than what is typically observed in semiconductors like GaAs or Si. Besides the RBM mode around 200 cm^{-1}, the strongest Raman modes are the so called D mode (1350 cm^{-1}) associated with the large wave vector longitudinal optical (LO) and inplane transverse optical (iTO) phonons and the

high-energy G modes (∼1600 cm^{-1}), the most prominent mode of graphite associated with zero–momentum LO and TO phonons [13, 14]. Because of their large momentum the D modes cannot be excited with a photon unless a defect site in the structure of the nanotube is present to elastically scatter back the phonon to match the momentum conservation law. Thus, as it will be discussed in Chapter 5, the intensity of the D mode is a direct measure of a defect concentration in the tube. The most prominent second order mode in nanotubes is the overtone of the D mode, the so called G' (or alternatively 2D) mode at ∼2600 cm^{-1}.

2.2 Electronic Structure

Electronic properties of nanotubes are also determined by their chiral vector. Depending on the values of n,m indexes the SWNT can be either metallic or semiconducting [15, 16]. Moreover, as it will be shown later in this section the energy gap of the tubes can be tuned by changing their diameters [17]. This is one of the most remarkable properties of carbon nanotubes which makes them promising candidates for nanoscale electronics. The conduction properties of CNTs are governed by the following simple clauses:

$$\upsilon = n\text{-}m = 3j \rightarrow \text{metallic} \qquad \upsilon = n\text{-}m \neq 3j \rightarrow \text{semiconducting}, \qquad j \in \boldsymbol{N}$$

If the difference of n and m is a multiple of three, then the tube is metallic, otherwise it is semiconducting. Thus, all SWNTs belonging to the armchair group are metallic. In general, from all theoretically possible SWNT structures one third will be metallic while two third will possess semiconducting properties(Fig. 2.1).

The electronic characteristics of the SWNTs, in particular the 1D joint density of states (JDOS) and its van Hove singularities (vHs), are fundamental for the occurrence of such optical phenomena like absorption, photoluminescence and resonance Raman effect. The electronic band structure of the SWNTs, and the special electronic and vibrational characteristics resulting

from it, are a direct consequence of the geometry of the SWNTs. In the previous section the geometrical characteristics of the SWNTs were derived from the graphite lattice structure. Now, in order to understand the SWNTs' band structure in more detail it is useful to consider first the electronic properties of a graphene sheet. Afterwards the 1D energy dispersion relation for SWNTs can be obtained on the basis of graphene's 2D dispersion relation.

Graphite consists of layers of hexagonally arranged sp^2-hybridized carbon atoms. While inter–layer interaction is due to weak van der Waals forces, within the individual layers each carbon atom is covalently bonded with its three neighboring atoms through one $\sigma-$ and one $\pi-$ bonds.

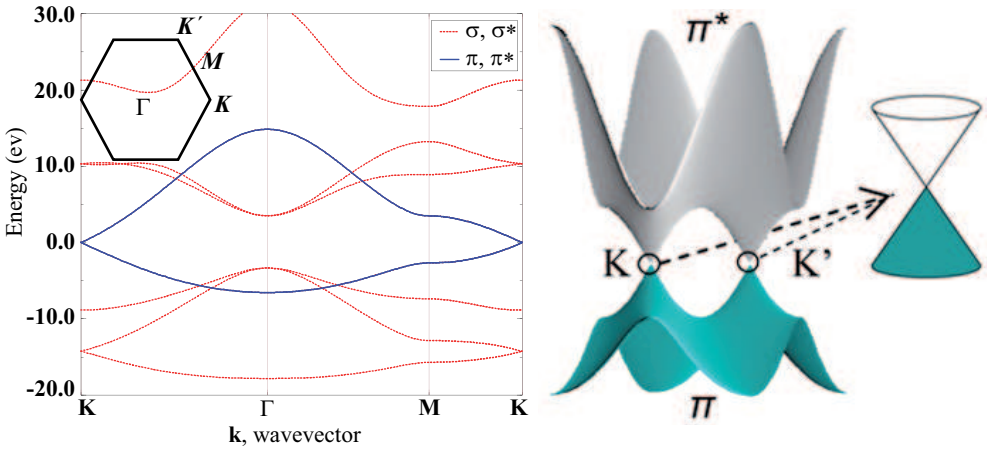

Figure 2.4: Graphene band structure along the high symmetry points of the reciprocal lattice (right panel), 3D structure of the π orbitals with a linear energy dispersion near the Fermi level in the inset.

The hexagonal elementary cell of graphene contains two carbon atoms. The corresponding Brillouin zone in the reciprocal lattice has a hexagonal structure as well, however it is rotated by 90° with respect to the elementary cell in the real space. The Brillouin zone contains three points of high symmetry designated as K, M and Γ. Fig. 2.4 shows the band structure of the graphene along high symmetry points (b) and structure of only π orbitals in the first Brillouin zone computed for the reciprocal effect of three nearest neighbors ("third nearest neighbor tight-binding approximation"). The π or-

bitals are formed via binding of $2p_z$ orbitals of two adjacent carbon atoms and the resulting π, π^* molecular orbitals cross at the high symmetry K–point of the graphene Brillouin zone, exactly at the Fermi level. These orbitals in the terms of solid state physics are regarded as valence and conductance bands. Thus, graphene is a "zero bandgap" semiconductor. The inset at the Fig. 2.4 demonstrates the linear energy dispersion of the graphene bands near the Fermi level at the K point responsible for many remarkable properties of the graphene itself [18].

The unit cell of the carbon nanotube is formed by a cylindrical surface with height T and diameter d, where T is the length of the tube translational vector. The latter is defined as the smallest graphene lattice vector perpendicular to $\mathbf{C}_h$ determining the translational period along the tube axis. It can be calculated from chiral indexes as:

$$\mathbf{T} = \frac{2m+n}{gcd(2n+m, 2m+n)}\mathbf{a}_1 - \frac{2n+m}{gcd(2n+m, 2m+n)}\mathbf{a}_2 \tag{2.4}$$

where gcd() stands for the greatest common divisor. T varies strongly with the chirality of the tube; chiral tubes often have very long unit cells.

The determination of the unit cell of the CNTs allows us to construct their Brillouin zone. The reciprocal lattice vector $\mathbf{k}_z$ in the direction of the tube z–axis corresponds to the transitional period T, and has a length $k_z = 2\pi/T$. As the tube is regarded as infinitely long, the wave vector $\mathbf{k}_z$ is continous, therefore the first Brillouin zone in the z–direction is the interval $(-\pi/T, \pi/T]$. In contrast to $\mathbf{k}_z$ the wave vector $\mathbf{k}_\perp$ along the circumference of the tube can assume only quantized values due to the reduced dimensionality of the system. The wave function of electrons in the nanotube must have a phase shift of an integer multiple of 2π around the circumference, as all other wavelengths will vanish by interference. This implies a boundary condition on the wave vector:

$$\mathbf{k}_{\perp,j} = \frac{2\pi}{\lambda} = \frac{2\pi}{|\mathbf{C}_h|}j = \frac{2}{d}j \tag{2.5}$$

where j is an integer taking the values $-n_c/2+1, \ldots, 0, 1, \ldots, n_c/2$, n_c

being the number of graphene hexagons in the nanotube unit cell. Thus the first Brillouin zone of carbon nanotubes consists of n_c lines parallel to the z–axis separated by $\mathbf{k}_\perp = 2/d$, Fig. 2.5. In the first approximation the electronic band structure of a particular carbon nanotube can be found by cutting the two–dimensional band structure of graphene into n_c lines of length $2\pi/T$ and distance 2/d parallel to the direction of the tube axis Fig. 2.5. In this way, the appropriate SWNT bands are found. This approach is called *zone folding* and is commonly used in nanotube research. Although results obtained using this method are satisfactory in many cases, for the more precise calculation of the band structure the curvature effects and the cylindrical geometry of the nanotubes have to be taken into account.

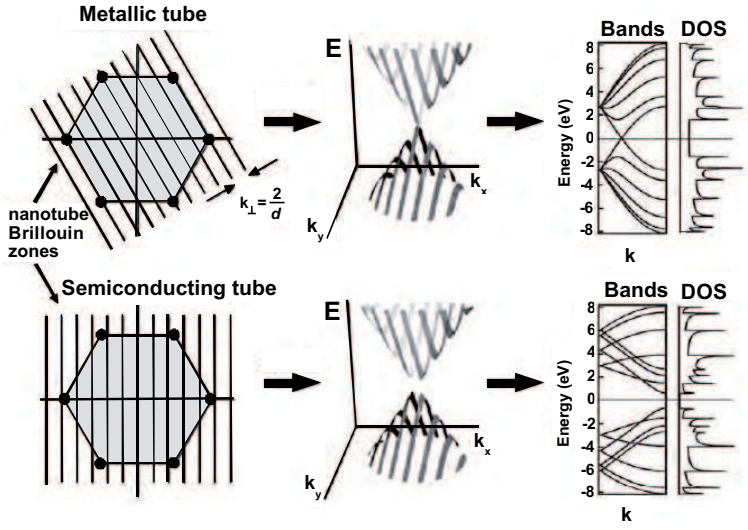

Figure 2.5: From left to right: The Brillouin zone of a carbon nanotube, "cutting lines" in the energy dispersion of the π orbitals, corresponding energy bands and density of states.

The density of states (DOS) of the SWNTs can be directly calculated from their band structure using the definition of the DOS:

$$DOS \propto (\frac{dE_j}{dk})^{-1} \tag{2.6}$$

An example of such a derivation of the DOS for metallic (upper panel) and semiconducting (lower panel) cases are depicted on Fig. 2.5. It shows that at certain energy values the density of states exhibits sharp peaks called van Hove singularities (vHs). These maxima occur when the energy dispersion relation has a infinitesimal upward gradient as function of k, i.e. for each extremum of the energy. These singularities are characteristic for 1–dimensional systems and combined with the peculiar properties of SWNTs give rise to several interesting phenomena. One of them is the unusual absorption spectrum of these materials with many well resolved narrow peaks resulting from different chirality species. Due to the very small momentum of the absorbed photon compared to the line separation $\mathbf{k}_\perp = 2/d$ of the SWNTs' Brillouin zone, the allowed transitions are only those within the same Brillouin zone line or so–called vertical transitions. In other words the electron from any van Hove singularity below E_F can be excited only to the band which is its mirror image with respect to the Fermi level in the energy band (or DOS) diagram. This transitions are usually called E_{11}(or A), E_{22}(B), ..., E_{ii} transitions and are shown in Fig 2.6.

$\Delta\mathbf{k} = 0$ is not the only selection rule for the optical transitions in the nanotubes. One of the noteworthy properties of the electronic transitions which also arises from the reduced dimensionality is their strong dependance on the relative polarization of the electric–field vector to the nanotube axis. Depolarization or antenna effect takes place which implies that carrier excitations are possible only with the field component parallel to the tube axis. For external fields applied in other directions charges are induced on the cylinder walls. The resulting polarization vector opposes the external field and reduces the electric field.

As mentioned above, a very interesting electronic property of the carbon nanotubes is their either semiconducting or metallic nature. As depicted in Fig 2.6 two typical structures are possible for the energy bands. When the cutting line of the Brillouin zone goes trough K point the density of states has a finite value at the Fermi level due to the respective linear energy

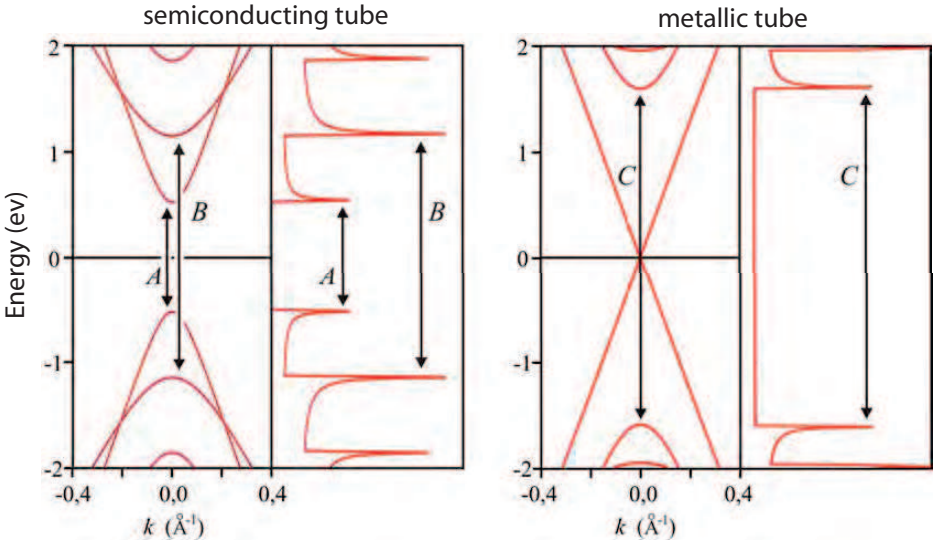

Figure 2.6: Energy dispersion and density of states of semiconducting (left) versus metallic (right) tubes, near the Fermi level. For metallic nanotubes because their Brillouin zone the K point of the graphene reciprocal lattice a finite density of states exists at Fermi level.

bands. These nanotubes have metallic characteristics. In all other cases a bandgap opens between the first two vHs and the nanotubes are semiconducting. Strictly speaking, a tiny gap exists also for the non–armchair metallic tubes because of the curvature effects[19, 20]. Nevertheless, for most practical purposes and for most experimentally observed carbon nanotube sizes this gap would be so small that, all the $n - m = 3j$ tubes can be considered as metallic at room temperature. From geometrical considerations it is obvious that one–third of all possible SWNT structures will be metals while two–third will be semiconductors.

The size of the gap depends on the diameter of the SWNTs as result of the spatial confinement of electrons in the radial direction. However, the dependence is not simply inversely proportional to the diameter as in the case of e.g. quantum dots, but depends also on the chirality of a certain tube in an elegant manner:

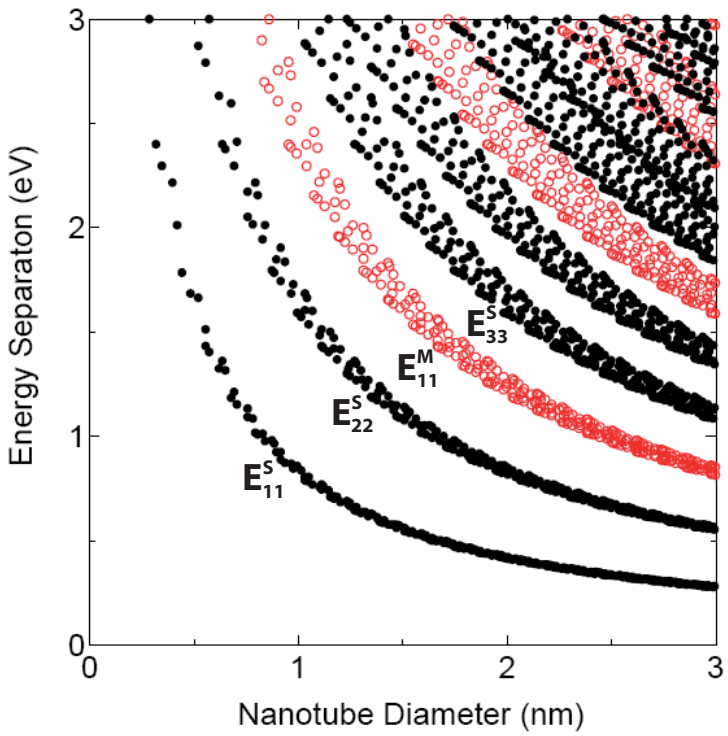

Figure 2.7: The Kataura plot showing the dependence of the electronic transitions in nanotubes on their diameters. The separation of the van Hove singularities scales with the inverse diameter. Black points correspond to semiconducting nanotubes and red points to the metallic ones.

$$E_{11} = 2\gamma_0 a_0 d^{-1} + (-1)^{\upsilon} \frac{t_{11} \cos 3\theta}{d^2} \tag{2.7}$$

where γ_0 and t_{11} are free parameters related to the onsite energy and to the hopping integrals, respectively, d is the nanotube diameter, and θ is the nanotube chiral angle. Fig. 2.7 shows the computed transition energies E_{ii} of semiconducting and metallic SWNTs for different n,m pairs for the diameter range up to 3 nm. The subscript indexes designate the appropriate pair of van Hove singularities, while the superscript indexes "S" and "M" refer in each case to metallic or semiconducting SWNTs. This kind of the representation is the so-called Kataura plot [17].

2.3 Optical Properties

2.3.1 Photoluminescence

As most CNT species are semiconducting it was commonly expected that these materials should be luminescent. It was anticipated that the carriers excited to the higher vHs will relax to the band edge of the first singularity followed by a radiative recombination to the valence band. However luminescence from carbon nanotubes was not observed for many years after their discovery in early 90s. The main obstacle here is apparently the low intrinsic quantum efficiency of the system. Another very important reason that hinders the tube to radiate is their tendency to form small bundles and ropes in most of the samples. The van der Waals forces between individual tubes can be as strong as 500 eV/μm tube–to–tube contact and favor the aggregation of the tubes into bundles. The exact mechanism which quenches the radiative recombination in the bundles is still a matter of debate. Supposedly, the energy transfer [21, 22] from the excitations in the semiconducting tubes to the metallic ones and their subsequent radiationless relaxation is one of the main contributing reasons. Other speculations suggest alterations in the band structure of the individual tube due to the inter–tube interactions which might create sites with non–zero density of states near the Fermi level along the nanotube. Some of the factors influencing non–radiative relaxation channels in CNTs will be discussed later in this work.

In order to prevent the bundling process a procedure of coating the individual tubes with surfactant molecules was successfully implemented by Weisman and coworkers [23]. The surfactant molecules (sodium dodecyl sulfate (SDS)) used in this pioneering work and also in subsequent improved methods have hydrophobic head that aggregates with the nanotube sidewalls and hydrophilic long tails. Ultrasonic agitation of an aqueous dispersion of raw single–walled carbon nanotubes and surfactant material and subsequent centrifugation to remove tube bundles, ropes, and residual catalyst resulted in individual nanotubes, each encased in a cylindrical micelle. Free from the per-

turbation of surrounding tubes and surfaces, the tubes in these suspensions show much better resolved optical absorption spectra. Most importantly, the one-dimensional direct band gap semiconducting tubes in these samples are now found to fluoresce brightly in the 800– to 1600–nm wavelength range of the near infrared. Later analysis of the discrete peaks in photoexcitation emission maps [24] and combined Raman and photoluminescence measurements from single carbon nanotubes [25] allowed unambiguous assignment of the emission peaks to certain tube chiralities.

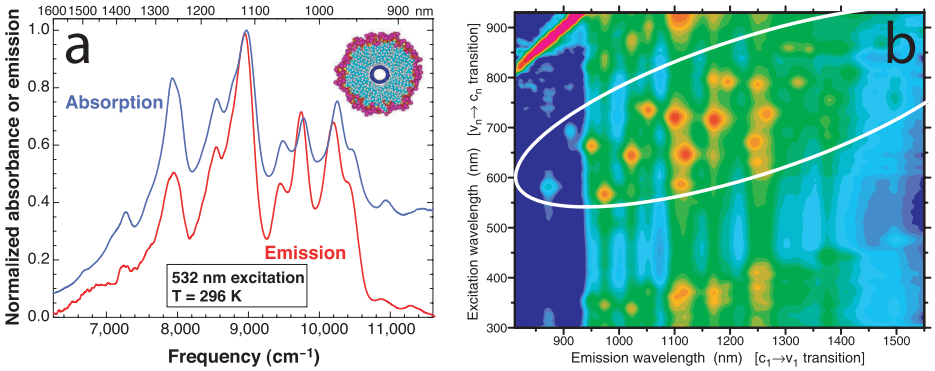

Figure 2.8: Photoluminescence from carbon nanotubes. (a) the emission and absorption spectra of the aqueous solution of surfactant coated nanotubes, with the cross section of the carbon nanotube model encapsulated into a SDS micelle in the inset. Well resolved peaks belonging to different nanotube charities are present in both spectra. (b) photoluminescence intensity as a function of emission and excitation wavelengths, from [23, 24].

Fig. 2.8 shows the well resolved peaks in the absorption and emission spectra of the micelle encapsulated SWNTs aqueous solution (a) and photoluminescence excitation map of the material (b). In the contour plot the fluorescence intensity versus excitation and emission wavelengths is depicted. Each feature in the region marked by a white ovale corresponds to the E_{11} emission of a certain (n,m) species after their excitation to the second van Hove singularity of the conduction band. Similar results were reported for individual nanotubes suspended in air, free of substrate interaction [26, 27, 28].

2.3.2 Excitons

The electronic structure of SWNTs presented above does not take into account the electron–electron interactions but assumes free non–interacting carriers. However, strong confinement of electrons in the 1–dimensional geometry suggests that these interaction can significantly influence the band structure. Indeed, early theoretical calculations predicted that because of strong Coulomb interaction the excited electron in the conduction band and the hole in the valence band will form strongly correlated entities known as excitons [29, 30, 31, 32]. Another important effect that results from Coulomb interactions is the so called band gap renormalization (BGR). Electron–electron repulsion in the stongly confined 1–D system leads to a larger energy gap compared to the free carrier picture. The net impact of these two effects results in optically active singlet excitonic states with an energy close to calculated values based on zone folding free carrier approximation. Moreover, in contrast to 3D or 2D materials the density of states for one dimensional structures with sharp singularities does not change significantly with the addition of excitonic states. These factors made the existence of the excitons in the CNTs elusive in the early stages of carbon nanotube research.

As a result of strong Coulomb interaction strongly bound hydrogen-like excitonic states are formed below the energy of the vHs. The structure of these excitonic states determines the optical, electronic and other properties of the nanotubes. Moreover, the unique electronic structure of the graphene and SWNTs give rise to interesting features of the excitonic manifold. Two special points in the Brillouin zone the K and K' points, emerge as a result of the unusual geometrical structure of sp^2 hybridized carbon atoms. These points are related by time-reversal symmetry [33] and therefore the conduction and valence bands in the vicinity of these points constitute two sets of inequivalent bands (Fig. 2.9 a), Fig. 2.10 a)) making carbon nanotubes different from other nano systems, which also have large excitonic effects, but do not have similar symmetry constraints. Although an optical transition occurs vertically in k space, we can consider the electron and the hole in the

electron-hole pair to be either in the same valley, or an electron to be in one valley and a hole in the other valley. The latter pair can form an excitonic state, but it never recombines radiatively because the electron and hole do not exist in the same valley; such a state is called a dark exciton Fig. 2.9 b). Differences in symmetry are important and guide electronic-structure calculations and the interpretation of experiments. Therefore, an analysis of exciton symmetries in SWNTs is needed to understand in greater detail many aspects of their optical properties.

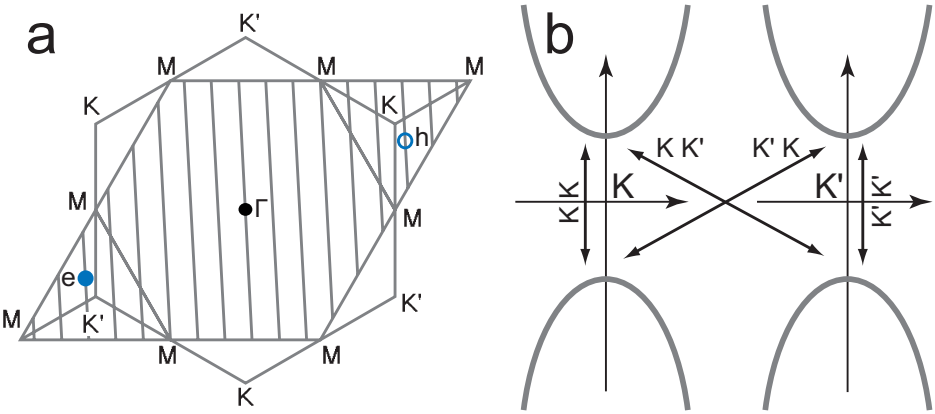

Figure 2.9: a)Brillouin zone of the (6,5) nanotubes showing to inequivalent valley near K and K' points (adopted from [33]). Electron (filled cycle) and the hole (empty cycle) are depicted on the cutting lines in the vicinity of K and K' points, respectively . b) the four excitonic states formed as a result of mixing of two bands near the K and K' points.

Because the exciton wave function is localized in real space by a Coulomb interaction, the wave vector of an electron (k_e) or a hole (k_h) is not a good quantum number any more, and thus the exciton wave function Ψ_n for the n-th exciton energy Ω_n is given by a linear combination of Bloch functions at many k_e and k_h wave vectors.

$$\Psi(\vec{k}_e, \vec{k}_h) = \sum_{v,c} A_{vc}\phi_c(\vec{k}_e)\phi_v^*(\vec{k}_h), \tag{2.8}$$

where v and c stand for valence and conduction band states, respectively.

Then the Fourier transformation of the localized exciton (e.g. a Gaussian wave packet) wave function will obviously result in a localized wave function also in k–space and thus we can define the central position of the latter as a wave vectors of the of the electron and the hole in the bound exciton. For the theoretical determination of the coefficients A_{vc} and to obtain the mixing of different wave vectors by the Coulomb interaction it is necessary to solve a Bethe–Salpeter equation which incorporates many-body effects and describes the coupling between electrons and holes.

$$\sum_{k_e,k_h}((E(\vec{k}_e)-E(\vec{k}_h))\delta_{\vec{k}'_e\vec{k}_e}\delta_{\vec{k}'_h\vec{k}_h}+K(\vec{k}'_e\vec{k}'_h,\vec{k}_e\vec{k}_h))\Psi_n(\vec{k}_e\vec{k}_h)=\Omega_n\Psi_n(\vec{k}'_e\vec{k}'_h), \tag{2.9}$$

where $E(\vec{k}_e)$ and $E(\vec{k}_h)$ are the quasi-electron and quasi-hole energies, respectively and are the sum of the single-particle energy and the self-energy. The self-energy encodes the exchange-correlation potential an excited quasi–particle feels due to the surrounding electronic medium, and it is nonlocal and energy dependent. Here quasi-particle means that we add a Coulomb interaction to the one-particle energy and that the particle has a finite life-time. Equation 2.9 represents simultaneous equations for many k'_e and k'_h points. The $K(\vec{k}'_e\vec{k}'_h,\vec{k}_e\vec{k}_h)$is the mixing term which takes into account the direct and exchange interactions of spin-singlet and spin–triplet states.

Although by solving Bethe–Salpeter equation it is possible to calculate the exact excitonic manifold of the system [30, 31] some important optical properties like the above mentioned availability of the excitonic state from the ground state can be obtained only from symmetry considerations [34]. For this purpose the effective mass and envelope function approximation (EMA) [35] can be used and the final excitonic wave function's symmetry can be directly related to the symmetry of the conduction and valence states where the electron and the hole forming the exciton originate from. It is important to note that for the use of the approximation the contributions from only 1st (n-th) van Hove singularity states can be used which is justified given the large energy separations of the singularities. Thus the approximate

wave function

$$\psi^{EMA}(\vec{r}_e, \vec{r}_h) = \sum_{v,c}{}' B_{vc}\phi_c(\vec{r}_e)\phi_v^*(\vec{r}_h)F_\nu(z_e - z_h) \tag{2.10}$$

will have the same symmetry as the real wave function. Here the prime in the summation indicates that only states from the given singularity are included. The "hydrogenic" envelope function $F_\nu(z_e - z_h)$ provides the localization of the exciton along the principal z axis of the nanotube and ν labels the levels in the 1D hydrogen–like series. The use of this envelope function is dictated from general physical considerations for the ordering in which the different exciton states appear. Finally, to evaluate the symmetry of the excitonic state its irreducible representation $D(\psi^{EMA})$ should be examined. The $D(\psi^{EMA})$ is simply related to the product of the respective irreducible representations of the conduction state $D(\phi_c)$, valence state $D(\phi_v)$ and the envelope function $D(F_\nu)$

$$D(\psi^{EMA}) = D(\phi_c) \otimes D(\phi_v) \otimes D(F_\nu) \tag{2.11}$$

We can now apply the Eq. 2.11 to study the symmetry related properties of the excitons in nanotubes. Here we consider only E_{11} transitions of the most general case of the chiral nanotubes as they were subject of the experimental studies of the current work. The similar discussion for the achiral (zigzag and armchair) nanotubes can be found in the original work of Barros *et al.* [34].

Fig. 2.10 a) shows the two inequivalent bands in the vicinity of K and K' points of the nanotube's Brillouin zone. As mentioned above these two bands are related by time-reversal symmetry and have band extrema at $\pm$ k points. The symmetry of these bands in the commonly used molecular symmetry notation[1] [37] are $E_\mu(k_0)$ and $E_{-\mu}(-k_0)$. Here E stands for the doubly degenerate representation and μ is the quasiangular momentum quantum

[1]For the description of the symmetries of the nanotubes the so called "line group" notations were also introduced which provide somewhat more convenient but equivalent labeling. [36]

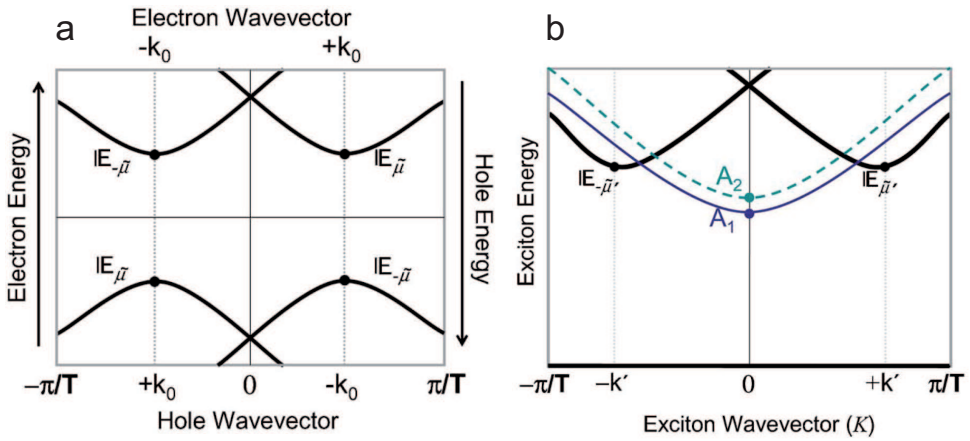

Figure 2.10: Forming of excitonic states in a chiral nanotube [34]. (a) The inequivalent pair electron and hole bands in a free carrier picture, (b) corresponding four excitonic bands with different symmetries. The electron hole and exciton states at the band edges are indicated by a solid circle and labeled according to their irreducible representation.

number associated with the cutting lines of the Brillouin zone. Thus for the lowest "hydrogen level" of the envelope function $\nu = 0$ with the absolutely symmetric $A_1(0)$ representation we have

$$\begin{aligned}(E_\mu(k_0) - E_{-\mu}(-k_0)) \otimes (E_{-\mu}(-k_0 - E_\mu(k_0)) \otimes A_1(0) \\ = A_1(0) + A_2(0) + E_{\mu'}(k') + E_{-\mu'}(-k')\end{aligned} \tag{2.12}$$

where k' and μ' are the exciton linear momenta and quasiangular momenta respectively. Here for A_1 and A_2 symmetries A stands for the symmetrical rotation around the principal axis with odd and even parity respectively for subscripts 1 and 2. The resulting four lowest set of excitonic bands is shown in Fig. 2.10 b). The excitonic bands that have an energetic minimum at the Γ point result from electron and hole states from different bands (near K and K' points). As the ground state of the nanotube has a totally symmetric A_1 representation only one of these two excitonic states fulfills the selection rule of one photon absorption and emission polarized parallel

with the nanotube axis. This is a consequence of the fact the interaction between the light polarized along the principal axis and the electric dipole moment in the nanotube transforms as the A_2 representation for the chiral nanotubes [38]. Thus, only the product of A_2 state with the symmetry of the interaction equals to the ground state's symmetry and the other state is a optically inactive dark state. The other two states formed by the same K and K' bands will be dark as well because they do not match the selection rules for both symmetry and momentum (they have non–zero momenta). Other values of the envelope function ν (odd and even) will leave the decomposition in the Eq. 2.12 unchanged, hence, there will be one and only one optically active excitonic state per each ν.

The similar set of excitonic bands exists also for triplet excitons which have lower energies compared to singlet states [39, 40, 41]. The obvious difference is that triplets are non–emissive due to the spin selection rule. Thus only from symmetry considerations it becomes obvious that not all excitonic states are emissive. However if the ideal structure of the nanotube is modified e.g. by defect introduction, the discussed selection rules can be relaxed because of the change in the symmetry of the structure [39]. In this case the exciton state can be formed by mixing of states with different parity and multiplicity depending on the nature of the introduced defect. In Chapter 5 we will show for the first time the experimental realization of this effect. By intense pulsed laser excitation and by interaction of metal atoms with the individual nanotube we show that singlet A_1 symmetry and triplet states can be "brightened" i.e. turned into emissive.

The existence of strongly bound excitons was experimentally observed using the described peculiarities of their electronic states (Fig. 2.11). Namely, the states inaccessible from the ground state with a one photon absorption can be accessible if two photons are absorbed simultaneously. If this state has a higher energy ($\nu > 0$) than the lowest optically active state ($\nu = 0$) it can decay non–radiatively to the latter state and emit a photoluminescence photon. Thus the difference between the energy of the two absorbed photons

and the emitted photon will manifest the excitonic nature of the excited state and will determine the binding energy of the excitons.

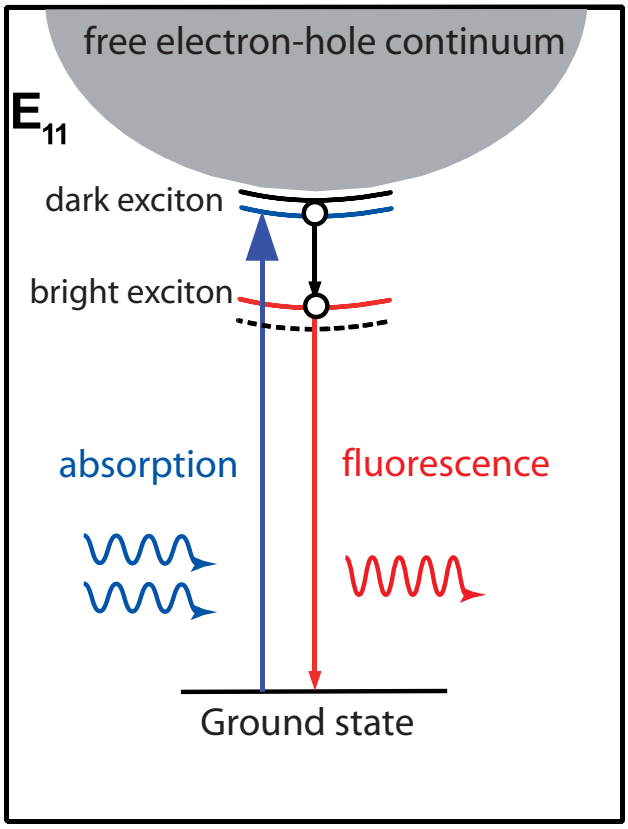

Figure 2.11: Schematics showing the experimatal approach to identify the nature of the excited states in carbon nanotubes. The two–photon absorbtion into the dark excitonic state is followed by its radiationless relaxation to bright state and subsequent fluorescence. The difference in the energy of the absorbed and emitted photons determines the biding energy of the exiton.

This experimental approach was successfully implemented by two groups [8, 42] and exciton binding energies (E_b) up to 1 eV have been determined. Thus, the exciton binding energy constitutes a substantial fraction of the gap energy. For comparison the exciton binding energies in bulk semiconductors typically lie in the range of several meV and represent a slight correction to the band gap [43].

These significant binding energies suggest that the excitons in SWNTs should be more strongly localized than their weakly bound bulk counterparts. Indeed, the wavefunction of the excitons was found to be fully delocalized along the circumference of the nanotube and strongly localized along the nanotube axis, with resulting exciton Bohr radius corresponding to the envelope function defined in Eq. 2.10 of ∼3nm [8, 44]. Thus, the size of the exciton is comparable and even larger than the diameter of the nanotube and as a result the effect of the lattice potential can be incorporated into the effective masses of the electron and hole as is usually done for the so called Wannier–Mott excitons.

The size of the excitons in the nanotubes also implies that their binding energy will be very sensitive to the environment. The Coulombic coupling between the electron and hole forming the 1D exciton, as in the case of bulk excitons, depends on dielectric screening. In bulk excitons the binding energy is proportional to $1/\varepsilon^2$, where ε is the dielectric function of the material. In nanotubes, when the exciton size is larger than the tube diameter, most of the electric-field lines between charges penetrate the surrounding medium and this makes the exciton binding energy (as well as the bandgap) a function of the dielectric constant of the surrounding environment. Perebeinos et al. [31] gave the following expression for the dependence E_b on CNT diameter (d), chirality through the effective mass (m^*) and dielectric constant (ε):

$$E_b = C d^{\alpha-2} m^{*\alpha-1} \varepsilon^{\alpha} \tag{2.13}$$

where $\alpha = 1.4$. Hence, the poor screening in the vacuum or dielectric environment outside of the nanotube allow for significant binding energies of 0.4-1.0 eV characteristic for Frenkel type excitons. This dual nature (Wannier–Mott and Frenkel type) of the excitons is a unique feature of carbon nanotubes. The excitonic nature of the excitation was shown even in metallic nanotubes with combination of Rayleigh scattering and absorption spectroscopy [45]. Normally, one does not find bound excitons in bulk metallic systems because the long-range part of the electronhole interaction is

screened out completely by the available carriers. However, the reduced dimensionality leads to the incomplete screening of Coulomb interactions and exciton formation.

Thus, in carbon nanotubes the excited state oscillator strength is almost completely transferred from the free carrier band edge to the excitonic manifold. The former still exists with a far smaller weight and does not play a major role [46]. The described excitonic structure of the carbon nanotubes has a very important impact on optical, electronic and other properties of this material. Naturally, it influences also the dynamics of the excited state discussed in present work.

2.4 Excited State Dynamics

Recent rapid advances in synthesis of high quality, low cost nanotube materials opened perspectives for new applications in different promising fields dealing with optoelectronic properties of CNTs, e.g. ultracompact and narrow-band emitters and detectors. Knowledge of excited state dynamics of these systems is absolutely crucial for achieving desired goals as it probes the fundamental properties of the CNTs like electron-photon/phonon coupling, exact electronic/excitonic structure, nature of the various defect states, impact of the environment on the electronic processes and many other interesting and important characteristics. In this work these questions are addressed by investigating the exciton recombination lifetimes of single carbon nanotubes at room temperature.

In any electronic system after absorption of a photon with an appropriate energy matching the transition resonance of its electron, an excitation from the ground state to higher energy electronic states occurs. The characteristic time needed for the electron to return to the ground state is called *lifetime* of the excited state. Decay channels influencing the effective lifetime can be divided in two major groups: radiative and non–radiative. Radiative relaxation is associated with the emission of a photon whereas non–radiative

relaxation can have various pathways such as coupling to phonons, energy transfer to the environment, quenching by other molecules or by intrinsic defects. A useful measure for this output is the *quantum yield* defined as

$$\eta = \frac{\gamma_r}{\gamma_r + \gamma_{nr}} \tag{2.14}$$

where γ_r and γ_{nr} are radiative and nonradiative decay rates, respectively (inverse of lifetime τ) .

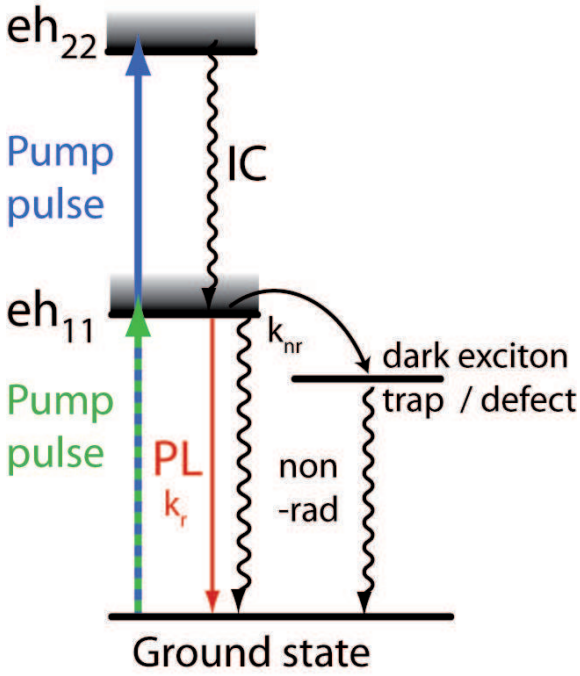

Figure 2.12: Schematic representation of the commonly accepted picture of the excited state's relaxation channels in the CNTs. The exciton pumped into its first excited manifold by an external stimulus relaxes to the ground state predominantly via non–radiative relaxation channels.

The *radiative* lifetime of the system is given only by the oscillator strength of the specific excited state. For the SWNTs theoretical calculations [47, 39] predict this parameter to be in the range of $\sim 10ns$ at room temperature. On the other hand all the measurements of the ground state recovery lifetime using different methods, samples and environments give us lifetimes that

are faster by several orders of magnitude and very low quantum yields were measured in the range of 10^{-3}. This fact indicates that the total decay rate $\gamma = \gamma_r + \gamma_{nr}$ is dominated mainly by the non–radiative decay channels. One of the main goals of this work is to discuss the possible mechanisms of the non–radiative relaxations of excitons in the SWNTs.

Many measurements on excited state dynamics have been reported during the last several years, for various samples of SWNTs using different methods. Although these findings step by step bring us closer to the full understanding of the principal properties of the problem, there is a large variety of different observations often contradicting each other. This concerns mainly the timescale of the ground state recovery ranging from sub–picosecond dynamics to several hundreds of picoseconds, the time dependence of the exciton recombination and the exact structure of exciton manifold's electronic states. Apparently, this discrepancies are due to differences in the sample preparation and processing as well as to different measuring methods. As many of this experiments were done on ensemble samples, the averaging over individual features of single nanotubes like defect concentration, length, coupling to the environment, bundling also contributes heavily in complicated and sometimes controversial interpretations of the data. Thus, in this work we tried to use an approach that would simplify the matter and reduce the number of unknown parameters by investigating *individual* SWNTs and by using relatively straightforward Time Correlated Single Photon Counting (TCSPC) technique for measuring time resolved photoluminescence. Previously this approach was used to measure SWNTs exciton decay lifetimes at low temperature [9] and quite a big variation of recombination lifetime for different tubes (20–180ps) was detected. At room temperatures similar experiments might seem to be challenging as the PL intensity is reduced by a factor of ~ 5 and the decay times are also decreased dramatically [9, 48, 49]. However, the results shown here indicate that a well optimized confocal laser scanning microscope setup is capable for such investigations and we can benefit largely from advantages of the ambient conditions. Moreover, from the application

point of view room temperature measurements are even more valuable as most of the devices are supposed to work in these conditions.

First studies on the excited state dynamics of SWNTs were done mainly using the so called "pump–probe" techniques. In these experiments two spatially overlapped beams from pulsed lasers are used. The first beam excites the system from its grounds state and the second beam probes the evolution of the excited state. The measured signal here is the enhanced or reduced transmission of the probe beam through the sample respectively due to either stimulated emission and photobleaching or excitation of the system to even higher electronic states. Thus, by varying the time delay between the two pulses one can investigate dynamic electronic processes of the system. Though this technique has a major advantage, that is the temporal resolution of the experiment is limited only by the laser pulse duration and not by the response time of the detection electronics, very often there are complications in the interpretation of the data caused by different types of signals (positive and negative) and overlapping contributions in different spectral regions from various nanotube species. Besides this, the powers usually used in these experiments are relatively high in order to be able to detect the small variations in the transmission. High power excitations however, are shown to cause additional non–linear processes in the excited state dynamics like Auger recombination or exciton–exciton annihilation [50, 51, 52] which further complicate the matter substantially.

Nevertheless, valuable information have been obtained using this method for semiconducting SWNTs excited to their first excitonic state. They were shown to exhibit a very fast recovery to the ground state with time constant of ~ 1 ps, attributed to nonradiative decay [53, 54, 55, 56]. By correlating the photoinduced absorption signal corresponding to the difference of the first and second excitonic bands' energies with the photobleaching from the first excitonic band Manzoni et. al. [57] determined the time constant of $\sim 40fs$ for the intersubband exciton relaxation. The availability of unbundled, individual SWNTs free from complications of intertube interactions as

well as chirality enriched materials [58], made it possible to improve the understanding of these experiments. The detection of signals indicating the transitions of excited electrons to other non–emitting states (dark excitons or non–emitting trap states), made it closer to the full understanding of the dynamical properties of the system [59], [60].

On the other hand, the discovery of the bandgap photoluminescence from surfactant coated semiconducting carbon nanotubes [23, 24, 25] enabled the direct measurement of the decay rate of the PL. Early measurements on suspension of isolated SWNTs using Kerr gating [61] technique showed bi-exponential decay with a fast component in the order of $\sim 7ps$ attributed to intrinsic non–radiative relaxation channels. In that work authors suggested that given the extremely low fluorescence quantum efficiency, η, of carbon nanotubes ($\sim 10^{-4}$) the intrinsic radiative lifetime γ_r can be estimated to be as long as $\sim 100ns$.

Several other measurements of time-resolved fluorescence reported somewhat longer lifetimes with mono- [62, 63, 48], bi- [64] and multiexponential decay dynamics [49]. The short lived components within 10–60 ps is usually believed to be due to coupling to either extrinsic relaxation channels like radiationless energy transfer to metallic tubes in the small residual bundles or to intrinsic non emissive states. The observed long lived components in some experiments ranging from several hundreds of picoseconds to several nanoseconds are attributed to the real intrinsic lifetime of individual SWNTs.

Chapter 3

Experimental

3.1 Confocal Microscopy of Single Carbon Nanotubes

The measurement of the excited state dynamics of the single carbon nanotubes consists of two main parts. First, the individual nanotubes are identified on the substrate by confocal microscopy and afterwards the exciton recombination lifetime is measured using Time Correlated Single Photon Counting (TCSPC) technique.

The concept of confocal microscopy, depicted in the Fig. 3.1 is to excite the material resting on the substrate by a tightly focused diffraction limited spot of the excitation beam from the light source (typically a single mode laser source) and then to detect the locally generated optical signal by guiding it through a pinhole [65]. The latter is done in order to avoid the background originating not from the excitation area. The small detection area of the detector can also act as a spatial filter, i.e pinhole. The measured optical response of the system can be different types of light–matter interactions, such as elastic or Raman scattering, fluorescence, higher–harmonic generation etc. To generate an image of the optical response from the sample either the laser beam or the sample itself has to be raster scanned. The availability of translators based on piezoelectric actuators made it possible

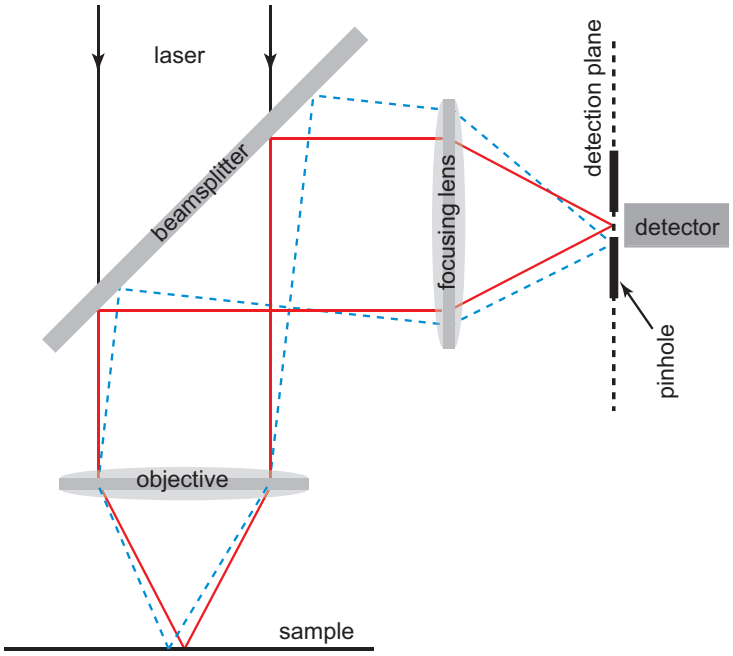

Figure 3.1: Schematic of the confocal microscopy. Only the signal emanating from the focal point of the objective can reach the detector(red solid line). Light emanating from other spots(blue dashed line) is blocked by the pinhole.

to scan areas with nanometer precision.

The confocal microscopy setup is depicted on Fig. 3.2. The excitation source is a Coherent Mira 900 Ti:Sapphire laser. It is pumped by a Coherent Verdi diode–pumped solid state laser operating at 532nm wavelength with 5W output power. The Ti:Sapphire laser can operate either in continuous wave (CW) or in pulsed (mode–locked, ML) regime with pulse duration of 150fs and repetition rate 78 MHz. The operating wavelength can be tuned from 750nm to 900nm depending on the experimental objectives. The typical output power is in the range of 50mW, though for our purposes beams with far less intensities are used in the range of 1μW–200μW. The laser line filter (LLF) with a narrow spectral transmission matching the laser wavelength is located in the beam–path to suppress the fluorescence of the Ti:Sapphire crystal. The set of neutral density (ND) filters reduce the intensity of the

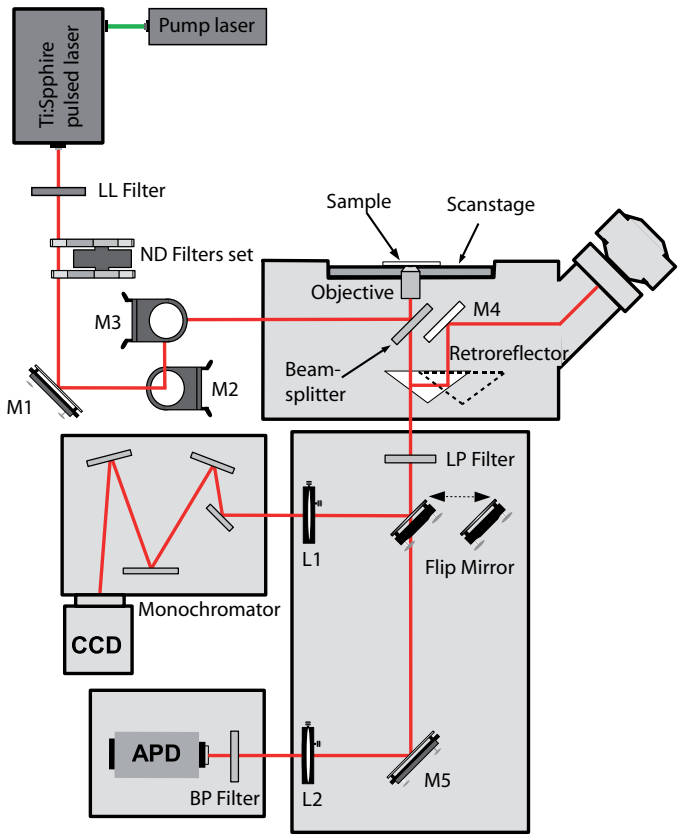

Figure 3.2: The basic elements of the experimental setup. Excitation is provided by a pulsed tunable laser, confocal detection principle is used to measure PL spectra(spectrometer) and transients(APD) from individual nanotubes.

laser beam to obtain powers required for a given experiment. Next, the beam is guided into the inverted microscope (Nikon Eclipse TE2000 E) with a set of mirrors (M1, M2, M3). To split the excitation path and the detection path into two separate arms a beam splitter is introduced with a transmittance to reflection ratio of 70/30. Afterwards, the beam is focused onto the sample by an oil immersion objective (Nikon Plan Fluor S) with 1.3 numerical aperture (NA). The high NA objective allows us to have an excitation spot size $\Delta x \approx 0.61\lambda/NA$ as small as half the wavelength of the excitation beam and therefore high lateral resolution of optical signals. Collection angles ex-

ceeding the angle of total internal reflection reached for $NA > 1$ maximize the detection efficiency and are also very crucial for the observation of weak signals emanating from nanoscale emitters as in the case of single carbon nanotubes. The sample, typically a microscope cover slip spin coated with the CNT solution, is then raster scanned by a XY piezo scan stage (Physik Instrumente, P-517.2CL) and at each position the optical signal from the sample is collected in epi-illumination configuration. A retroreflector is used to guide the detection path either to the eye piece or the side port of the inverted microscope.

In the detection path the first element usually is the one that should suppress the excitation background. As we work mainly with spectrally shifted signals with respect to the excitation, e.g. photoluminescence, a long–pass (LP) interference filter is used to block the laser. With the help of a flip mirror the signal can be guided either to the avalanche photo diode (APD)(MPD, PDM 5CTC) or to the spectrometer depending on the measurement goals. Alternately a 50/50 beamsplitter can be used instead of a flip mirror if the simultaneous detection of spectrum and the PL transient (vide infra) is desired. As usually the imaging is done with an APD the signal is guided through a lens to focus it onto the small detection area of the APD of 25μm. As previously mentioned the pinhole is not needed in this case and confocal detection is secured by the small size of the detector. Typical acquisition times per pixel for APD imaging are in order of 20–60ms depending on excitation power. If the detection of the PL signal from a specific chirality nanotube is desired then a narrow band–pass (BP) filter corresponding to the particular chirality emission energy is inserted in front of the APD. Besides the imaging the photodiode is used also to measure the time resolved photoluminescence from single carbon nanotubes as will be described in the next section. In this last case the presence of the bandpass filter, matching the emission wavelength of the tube, in front of the APD is obligatory as the residual fundamental photons not suppressed by the LP filter can bring misleading results.

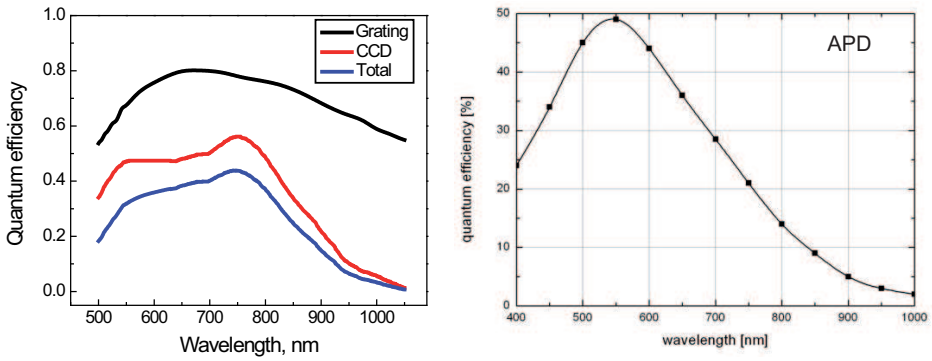

Figure 3.3: The quantum efficiency curves for the detectors used in the current work. a) the QE of the CCD camera and the spectrometer grating, b) the QE of the APD. The curves show typical behavior of Si based detectors that become "blind" for wavelengths longer than ∼1000nm.

The spectra of the SWNTs are measured by flipping up the mirror and guiding the signal to the spectrometer (Andor Technology, Shamrock 303i). An additional lens is situated in front of the spectrometer to focus the light through the entrance slit. The size of the slit can be varied and can be reduced down to 10μm thus, if needed, it can act as a pinhole. Inside the spectrometer the signal is dispersed by a dispersion grating which operates in Czerny-Turner configuration. The dispersed spectrum is then recorded by charged coupled device (CCD, Andor IDUS OE DU420) camera, thermoelectrically cooled to $-60°C$. The typical integration times for obtaining a spectrum from a single nanotube is in the range of 2–30 seconds depending on the emission rate. The spectroscopic imaging of the sample, i.e. recording the spectrum of the sample at each pixel in principle is also possible, however it requires much longer acquisition times given the slow readout speed of the CCD.

The quantum efficiencies (QE) of the detectors used in this work are depicted in Fig 3.3. The working materials of these detectors are based on Si, which has a band gap 1.12 eV at room temperature, therefore their QE decreases drastically at wavelengths longer than $\sim 1000nm$. This limits our studies on the photoluminescence of the SWNTs to those which have a band

gap larger than 1000nm i.e. diameter smaller than $\sim 0.8nm$ according to the Kataura plot 2.7. However, the CoMoCat nanotubes used in this work have a quite narrow diameter distribution peaking at about 0,8nm [66] and based on the comparison of the density of the nanotubes on the microscope cover slips determined from Atomic Force Microscopy (AFM) measurements and optical imaging (vide infra) we conclude that most of the nanotubes present in our samples emit in the detection range of our system.

The total detection efficiency of the system can be estimated from the absorption cross section and the quantum yield of the emitter and the actual count rate detected at the detector. The quantum yield of the SWNTs is in the range of 10^{-3} [9] and absorption cross section is $\sim 10^{-18} cm^2/atom$ [67, 68]. The typical count rate detected at the APD from the PL of the nanotube in the focus of the $10^{14} pulse^{-1} cm^{-1}$ intensity excitation is $\sim$ 1000Hz. Taking into account the repetition rate of the Ti:Sapphire laser of 78 MHz we get an estimation of the overall detection efficiency of the setup of $\sim 10^{-3}$.

3.2 Time Correlated Single Photon Counting

Time-correlated single photon counting (TCSPC) is a sensitive technique for recording low-level light signals with picosecond resolution and extremely high precision [69]. Photon counting techniques consider the detector signal a random sequence of pulses corresponding to the detection of the individual photons. Therefore, the detector signal is a random sequence of single-photon pulses rather than a continuous waveform. The light intensity is represented by the density of the pulses, not by their amplitude. Obviously, the intensity of the light signal is obtained best by counting the pulses in subsequent time channels. A unique feature of photon counting results from the fact that the arrival time of a photon pulse can be determined with high precision. The bandwidth of a photon counting experiment is limited only by the transit time spread of the pulses in the detector, not by the width of the pulses.

Time-correlated single photon counting, or TCSPC, is based on the de-

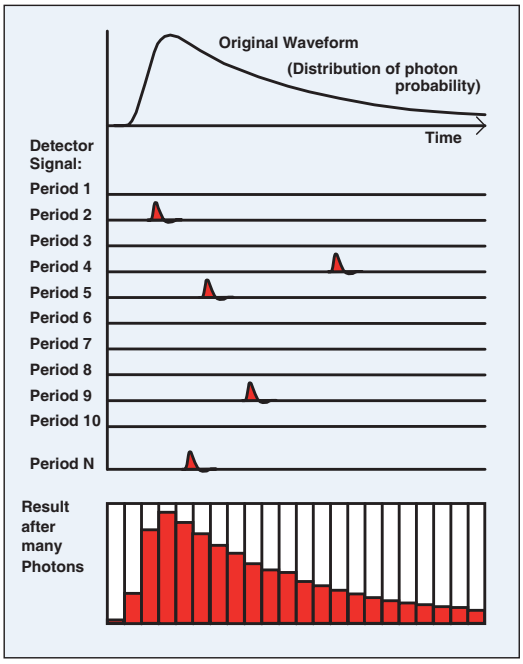

Figure 3.4: The principle of the TCSPC method. The histogram of the detected counts is constructed based on their arrival time. The measurements over many excitation cycles result in a time–resolved signal curve

tection of single photons of a periodic light signal, the measurement of the detection times, and the reconstruction of the waveform from the individual time measurements. TCSPC makes use of the fact that for low-level, high-repetition rate signals, like single SWNT flourescence, the light intensity is usually low enough that the probability to detect more than one photon per one laser excitation pulse is negligible. The detector signal consists of a train of randomly distributed pulses corresponding to the detection of the individual photons. There are many signal periods without photons, other signal periods contain one photon pulse. This situation is depicted in Fig. 3.4.

When a fluorescence photon is detected, the arrival time of the corresponding detector pulse in the signal period is measured. The events are collected in a memory by adding a 1 in a memory location with an address proportional to the detection time. After many signal periods a large number of photons has been detected, and the distribution of the photons over the

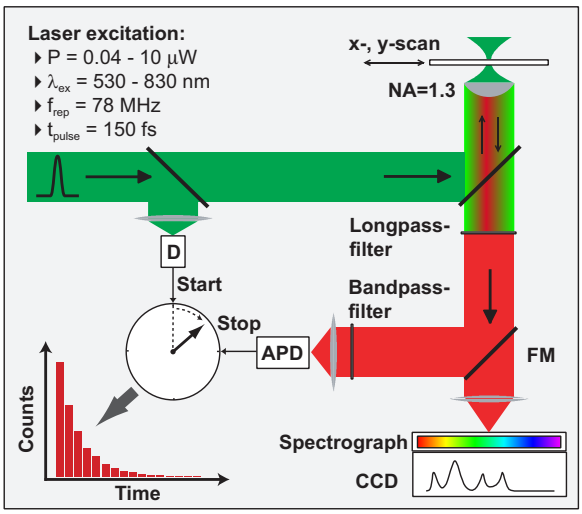

Figure 3.5: The schematics of the TCSPC experiment. The delay time between a laser excitation pulse (start pulse) and the detected PL photon (stop puls) is determined by a TCSPC acquisition card.

time in the signal period builds up. The result represents the waveform of the optical pulse. In other words the generated laser pulse starts the clock and afterwards the PL photon created by the same pulse stops the clock and the measured waveform shows the characteristic delay between the excitation and the emission. The latter is governed by the dynamical properties of the excited state of the sample.

To measure the signal period the exact excitation time of the signal should be known. This is provided by connecting the output of the detector inside the laser which monitors the pulse generation directly to the TCSPC card(SPC-140). Another input of the card is connected to the APD to detect the 'stop' pulse from PL signal. This configuration is schematically represented in the Fig. 3.5. Typical accusation times for a PL transient are in the range of 30-500 seconds.

Chapter 4

Exciton Decay Dynamics in Individual Carbon Nanotubes at Room Temperature

4.1 General Procedure for Exciton Lifetime Measurements

In this chapter exciton lifetimes of individual CNTs are measured using the TCSPC method combined with confocal microscopy as described in the experimental chapter. Here, for the first time, the results on time–resolved photoluminescence (PL) of *individual* SWNTs at *room temperature* are presented. The exciton recombination follows strictly monoexponential decay over four orders of magnitude with time constants varying from tube to tube in the range of $\sim$ 1 to 40ps for the same chirality tubes. The impact of parameters expected to influence the exciton decay, like nanotube length, environment and defect concentration on the photoexcitation relaxation process is discussed.

Samples are prepared by spin coating an aqueous solution of surfactant coated CoMoCat SWNTs [70, 71, 72] on the microscope glass cover slip. Di-

luted solutions are used in order to obtain samples with individual nanotubes and to prevent bundling. The atomic force microscopy (AFM) measurements of the samples show well dispersed, isolated, extended structures (Fig. 4.1). The height of these structures ∼2nm is somewhat bigger than expected for single tubes ∼0.8nm. This is due to the surfactant layers covering the tubes. The residual surfactant can also be seen in the AFM image in a form of small dots with similar height. Almost parallel orientation of the tubes is a result of the spin coating procedure.

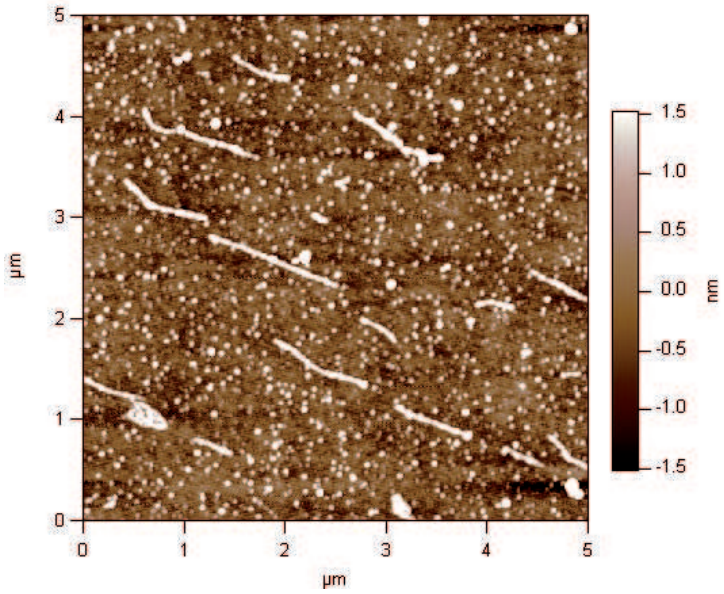

Figure 4.1: Typical AFM image of the sample containing micelle encapsulated nanotubes. Well separated, elongated features are individual SWNTs. The height of the features exceeds single nanotube diameter due to the layer of the surfactant covering the tubes.

Nanotubes are imaged by raster scanning the sample by means of piezo XY scanner and detecting the optical signal from individual tubes with the APD [73]. As the aim of our studies is to investigate the time resolved radiative recombination of the excitons in CNTs, the typical signal detected during the scanning process is the fluorescence from single SWNTs. The detection of inelastically scattered Raman photons to identify the nanotubes

in the sample could be another option. In order to obtain chirality selective signals the RBM Raman mode has to be detected. However, the detection of PL is preferable since the chirality identification using this signal is much less ambiguous. The PL peaks of different (n,m) species are spectrally far better resolvable than RBM modes and also RBM detection would require to be in exact resonance with an electronic state within ~ 20 nm. Moreover, the detection of the Raman active tube does not necessarily mean that it will be a luminescent one, i.e the intensity (or even occurrence) of these signals do not always correlate [74].

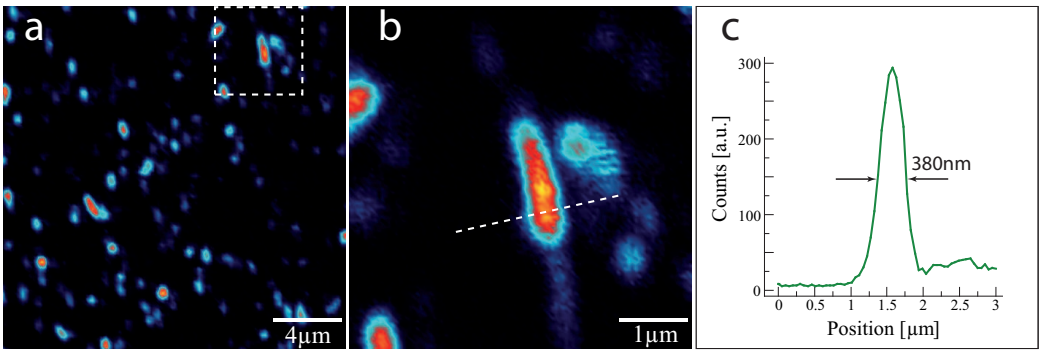

Figure 4.2: (a)A confocal PL image of SWNTs emitting at 800nm - 1000nm spectral range. The density of the emitting nanotubes determined from the optical measurement is in good agreement with the AFM measurements indicating that most of nanotubes ar emissive on glass substarte, (b) zoom-in of the area highlighted in the (a), (c) cross section of the dashed line in (b) showing the spatial resolution of the confocal microscopy setup.

Laser wavelength used in typical experiments presented here was 760 nm, which is close to the exciton–phonon(G) bound state resonance of the (6,4) tubes, above the E_{11} transition [75, 76, 77, 78]. After imaging the area with a 800nm longpass filter all the tubes with a emission energy in the range of the detection limit of the APD can be observed. As our Si–based detector has almost zero detection efficiency at the wavelengths longer than $\sim 1000nm$ (See Fig. 3.3), PL from tubes with only small diameter (smaller

than $\sim 0,8nm$) can be detected. In the Fig. 4.2 (a) typical example of such a PL image from 20μm x 20μm sample area is shown. Some elongated features can be recognized in the image indicating the presence of tubes significantly longer than the confocal spot size. The 5μm x 5μm zoom–in image of such an elongated tube is depicted in Fig. 4.2 (b) together with the cross section taken along the indicated dashed line (c). The 380nm full width at half maximum (FWHM) of the cross section is the maximum achievable resolution with this diffraction limited type of microscopy. The nanotube density of 0.4 $/\mu m^2$ observed in the optical image is in agreement with the value determined from AFM measurements (0.6 $/\mu m^2$) and demonstrates that most of the nanotubes on the substrate are in fact emissive in the accessible spectral range. This shows also that we are not probing optically some particular fraction of the nanotubes but rather most of them.

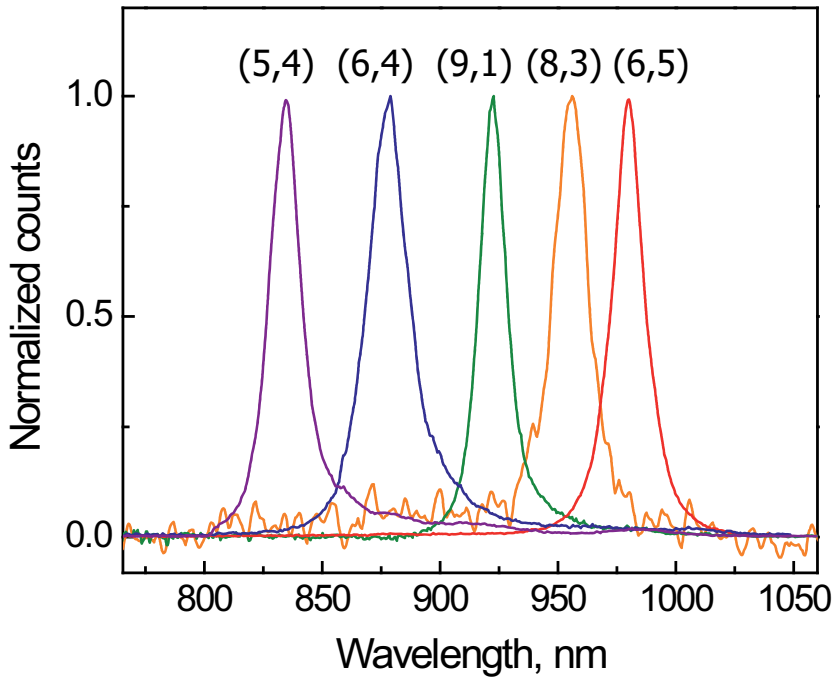

Figure 4.3: Representative photoluminescence spectra of SWNTs. Each of the narrow emission peaks correspond to five individual nanotubes with different chirality as indicated by the index pair (n,m).

Measurement of the PL spectra at different bright spots shows that nanotubes belonging to various chirality species are present in the sample. In Fig. 4.3 normalized PL emissions of five different tubes are illustrated: (5,4) tube with emission maximum at 835 nm, (6,4) tube at 880nm, (9,1) tube at 918nm, (8,3) tube at 958nm, and (6,5) nanotube with emission at 979nm. The assignment of the peaks to the respective chiral indexes is done according to the previous works [25, 24] where the simultaneous of Raman RBM mode and the absorbtion or PL resonances allowed the complete recognition of the emissive species. The position of PL maxima for certain chirality can vary slightly from tube to tube in the range of 10 nm [77]. Also for the FWHM of the emission which is typically $\sim$ 25nm at room temperature, can sometimes be as wide as $\sim$ 100nm. The origins of these variations are still not fully understood. However, the effect of the local environment seems to be the major factor [62, 79, 80, 81, 82]. As it will be discussed later the width of the emission is determined by the dephasing of the exciton caused by elastic exciton-phonon interactions. The slight asymmetry of the lineshape is arising from the non–Markovian nature of this process [83]

For a single straight nanotube, emission and absorption of light should be preferentially polarized along the nanotube axis [25, 27, 84]. The polarization of the emission from a single nanotube can be determined by inserting an analyzer in front of the detector. As in the case of dipole(antenna) emission, the intensity of the PL should follow a $cos^2(\theta)$ behavior, where θ is the angle between the nanotube axis and the analyzer. The Fig. 4.4 visualizes the polarization dependence of the PL intensity integrated over all spectral range of the emission (left panel) along with three spectra at different angles of the polarizer (right panel). Generally the dependance can be nicely fit with $cos^2(\theta)$ function, however often there are noticeable deviations from it as in the case depicted in Fig 4.4. The origin of this deviation is the fact that nanotubes resting on a glass substrate are not ideally straight as it was visualized by AFM or near-field optical microscopy measurements [85, 74].

We focus our time-resolved studies mainly on (6,4) tubes which have an

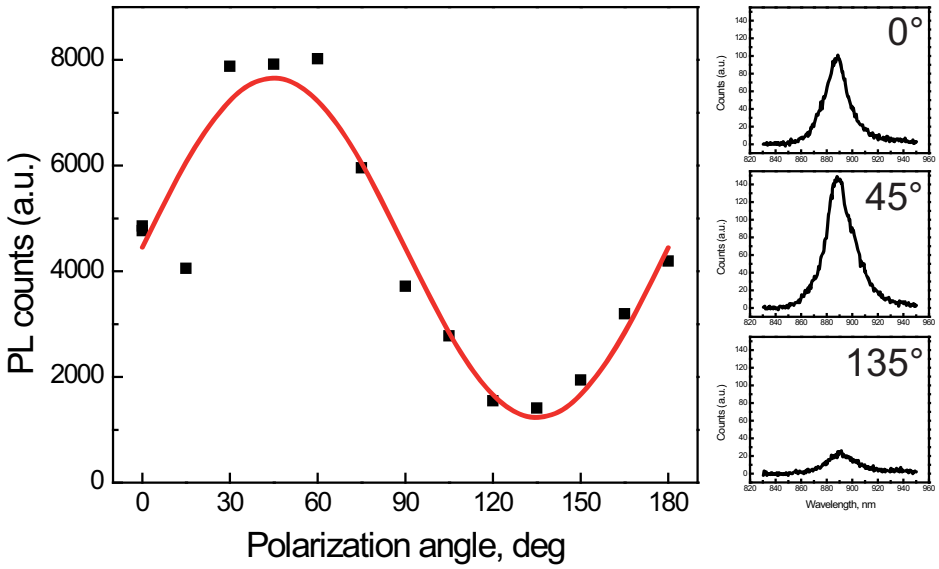

Figure 4.4: Polarization dependence of the integrated PL intensity from a single nanotube (right). The red solid line represents a fit to the data with $cos^2\theta$ function. Spectra at 3 different positions of the analyzer (left).

emission peak at 880nm, well separated from neighboring tube bands at 835 and 918 nm corresponding to E_{11} transitions in the (5,4) and (9,1) SWNTs. In order to locate the tubes with a desired chirality, during the imaging procedure a narrow bandpass filter is introduced in the detection path which spectrally selects the emission from the specific SWNT species. The typical example of such a spectral filtering is shown in Fig 4.5.

After the localization of a nanotube with a certain chirality, it is moved to the focus of the excitation laser source and the photoluminescence transient curve of an individual tube can be obtained. A representative transient curve (blue curve) is shown on Fig. 4.6 with the instrument response function (IRF) corresponding to elastically scattered laser light (green curve). The width of the measured transient is clearly wider than the IRF. This means that the temporal resolution of our setup is sufficient to measure time resolved excited state dynamics of our samples. Obviously, the measured curve for our PL signal is the convolution of the true temporal dependance of the signal with the IRF. To ensure optimum performance, the IRF was recorded repeatedly

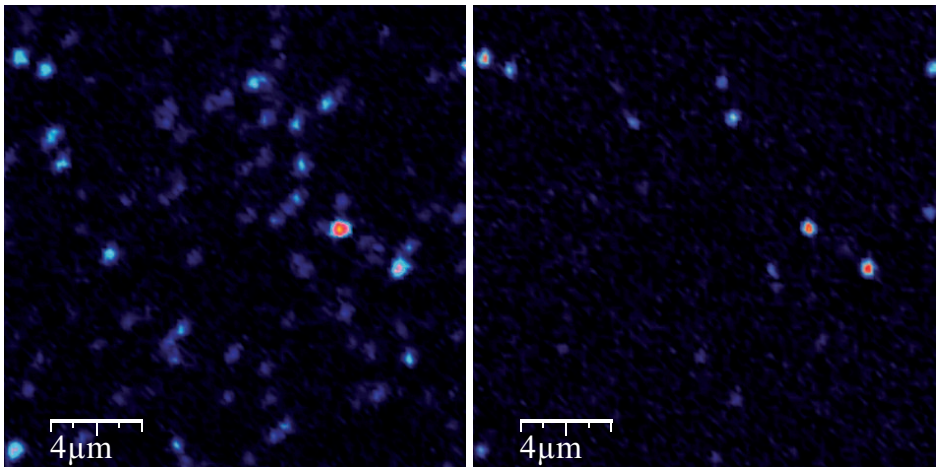

Figure 4.5: Confocal images of SWNT PL emission. (a) image with only 800nm longpass filter in the detection path, (b) image of the same sample area as in (a), but with an additional 880 nm narrow bandpass filter to identify tubes with (6,4) chirality only.

in between measurements. PL transients were fitted by exponential functions that were convoluted with the IRF [86]. Due to the high signal to noise ratio achieved in our experiments and the reproducibility of the IRF the time-resolution of the setup is about 3 ps, close to 10 % of the FWHM of the IRF. This reconvolution procedure shows that our transients can be perfectly fit with a mono–exponential decay function. The result of this fitting is also shown in Fig. 4.6 (red curve) with the weighted residue below employed to judge the goodness of the fit. The uniform profile of the residuum clearly demonstrates that the exciton dynamics at room temperature can be described by a single-exponential decay covering more than four orders of magnitude. Note, that a second slow slope is part of the response function.

4.2 Distribution of Lifetimes

Transients measured for several hundred different $(6, 4)$ nanotubes consistently exhibited mono-exponential decay. The determined lifetimes however showed a broad distribution ranging from about 1 ps to 40 ps. Three tran-

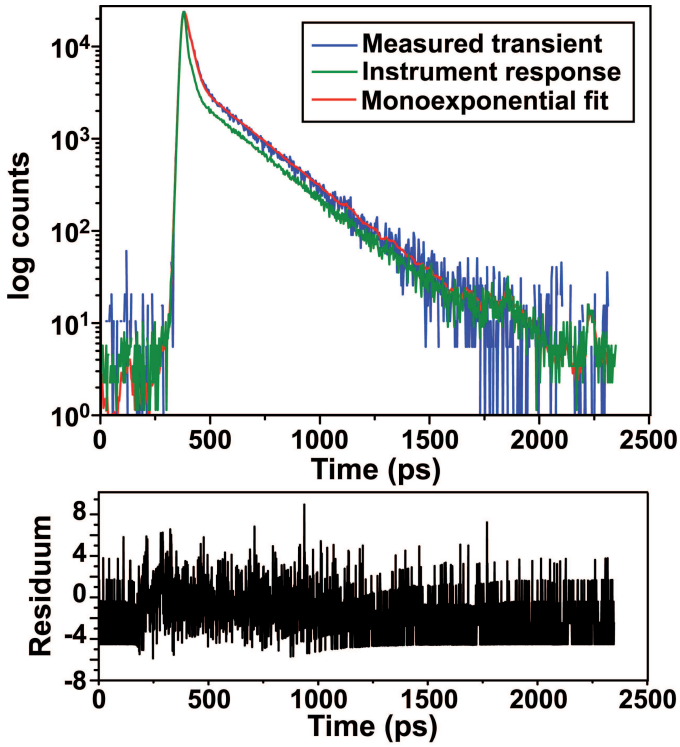

Figure 4.6: Semilogarithmic plot of a representative transient curve (blue line) together with the independently recorded Instrument Response Function (green line). A single-exponential fit function (red line) convoluted with the IRF describes the transient over four orders of magnitude clearly showing monoexponential decay dynamics with a lifetime $\tau = 15 \pm 3$ps. The quality of the fit can be seen from the residuum of measured transient and single exponential fit.

sients are presented in fig. 4.7(a) featuring lifetimes of τ =4 ps, 18 ps and 36 ps. The origin of this variation is very intriguing and it can explain the contradicting results obtained for nanotube ensembles in the literature. It has been previously observed at cryogenic temperatures and has been attributed to the different defect concentration of individual nanotubes [9].

The overall excited state depopulation rate of the nanotube can be written as a sum of radiative and non–radiative decay rates

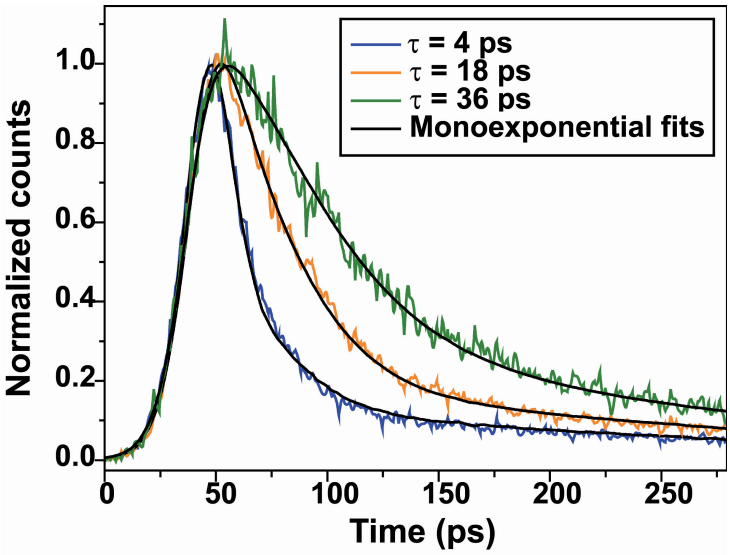

Figure 4.7: Example of transients for the three different (6,4) nanotubes visualizing the variation of exciton lifetime in the range of 4 to 36 ps.

$$\gamma_{tot} = \gamma_{rad} + \gamma_{nr} \tag{4.1}$$

The fast lifetime in the several picosecond range is a clear indication of decay dominated by non–radiative processes. As mentioned previously the radiative lifetime of CNTs is predicted to be as high as 100ns [47, 39]. The mono-exponential character of the decay dynamics suggests that the emissive state is excitonic in its nature rather than free carriers. The latter is generally expected to lead to second order (i.e., nonmonoexponential) kinetics, unless free electron and hole concentrations are significantly imbalanced.

The histogram of lifetimes measured for 126 different $(6, 4)$ nanotubes within the same sample is given in Fig. 4.8. The distribution is centered at about 11 ps with a width of 16 ps. While no literature data exists for $(6, 4)$ nanotubes at room temperature, the average lifetime of 14 ps is in general agreement with values reported for other nanotube chiralities [62]. The corresponding distribution established for $(6, 5)$ nanotubes within the same sample results in an average lifetime of 5 ps and a similar width. Remarkably, this value agrees very well with the 6 ps determined by pump-probe

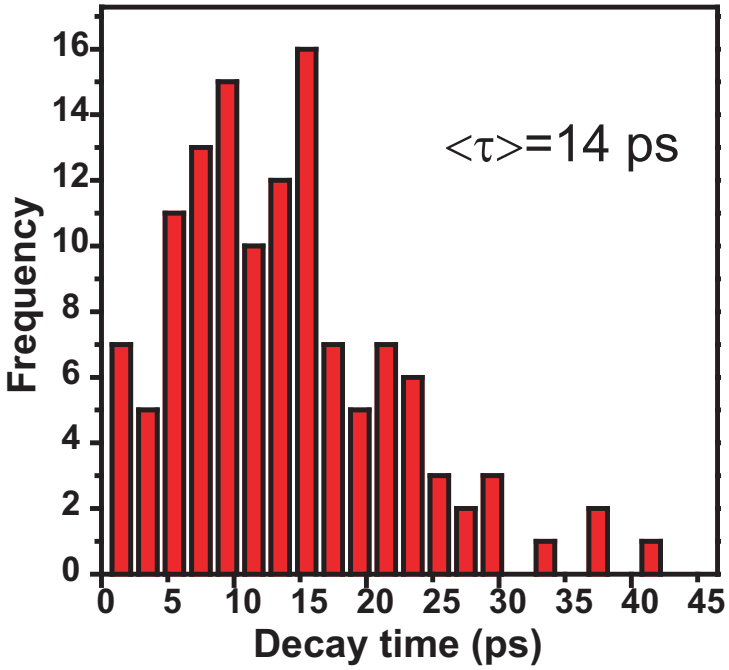

Figure 4.8: Statistical distribution of measured exciton lifetimes for 126 different (6,4) nanotubes. The distribution is centered at 11 ps with an average lifetime of 14 ps and a width of 16 ps.

measurements for the same CoMoCat nanotube material allowing for a direct comparison of the results achieved by both techniques [60]. On the other hand, ensemble measurements need to result in multi-exponential decay profiles in which fitted lifetimes will reflect summation over decay times with different contributions. Extremely long lifetimes in the range of nanoseconds as reported in the literature [64] have not been observed in our single nanotube measurements. In very few cases, less than 5 % of the measured transients, better fitting results could be achieved using multiple but similar decay times, probably because of spatial averaging along inhomogeneous nanotubes or the presence of a second nanotube within the detection area.

Before discussing the possible reasons of the lifetime distribution, we would like to shortly comment once again on the precision of our measurements and data acquisition. In Fig. 4.9 (a) two relatively fast transients are

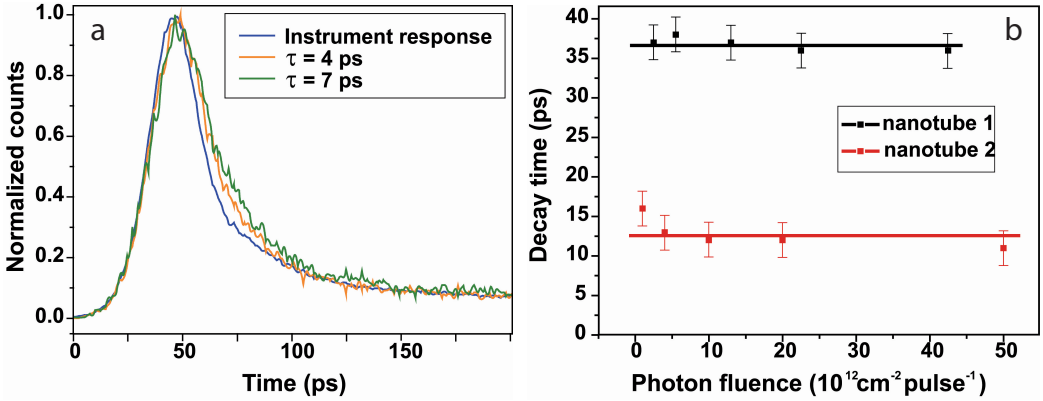

Figure 4.9: (a) Two relatively fast transient curves and the IRF. The difference in the width seen by the eye supports the precision of the fitting procedure, (b) the power dependence of the recombination time for two different tubes showing the absence of any additional processes associated with high excitation powers.

plotted for which the fitting procedure gives 4ps and 7ps decay times along with the instrument response function (IRF) of the APD and the TCSPC electronics. As it can be clearly seen these curves differ significantly in their width. This proves the high temporal resolution of the setup and accuracy of the performed statistical analysis. The Fig. 4.9 (b) shows the dependance of the decay times of certain tubes on the excitation power. The typical photon fluence used in these experiments is in the order of 10^{13} photons/cm^2 per pulse. It is known from previous studies that high excitation powers can affect the lifetime because of exciton–exciton annihilation processes [50, 51, 52, 87] giving rise to additional fast components. In fact, we have also observed such phenomenon, however at powers orders of magnitude higher than those plotted in the Fig. 4.9 (b). Therefore one can safely assume that lifetime variation observed here is not affected by multiexciton processes. In few cases we observed irreversible photodegradation of the nanotubes at highest excitation densities leading to reduced PL intensities and lifetimes.

4.3 Phonon Assisted Non–Radiative Relaxation

While it is clear from low quantum yield and from theoretical considerations that the fast relaxation is mediated by non–radiative relaxation channels the exact physical mechanisms of these relaxation are not known. Previously multi–exponential decay from ensemble samples have been observed and modeled with a sum of short decay constants in the range of our measurement [49]. In that work authors have speculated that the faster components are due to the additional decay channels provided by energy transfer in the residual small bundles. We cannot completely rule out the probability of having residual bundles in our samples due to limited spatial resolution and spectral range and have even observed in few cases several PL peaks for a single bright spot in the PL image. However, the occurrence of multiple PL peaks does not correlate anyhow with the observed lifetime. Therefore, we can state that while bundling can have an effect on the PL lifetime it does not play a major role in our experiments and cannot exclusively account for the lifetime variation.

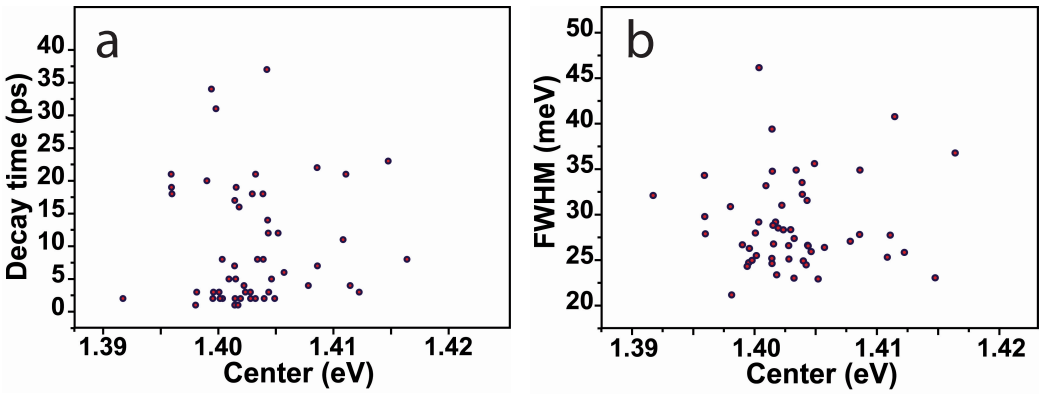

Figure 4.10: (a) Decay time of different (6,4) nanotubes versus their emission energy, (b) emission width versus emission energy. No correlation is observed suggesting that non–radiative relaxation channels are not affected by the environmental effects.

Another possible non–radiative relaxation channel for the optically active excitons is their transitions into optically inactive dark excitonic state, followed by a non–radiative relaxation to the ground state. In this case the variation of the lifetime could be explained by slightly different excitonic energies of the nanotubes caused by different dielectric environments. Namely, slight variations of the environment's dielectric constant can result in different screening of the excitons and thus different energies of the excitonic states. The variation of the splitting between the energies of the dark and bright exciton would in its turn affect the transition rates from bright state to the dark and vice versa. This would result in variation of the effective PL decay time of the bright state. If this is the case then we could expect that decay times of the CNTs should correlate with their spectral properties. To check this hypothesis in Fig. 4.10 we plot the observed decay times from the individual nanotubes versus their emission peak maximum (a) along with the plot of emission width versus emission energy (b). As it can be seen from these plots there is no obvious correlation which makes the aforementioned scenario unlikely.

On the other hand there is an interesting pattern when we plot the photoluminescence emission width of the nanotube against its decay time. While no exclusive 1:1 correlation could be observed, the long lifetimes were mostly associated with narrow emission linewidth and broad linewidth with short lifetimes (Fig.4.11). But what are the contributing factors in the homogeneous broadening (Γ) of nanotube PL? One of them is the finite lifetime τ of the exciton due to the Heisenberg uncertainty relation and the second is the exciton dephasing time T_{deph}

$$\Gamma \propto \frac{1}{\tau} + \frac{1}{T_{deph}} \tag{4.2}$$

As the measured τ lifetime of the exciton is in the order of several picoseconds, their contribution to the linewidth is negligibly small ($< 0.1meV$). Therefore the exciton dephasing is the dominating process controlling Γ. Dephasing times T_{deph} in the femtosecond range were predicted recently by the-

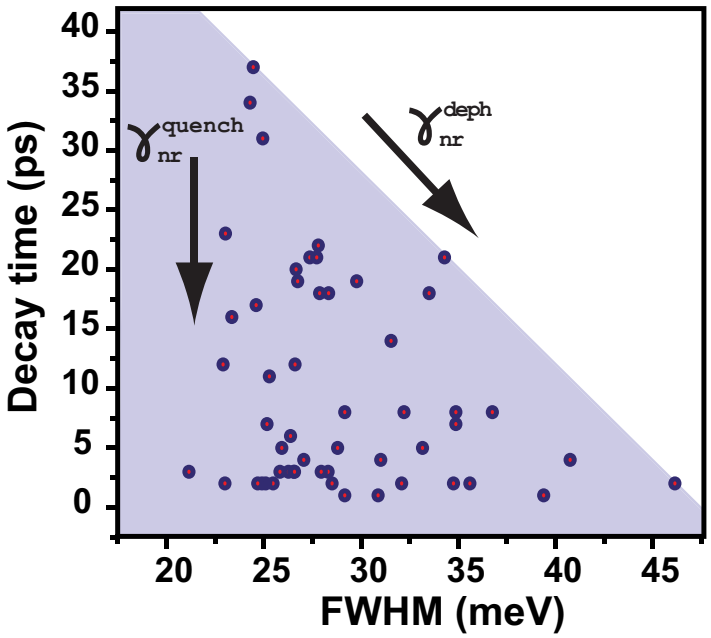

Figure 4.11: Correlation between spectral width of detected $(6, 4)$ nanotube spectra and lifetimes. Slow decay is observed for narrow linewidth and broad emission is associated with fast decay times.

oretical calculations [88] and were explained by the presence of structural defects. The local defect associated vibrational modes were suggested to couple with the excitonic states resulting in fast dephasing of the exciton and broad emission linewidth. The correlation observed here suggests that these local phonon modes also promote the non-radiative relaxation γ_{nr}^{deph} and their availability determines the excited state lifetime. But this obviously cannot be the only depopulation channel as the observed correlation is not linear but instead all the data points lay under the line that is determined by exciton–phonon coupling. Therefore, we speculate that certain type of defects simply quench the exciton γ_{nr}^{quench} while others contribute in both radiationless relaxation and dephasing. Thus the overall non–radiative rate is

$$\gamma_{nr} = \gamma_{nr}^{ideal} + \gamma_{nr}^{deph} + \gamma_{nr}^{quench} \tag{4.3}$$

where the γ_{nr}^{ideal} is the non–radiative decay rate of the ideal defectless nanotube. Thus we suggest a decay mechanism assisted by defect induced local phonon mode as one of the contributing factors to non–radiative relaxation. According to the recent calculations the multi–phonon scattering are expected to result in fast lifetimes in the case of localized excitons [89]. Thus the availability of more vibrational modes will enhance the coupling to the ground state.

4.4 Influence of the Nanotube Length

As mentioned in the previous section the quenching sites are expected to strongly affect the exction lifetime in the nanotube. It is well known that defects like vacancies, kinks, nanotube caps, heptagon–pentagon structures can change drastically the local electronic structure of the carbon nanotubes [90, 91, 92, 93]. In most of the cases a nonzero density of state near the Fermi level emerges as a result of a defect. Therefore, if the exciton spatially overlaps with such a state it can be easily quenched by non–radiative relaxation. By single nanotube quenching experiments using chemical treatment, it was shown [94] that the transport of strongly bound excitons is realized by a hopping mechanism rather than ballistic transport. In these experiments it was shown that the interaction of the nanotube with a single donor molecule that acts as a hole injector results in discrete stepwise reduction of the luminescence intensity. It was deduced that a single quenching molecule "switches off" a section of a nanotube that corresponds to the excursion range of the exciton. The excursion range was found to be around 90 nm irrespective of chirality. Thus, the motion of the excitons can be described as 1–dimensional diffusion with randomly distributed trap states or quenching sites. The lifetime of such a process will obviously heavily depends on the concentration of the traps. Hence, the different concentrations of trap states or perhaps different kinds of the defects present in the individual tubes can be a contributing factor in a lifetime variation.

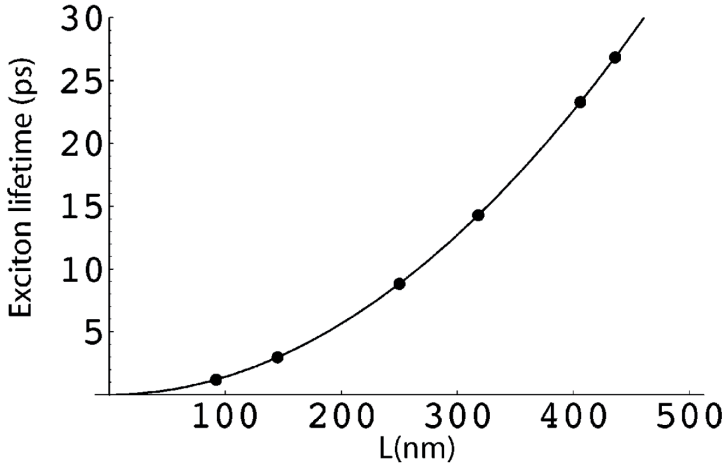

Figure 4.12: The predicted effective length-dependent lifetimes for excitons in (7,5) SWNTs. All lifetimes lie in the range of 1-27 ps in a good agreement with the experimental results. From [95]

Moreover, recent studies on ensemble samples based on the estimation of luminescence quantum yield of solutions with different average nanotube lengths have suggested that quenching of the exciton at the nanotube end can be *the only* non-radiative relaxation channel and that fast exciton lifetimes can be solely explained by finite length of the tubes [95]. Here authors speculate that excitons move diffusively rather than ballistically as quantum wavepackets spreading and assume that the exciton behaves as a fairly localized classical particle. They use the classical diffusion equation to describe the motion of the center of the exciton and non–radiative quenching at the nanotube ends.

$$\partial_t P(x,t;x_0,t_0) = D\partial_x^2 P(x,t;x_0,t_0) - k_r P(x,t;x_0,t_0) \tag{4.4}$$

where P(x, t; x0, t0) is the probability of finding an exciton at position x at time t, given that it started at x_0 at time t_0, D is the thermal diffusion coefficient and k_r is the radiative recombination rate. The following boundary conditions at the ends of the nanotube account for quenching:

$$\partial_x P(x,t;x_0,t_0) = k^e_{nr} P(x,t;x_0,t_0) \qquad at \qquad x = 0, L \tag{4.5}$$

The result of this one–dimensional diffusion is a non–linear trend in the dependence of the PL quantum yield versus the nanotube average length in the sample which explains fairly well their experimental observations. In addition, this simple model predicts the effective lifetime variation of the excitons depending on the nanotube length (Fig. 4.12). As it is evident from this dependence the lifetimes observed in our study could simply be explained by the presence of the nanotubes with different length from $\sim 100nm$–$\sim 600nm$ in our sample.

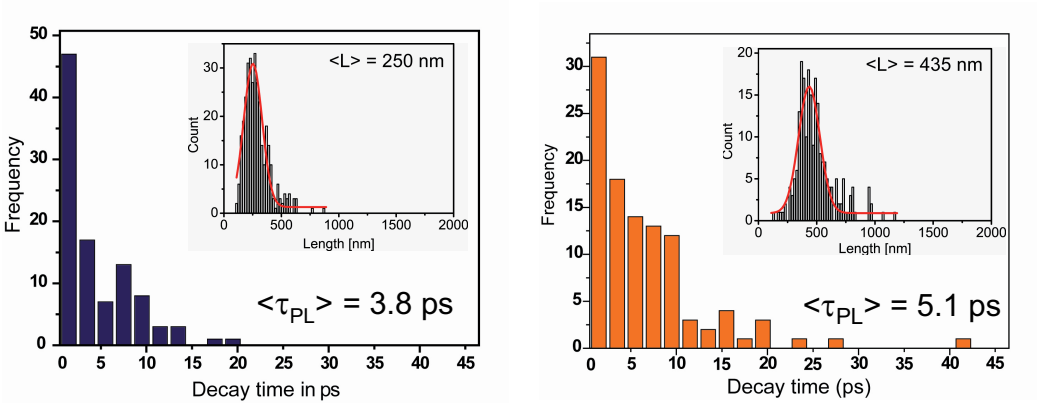

Figure 4.13: Lifetime distributions for samples with different lengths. Higher fraction of 'fast' tubes in the 'shorter sample' (a) compared to the 'longer sample' is due to quenching by the nanotube ends. In the insets the length distribution of two respective samples determined by AFM measurements is shown.

To examine this scenario we have preformed experiments with samples containing nanotubes with different length distributions (Dr. Frank Hennrich, Forschungszentrum Karlsruhe) [72]. Solutions containing different average length were prepared by size exclusion chromatography. Afterwards the length distribution of the sample was verified by AFM measurements. For each sample time–resolved PL measurements were performed for 100 individual nanontubes. In the Fig. 4.13 the results of such a statistics on the

lifetimes of two samples with different average length is depicted. In this example one sample contained tubes with an average length of $\langle L \rangle$=250nm (a) and another almost twice longer $\langle L \rangle$=435nm.

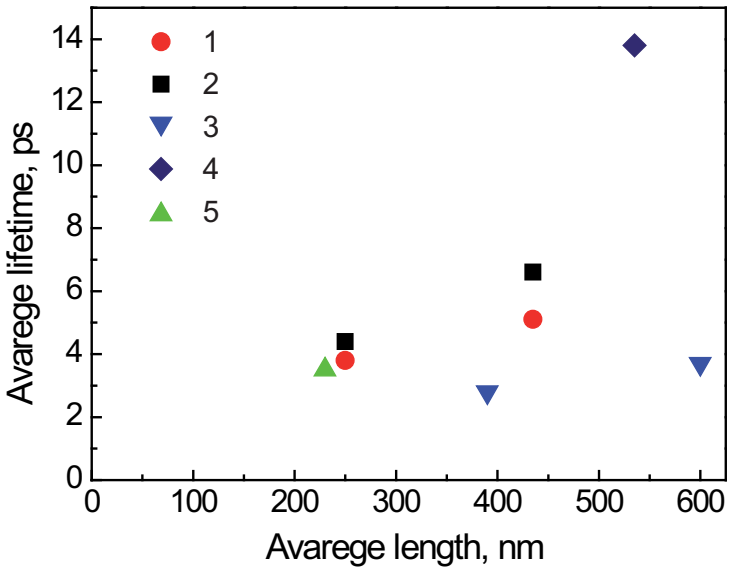

Figure 4.14: Average lifetime vs average length for different sample materials. For the materials prepared by the same method a variation of average lifetime is observed for samples with different average nanotube length.

The outcome of the lifetime measurements on this samples indicates that the length clearly has an effect on the average exciton decay time. However, this effect is not as decisive as predicted by the model and is not the only non-radiative channel. In the Fig. 4.13 the sample with long nanotubes shows longer lifetimes, the statistical distribution is shifted towards the longer lifetimes. The mean value for the decay times of 100 nanotubes for each sample is 3.8ps and 5.1ps respectively for samples with short and long tubes.

Fig. 4.14 shows the results of similar experiments on 8 different samples. The materials used here were CoMoCat tubes from different sources and were prepared following different procedures as follows.

1. CoMoCat tubes without surfactant (removed after sonication),from F. Hennrich, Forschungszentrum Karlsruhe (F.H.).

2. CoMoCat tubes with sodium cholate (SC) surfactant, F.H.
3. CoMoCat tubes with SC surfactant, different sonication procedure (mild sonication), F.H.
4. CoMoCat tubes with SC surfactant from A.A. Green and M.C.Hersam, Northwestern University.
5. CoMoCat tubes with SC surfactant, different batch, F.H.

Only data points marked with the same symbol had exactly the same origin and preparation procedure. One can see that for each such a pair of points the small effect of the length on the average lifetime can be observed. Nevertheless, there is no unique general correlation between the length and decay time for a given nanotube indicating that quenching at the nanotube ends is not the only contributing factor in the non–radiative relaxation process of the nanotubes' excited state.

To sum up, in this chapter we presented time–resolved PL measurements of a large number of single nanotubes at room temperature. In general, exciton decay is found to be monoexponential with decay times varying between 1 and 40 ps. Our measurements suggest a phonon–assisted mechanism and quenching at sites with vanishing bandgap as possible reasons causing this lifetime variation.

Chapter 5

Photoluminescence from Dark Excitonic States

5.1 Spectral Characteristics of Low Energy PL bands

Excitons determine all electronic properties of nanotubes. The unique structure of the graphene layer combined with the reduced dimensionality of the SWNTs leads to a manifold of excitonic states with different symmetries and multiplicities discussed in Chapter 2. This complex sequence of excitonic states and the non–radiative relaxation channels associated with them presumably have an important impact on the low PL quantum yield of SWNTs and fast exciton decay rates [61, 9, 96]. Detailed studies of the properties of dark excitonic states are therefore essential both for a complete understanding of the excited state dynamics and for, potentially, engineering of the optical properties of SWNTs.

The direct experimental evidence of the existence of dark excitonic states in SWNTs was presented applying two–photon photoluminescence excitation spectroscopy [8, 42] and measurements of magnetic brightening of the SWNT PL [97, 98]. Low-energy forbidden states were also used to explain the dynamics observed in pump–probe experiments [60, 59] and the temperature de-

pendence of PL intensities [99]. In addition, recent results on ensemble [100] and individual nanotube samples [101] have shown low energy satellite peaks in the PL spectra. These peaks were attributed to emission from low lying dark excitonic states while the mechanisms enabling optically forbidden transitions and the interplay between bright and dark excited states remain to be clarified.

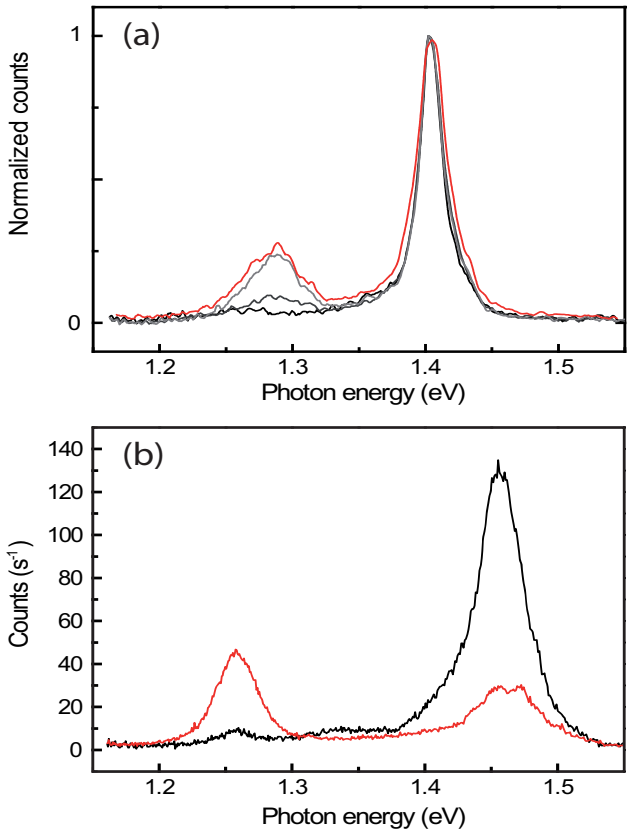

Figure 5.1: Creation of low energy satellites in the PL spectrum of a (6,4) SWNT (a) and a (5,4) SWNT (b). Initial spectra (black lines) acquired at low excitation intensity I_0=3·10^{13}photons/(pulse cm^2) and considerably modified spectra (red lines) of the same nanotubes acquired after exposure to high excitation intensities $\sim 17 \cdot I_0$.

In this chapter we characterize the creation of low-energy emission bands in the PL spectra of individual (5,4) and (6,4) chirality SWNTs upon high

power pulsed laser irradiation at room temperature [102]. The persistence of these bands in subsequent low power measurements indicates that irreversible distortions of the nanotube structure efficiently "brighten" forbidden states via disorder induced mixing of excitonic states in agreement with predictions made in [39, 47]. The unambiguous distinction between additional emissive features belonging to a certain nanotube and PL bands from other nanotubes is made possible by observing single nanotube spectra before and after high power irradiation and by recording the polarization dependence for bright and dark emission bands. Additionally, we show that similar low energy emission bands can be generated by adsorption of gold on SWNTs. This indicates the importance of spin polarized states created by metal atom adsorption or defect formation for brightening of dark states. Thus we suggest that low energy emission results from triplet exciton recombination facilitated by high spin density states and magnetic impurities. Time–resolved PL studies show that in the presence of defect–induced dark excitonic emission, the lifetime of the bright exciton is reduced significantly. Thus the defects increase the decay rate by introducing new non-radiative relaxation channels. Furthermore, we present the first time–resolved measurements of the dark exciton emission for individual SWNTs. While the mono–exponential decay times of the allowed transition are in the range of 1 to 40 ps (previous chapter) [103], far longer dark state lifetimes up to 177 ps have been observed. The evaluation of the dark exciton decay shows that this state is predominantly populated directly upon photoexcitation and not via branching from the bright exciton.

Fig.5.1 shows the generation of low energy satellite PL bands for two individual nanotubes. Initial spectra (black lines) acquired at low excitation power ($3{\cdot}10^{13}$photons/(pulse cm^2)) show a single emission peak centered at 1.41 eV (a) and 1.46 eV (b) assigned to the allowed bright exciton (BE) in (6,4) and (5,4) nanotubes, respectively [24]. Irradiation of the nanotubes for 10–100 seconds with an order of magnitude higher pulse intensity $\sim 5{\cdot}10^{14}$photons/(pulse cm^2) results in some cases in significantly

modified spectra (red lines in Fig. 5.1) with additional redshifted shoulders and new spectral features transferring substantial spectral weight to these satellite peaks. Importantly, no such spectral changes were induced at the corresponding averaged power levels using continuous–wave (CW) excitation suggesting that extremely high pulse intensities initiating multi-photon processes are crucial to induce these modifications. High power CW excitation, on the other hand, mainly leads to photobleaching and blinking of nanotube PL [104]. Satellite peaks for different (6,4) and (5,4) nanotubes consistently appear at similar energies and can be roughly divided into two groups with redshifts of $\sim 110-190$ meV (DE_1) and $\sim 30-60$ meV (DE_2) in good agreement with Ref. [101]. The same energy splittings (130 and 40 meV) were predicted theoretically for dark, non-emissive excitons in the (6,4) nanotube and were attributed to triplet and even parity singlet excitons, respectively [41]. Thus, as discussed in Chapter 2, due to the change in the symmetry of the nanotube structure and local spin density we lift the restriction of photon emission from lowest singlet A_2 and triplet excitons.

The polarization analysis of PL emission of the original BE peak and the newly created satellite DE_1 (Fig. 5.2) show the same $cos^2\theta$ behavior proving that the emission bands belong to the same nanotube and indicating that the redshifted emission originates from an intrinsic state of the SWNT.

Based on these experimental observations we conclude that during the intense irradiation the structure of the nanotube is modified by creation of local defect sites. These defects alter the local symmetry of the nanotube partially removing restrictions for the population and subsequent emission from intrinsic dark states [39] as discussed in Chapter 2.

The intensity of newly induced emission shows little correlation with the excitation power. The grey lines in Fig.5.1 (a) are the spectra acquired sequentially between initial and final spectrum at intermediate intensity $\sim 7 \cdot I_0$. The appearance of the emission is rather step-like and random. This kind of behavior is consistent with our interpretation of brightening of the dark states by introducing defect sites as the later process would obviously have

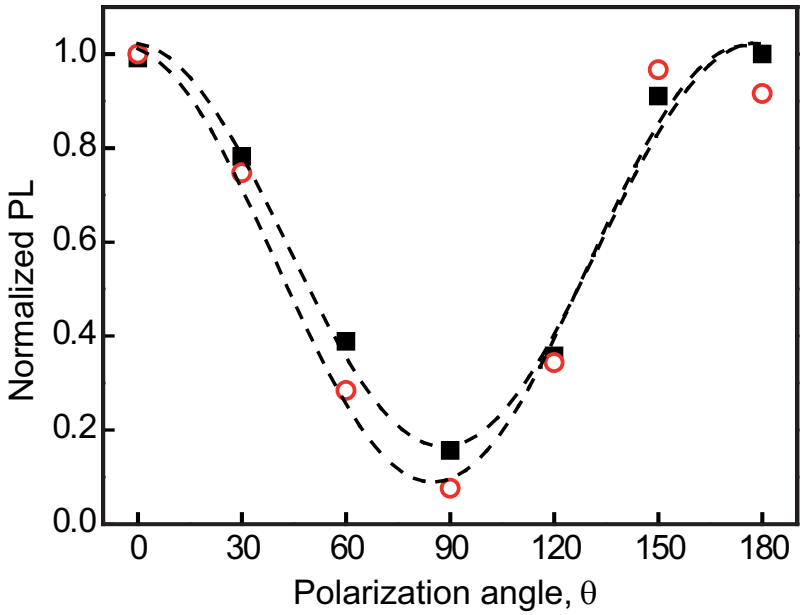

Figure 5.2: The polarization dependence of the PL emission for the bright exciton BE (open circles) and the dark exciton DE_1 (filled squares) determined from a series of spectra recorded for the same (6,4) nanotube. The dashed lines are $cos^2\theta$ fits to the data.

a random character as well. Although generally the spectral changes were irreversible, some nanotubes exhibited a reversible power dependence of the amplitude of the redshifted peak. This could indicate that some reversible structural defects are stable only at high thermal energies of the nanotube. While disorder can be inherently present in SWNTs due to e.g. the growth or post–processing and can lead to multiple PL peaks observed in the literature [105, 100, 101], their creation might be suppressed especially at low temperatures, where such effects were not observed under similar experimental conditions [106].

The possibility that the new PL emission is from outer shell of the double–walled nanotube (DWNT) that for some reason became emissive after laser irradiation is highly unlikely based on the small difference of the emissions' photon energy. If the two peaks would result from inner and outer nanotube

within a DWNT, their PL energies would be far more different based on the difference in diameter required to form such as structure. As an example, the outer shell nanotube for a (6,4) tube would need to have a diameter of $\sim 1,3$ nm corresponding to an emission energy at > 1500 nm. Moreover, the CoMoCat material used in the current study are practically free of DWNTs.

5.2 Population Dynamics of Dark and Bright Excitons

To determine the population dynamics of both dark and bright excitonic states and to study the effect of the created disorder we have performed time–resolved PL measurements of the different emission bands before and after creation of emission satellites. Fig.5.3 depicts representative PL transients detected from the shaded spectral areas (shown in the inset) for two individual nanotubes of two different chiralities: (6,4) (a) and (5,4) (b).

Black curves here show the decay of the BE state detected in the grey shaded spectral range in the insets before creation of the low energy satellites. Grey and red curves show the decay of the photoluminescence from respectively grey and red shaded areas in the spectra after the appearance of the new emission bands. Two important conclusions can be drawn from these data. First, upon creation of the satellite peaks the bright exciton lifetime is decreased compared to the initial decay, and second, the decay of the dark excitonic state DE_1, shifted by 110-190 meV with respected to the BE, is substantially slower. Monoexponential fits (dashed lines) to these transients give the lifetimes of the main emission peaks before and after creation of the redshifted band of 20 ps and 6 ps for the (6,4) nanotube Fig.5.3(a) and 13 ps and 2 ps for the (5,4) tube Fig.5.3(b), respectively. Importantly, the emission bands with smaller energy shifts in the range of several 10 meV (DE_2) show exactly the same decay behavior as the main peak, confirming that these states are in thermal equilibrium with the bright exciton at room temperature (data not shown) [47, 99, 107].

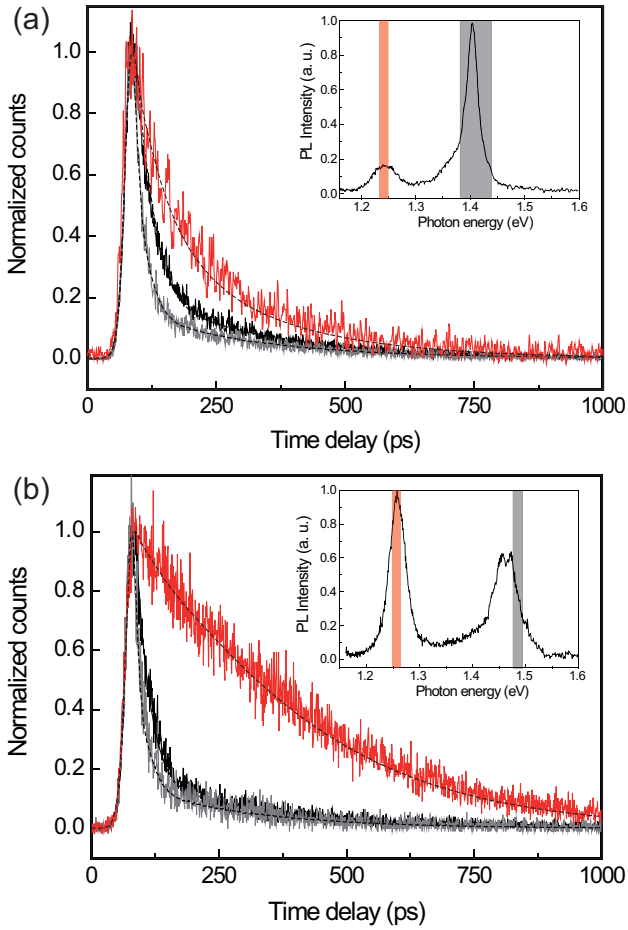

Figure 5.3: PL transients visualizing the decay dynamics of different emission peaks in the spectra of individual SWNT (inset) for two different chirality nanotubes: (6,4) (a) and (5,4) (b).

The decay of dark excitons DE_1 is dominated by much longer time constants, 65 ps and 177 ps for the (6,4) and the (5,4) nanotube in the present example, as would be expected for a weakly-allowed transition. Thus, other origins of the low-energy bands such as phonon replica and bi-excitons can be ruled out based on this slow decay dynamics. Additionally, we observed a fast decay component (8 ps and 2 ps) with far smaller photon flux (about a factor 1/20) possibly caused by heterogeneities along the nanotube introduced by the defects or by a more complicated structure of the DE_1 excitonic

manifold. Considering the large separation of the emission peaks and the detected spectral windows (shaded areas in insets in Fig. 5.3) overlapping emission contributions from the BE state appear not to be sufficient to explain this decay component. On the other hand, the decay dynamics of the dark exciton is possibly complex since it involves local defects controlling both initial population and PL emission by making the forbidden state weakly allowed and possibly also causing non-radiative quenching. Measurements on a number of other (6,4) and (5,4) nanotubes consistently show the same effects with dark exciton lifetimes ranging up to 177 ps. Decay times derived from time–resolved PL and pump–probe data in the range of 50 - 300 ps with small relative amplitudes have been reported before [49, 56] from ensemble samples as part of multiexponential decay. We speculate that these decay times could originate from the newly created states observed here.

Now we discuss the more rapid decay of the bright exciton in the presence of the redshifted peaks (Fig. 5.3). Since the amplitude of the BE peak is decreased we conclude that disorder induced defects are responsible for additional radiationless relaxation channels depopulating the bright excitonic state. Two competing channels can be distinguished. First, population transfer to the dark states DE_1 mediated by the introduced defects and secondly, decay to the ground state facilitated by enhanced exciton–phonon coupling due to the defect associated local phonon modes as discussed in Chapter 4 [88]. Both relaxation channels require diffusional motion of the bright exciton along the nanotube to enable interaction with localized defects, therefore faster decay also serves as an evidence for the mobility of excitons in nanotubes [9].

The population transfer from bright to dark states would result in a delayed rise of the DE_1 emission with a rise time equal to the decay time of the bright state. Such a delayed rise, that would be detectable in our measurements especially for nanotubes with relatively longer decay times of the BE state ranging up to 25 ps, was not observed suggesting that a substantial fraction of the dark state population is built up directly upon

photoexcitation. Importantly, the fact that the bright exciton maintains a different and finite lifetime in the presence of the dark state shifted by up to 190 meV clearly shows that these two states are not in thermal equilibrium. Possible transitions between the bright and low-lying dark exciton therefore need to occur on timescales much longer than several picoseconds.

5.3 The Mechanism of The Brightening of Dark Excitonic States

Having characterized the behavior of the new emissive states spectrally and dynamically the next very crucial question is the possible mechanisms of the defect creation by intense laser pulse and the properties of these defect sites enabling the coupling to the dark states. In this context it is very interesting to investigate the role of environment in the observation of the effect. To study this issue we have repeated our experiments with nanotubes coated with different surfactant and also embedded in different media.

Fig 5.4 shows PL spectra from a DNA wrapped nanotube embedded in Poly(methyl methacrylate) (PMMA) matrix. Here, an aqueous solution of DNA wrapped SWNTs was deposited on a microscope cover slide by spin-coating and was covered by a solution of 0.5 mass percent PMMA in toluene. The initial spectrum (black line) shows broad emission from the BE state, characteristic for DNA-wrapped nanotubes [108]. In the PL spectrum (red line) of the same nanotube after illumination with high power ($1.5{\cdot}10^{15}$photons/(pulse cm^2)) pulsed excitation at 1.63 eV the same new emission bands can be identified as in the case of nanotubes with sodium cholate as surfactant. Thus, the observation of the effect is not due to a chemical reaction specific to sodium cholate surfactant. On the other hand the isolation of the nanotube from the air by covering it with polymer or microscope immersion oil results in significant less cases of brightening of the dark states. One reason for this can be the lack of oxygens in the environment. Oxygen plays a critical role in the photochemical stability of

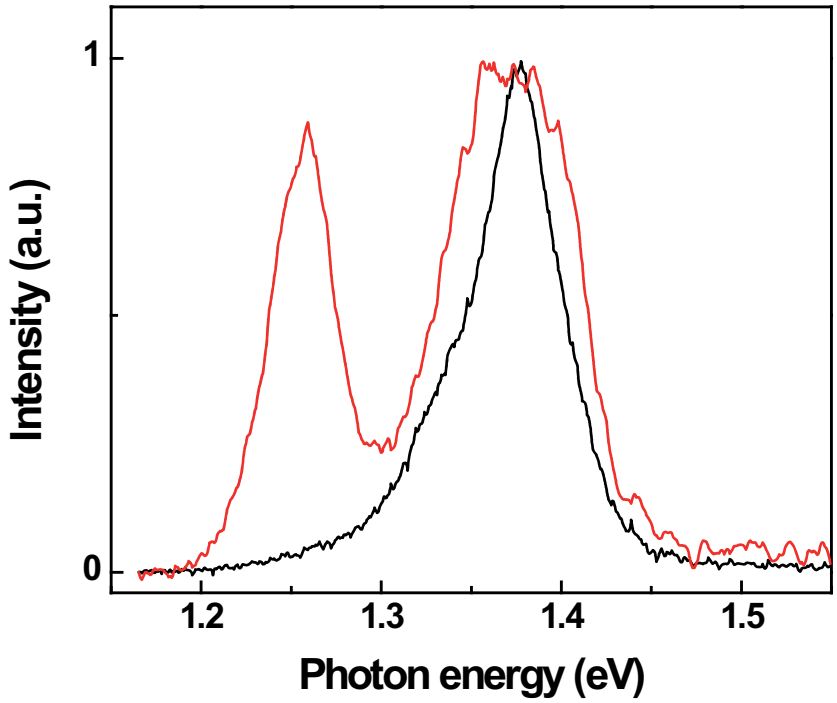

Figure 5.4: Photoluminescence (PL) spectra for an individual DNA wrapped (6,4) Single-Walled Carbon nanotube (SWNT) [71] covered by a thin layer of PMMA.

carbon nanotubes [104]. The availability of physisorbed oxygen appears to be controlled not only by the oxygen concentration in the atmosphere but also by the surface morphology and coverage. Our studies showed that both photobleaching and the creation of the dark state emission are suppressed by embedding nanotubes in quasi oxygen-free environments. Alternatively, the reason can be the different thermal conductivity of these media compared to the air. If the defects induced by the laser pulse are sidewall modifications of the robust sp^2 hybridized structure of the nanotube then the modification barrier, much bigger than the excitation photon energy, will probably be very sensitive to the thermal conductivity of the system.

Finally, the most intriguing issue of the novel emission is the nature of the excitonic state that it is originating from. The strongly polarized emission of the DE_1 state depicted in Fig. 5.2 makes the possibility of simply having lu-

minescent defects unlikely. Recent experimental studies on ensemble samples enriched with (6,5) chirality nanotubes have attributed low energy emission bands to K momentum $E_\mu(k_0)$ excitons described in Chapter 2 [109]. The authors speculate that though these excitons have higher energy than the emissive A_2 exciton they emit redshifted photons because of simultaneous emission of a phonon. They suggest that the absorption shoulder observed by many groups is the reverse process of simultaneous absorption of a photon and a phonon [75, 77]. Thus, by comparing the energy separation of the absorption and emission satellites with the main PL peak they identify the phonon with the energy of $\sim 167meV$ (D band, totally symmetric A_1' mode at K point) responsible for this phonon induced emission. However, from Fig. 5.1 b) it is evident the energy separation of the peaks can be as big as 190 meV, making the above mentioned scenarios impossible.

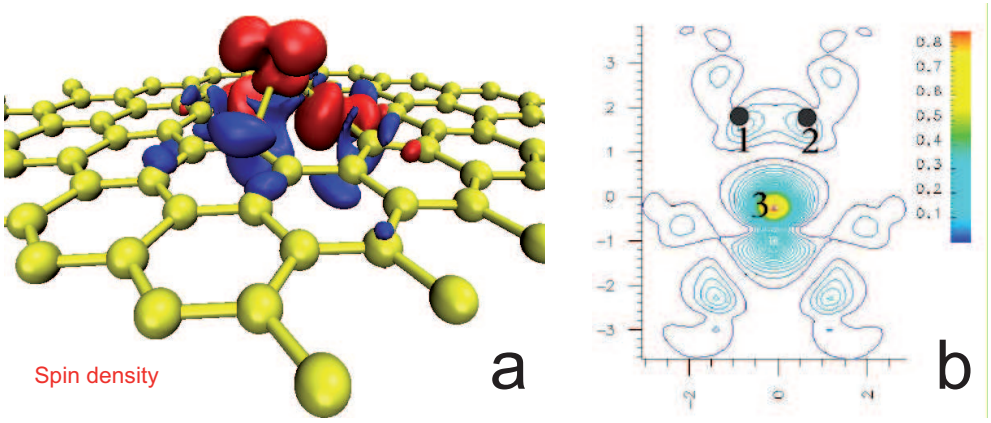

Figure 5.5: Theoretical calculations showing high spin densities at Au metal adatom site on graphene a), at the vacancy in SWNT lattice, from [110, 111].

On the other hand the energy separation for the triplet state calculated for the (6,4) chirality in Ref. [41] is in good agreement with our experimental data. The intersystem crossing leading to triplet emission can be assisted by coupling to high spin density states created by sidewall modification of the nanotube such as vacancy creation [111, 112]. The energy of about 5 eV needed to create a vacancy [111] can be provided through multi-photon exci-

tation processes explaining the high pulse energies required for the creation of DE_1. In general, magnetic impurities increasing spin-orbit coupling could also be formed by trace amounts of residual catalyst materials explaining the observation of dark state emission in other nanotube materials reported in literature. Fig. 5.5 shows the high spin densities formed as a result of adsorption of a gold atom on a graphene surface a) and at the vacancy on the sidewall of carbon nanotube.

To test the possibility of having an itersystem crossing in the nanotubes due to increased spin–orbit coupling we treated the SWNTs with a pH neutralized, aqueous solution of gold. The metal atoms, and in particular gold atoms, induce spin polarized states with significant magnetic moments when adsorbed on SWNT [113] or graphene surface [110]. The solution was prepared by reduction of $HAuCl_4$ by acetone and was pH neutralized by addition of NaOH [114]. The resulting solution was centrifuged to remove colloidal gold nanoparticles and was diluted with distilled water until a nearly transparent, violet solution was obtained. Strikingly, covering the sample with a gold solution results in similar changes in the single nanotube PL spectrum without requiring high power pulsed excitation (Fig 5.6) thus proving the triplet emission hypothesis. The efficiency of brightening of the dark states is especially high when the aqueous solution SWNTs is premixed with the gold solution before being spin coated on the substrate thus facilitating the surface adsorption of the metal. In the samples prepared with this procedure the majority of the (6,4) nanotubes exhibited low energy emission satellites, indicating that the same emissive DE_1 state is brightened. This has been further confirmed by time resolved measurements showing a broad distribution of lifetimes in the range of 7 to 150 ps, considerably longer than for the BE emission [103]. Thus this simple method allows tuning of the properties of the SWNTs' excited state.

Although the emission energy of the satellite peak and its lifetime leaves no doubt that with the treatment of gold solution the new emissive states have identical nature as in the case of high pulsed excitation there is a note-

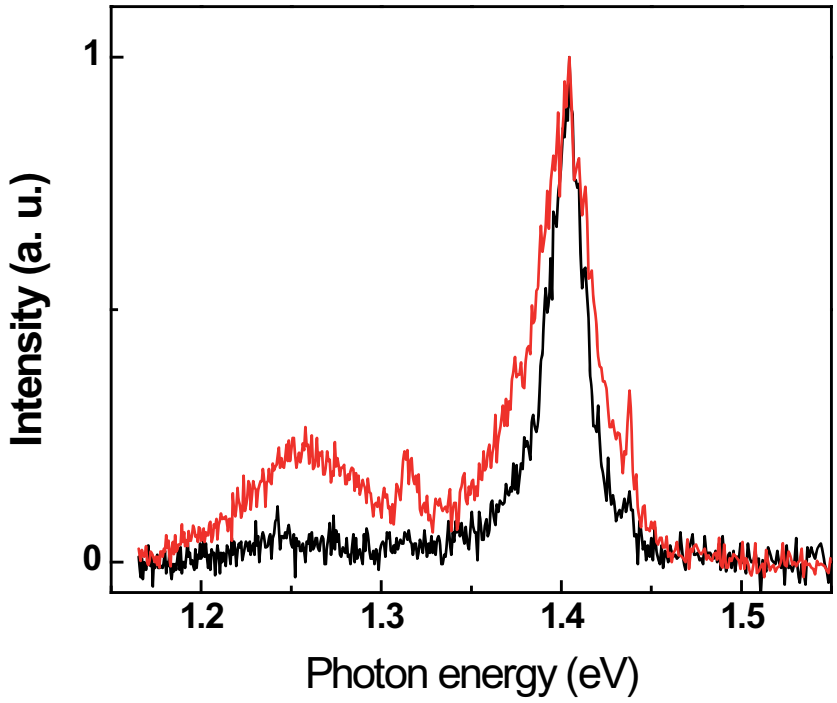

Figure 5.6: PL spectrum of an individual (6,4) SWNT before (black line) and after (red line) surface adsorption of gold atoms. The origin of the redshifted bands generated by this method was confirmed to be the same as in the case of high power pulsed excitation by time resolved PL measurements. The small features centered at 1.437 eV and 1.314 are G and G' Raman modes of the SWNT, respectively.

worthy difference between the two cases. After a gold treatment the new emission bands show pronounced spectral shifting and blinking even at low power cw excitation. As is shown in Fig. 5.7 the characteristic emission of DE_1 at 950 nm is varying with time and can be observed here in the time intervals 0-40 s and 100-160 s. This kind of behavior was observed for the high power pulsed excitation (without gold adsorption) far less frequently. This indicates that the adsorption of gold and the resulting interaction with the nanotube is less stable e.g. due to to the mobility of the adsorbed gold atoms on the nanotube surface [115].

Importantly, no additional PL bands have been observed in control exper-

iments on single nanotubes deposited on gold films as well as near-field optical experiments using sharp gold tips [108] indicating that the new PL bands are not created by metal surface induced electromagnetic field enhancement.

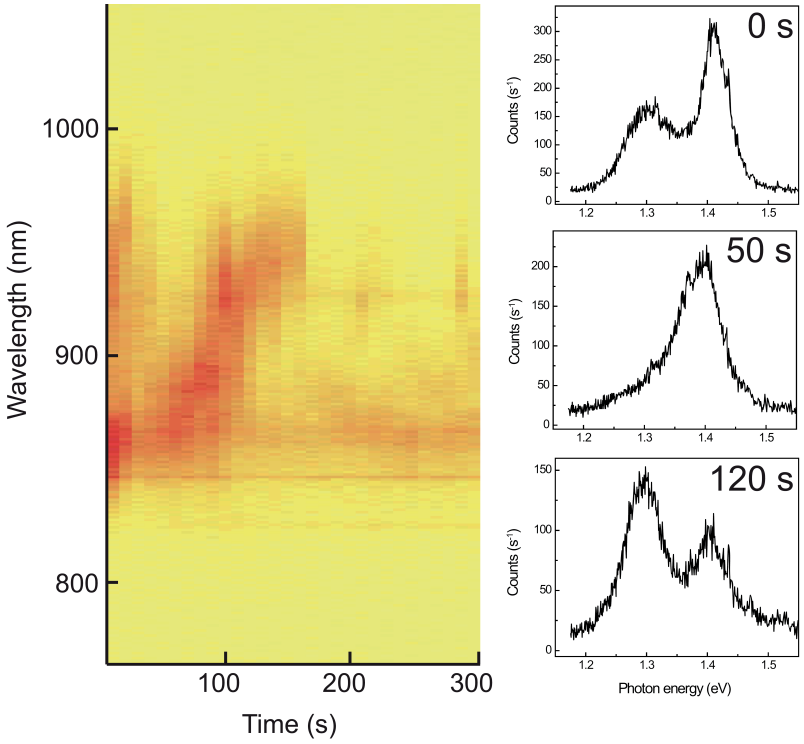

Figure 5.7: Series of PL spectra from a (6,4) SWNT after treatment with the gold solution. The series shows the temporal evolution of the emission with blinking and spectral shifts under low power CW excitation.

The lifetime of the triplet state around 100ps deduced from our experiments can seem to be somewhat faster than one would expect from such a system. On the other hand the theoretically calculated and experimentally estimated radiative lifetime of the bright singlet exciton is much longer than the measured excited state depopulation times indicating that the latter process is dominated by non–radiative relaxation. Therefore, though the radiative lifetime of the triplet state most probably would be much longer than several hundreds of picoseconds, the non–radiative depopulation of the state

is relatively fast resulting in the lifetimes measured here. Then a valid question arises: what is the origin of the difference between the lifetimes of singlet and triplet states if they are both dominated by non–radiative processes? The answer is probably hidden in the nature of the non-radiative process itself. If it is e.g. a phonon related process like multi–phonon scattering [89] then the differences will be determined by the different exciton–phonon coupling of the singlet and triple states.

5.4 Simultaneous PL and Raman Characterization of Defect Induction

Additional information on defect induced brightening of the forbidden exciton states can be obtain from inelastic Raman scattering measurements. Disorder or defects in carbon nanotubes are generally expected to result in increased D-band intensities in the Raman spectra [13]. Therefore, monitoring the intensity of the D-band during the creation of dark excitonic emission can further reinforce our arguments on defect induced brightening of originally dark states. To record Raman scattering spectra it is desired to have the excitation beam operated in CW mode as the short 150 fs excitation has a spectral width of 10 meV which would result in spectral broadening of Raman bands. As the scattering signal from single nanotubes is relatively small its spectral broadening can decrease the signal-to-noise ratio below the detection limit. The next prerequisite for obtaining high–quality Raman data spectrally well separated from the PL, the fundamental photon energy should match the E_{22} transition of the nanotube. On the other hand for a modification of the nanotube structure a pulsed excitation is needed. To combine all these requirements we have implemented a new excitation arm in the experimental setup consisting of a HeNe CW laser operating at 594 nm that matches the second excitonic transition of (6,4) tubes and combined it with the Mira laser beam with a beamsplitter. Thus after each irradiation cycle with a pulsed laser the Raman and PL spectrum were recorded with

CW excitation.

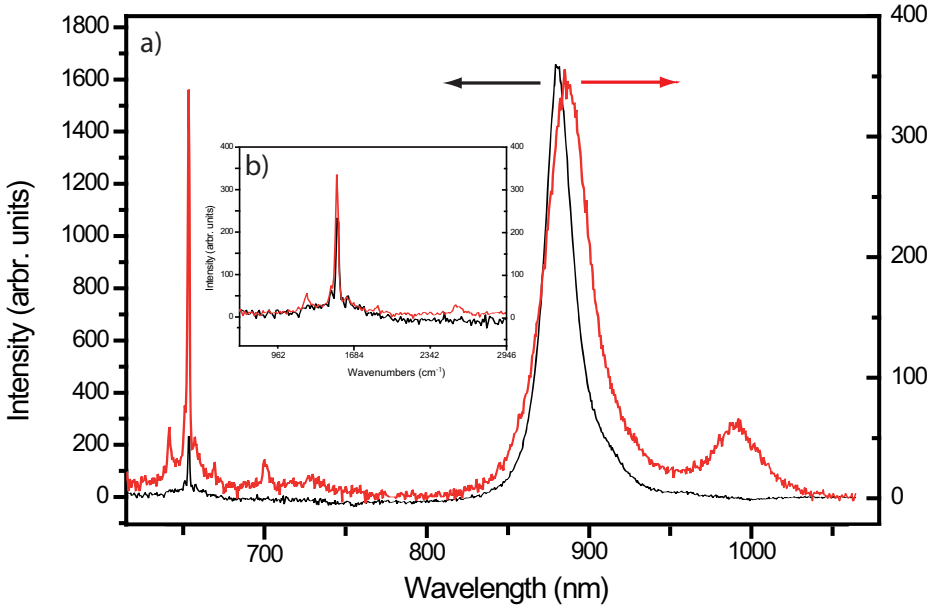

Figure 5.8: a) Raman- and PL spectra of a single DNA-wrapped (6,4) SWNT before (black line) and after (red line) exposure to high power pulsed laser irradiation at 760 nm ($6 * 10^{13}$ $photons/(pulse * cm^2)$) for 20 s. Both spectra have been acquired using 594 nm CW excitation with a power of $81\mu W$.

The Fig 5.8(a) visualizes the modification of both the Raman signal and the PL as a result of high power pulsed excitation. A new emission band is introduced in the DE_1 spectral region and significant changes in the corresponding Raman spectrum can be observed. While the initial spectrum in Fig 5.8(b) (black line) shows only weak intensities for the D- and G'-Raman modes at 1300 cm-1 respectively 2600 cm-1, those bands are increased in the modified spectrum (red line). An increase in the intensity ratio I(D)/I(G), which can be attributed to the introduction of additional defects [13], can be observed. The relative decrease of PL vs. Raman scattering here indicates a reduction of photoluminescence quantum yield.

Fig. 5.9 shows another example of relative increase of I(D)/I(G) intensity ratio accompanied with the appearance of new low energy PL bands. In ad-

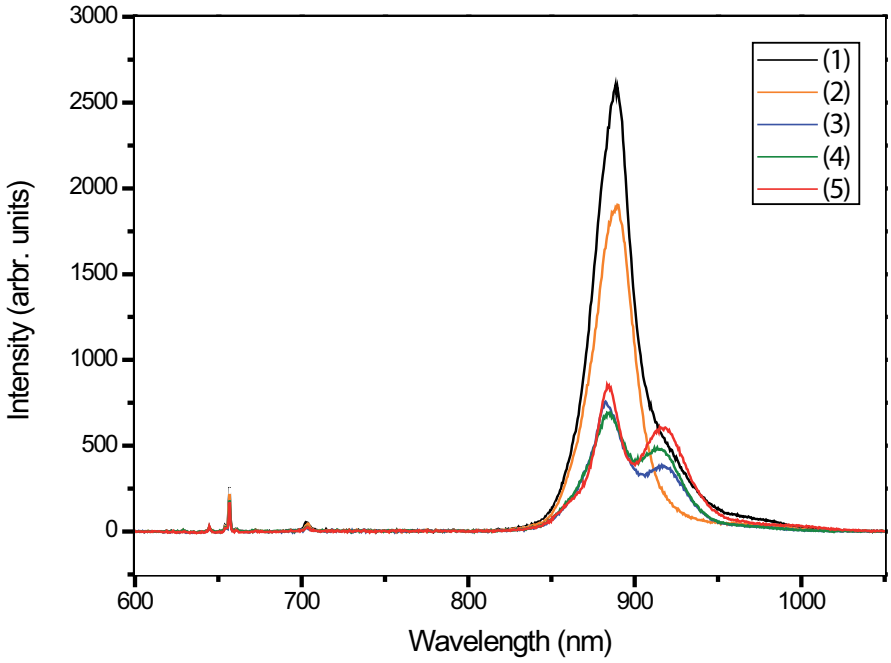

Figure 5.9: Series of Raman- and PL Spectra obtained for a single DNA-wrapped (6,4)-SWNT after consecutive illumination for 20s with high power laser pulses at 760 nm ($6 * 10^{13} photons/(pulse * cm^2)$). The spectra have been acquired using 594 nm CW excitation with an excitation power of 81 μW.

dition to photobleaching a new PL-emission band in the DE_2 spectral region is created upon pulsed laser excitation. Further illumination only results in changes of the BE/DE_2 PL-intensity ratio. Fig. 5.10 shows magnified Raman spectra of Fig. 5.9. The first order Raman modes D (b) and G (c) and the second order band G' (2600 cm^{-1}) are found to be modified after each illumination period with the pulsed laser. An overall increase in the D-band intensity and decrease in the G-band intensity can be observed (spectrum (1) to (5)), which results in an increase of the I(D)/I(G) ratio, indicating an introduction of additional defect sites.

These changes in the I(D)/I(G) ratio however cannot be attributed to the creation of the new emission bands exclusively, as they also occur for pure

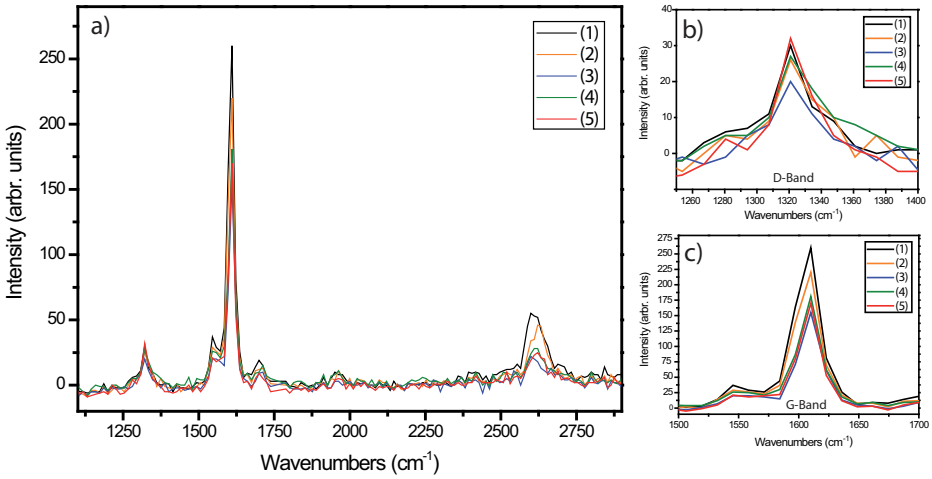

Figure 5.10: a) Magnified Raman spectra of Fig. 5.9 showing an increase of defect–induced D mode upon excitation with intense pulsed laser beam.

photobleaching. In Fig.5.11 the steady decrease of the PL intensity is accompanied by changes in the corresponding Raman spectra. These spectra were obtained with CW excitation without pulsed irradiation. The defect related D-Raman mode is increasing, resulting in an increase of the I(D)/I(G) ratio. Thus, the quenching sites, that decrease quantum yield of the nanotube, are obviously defect sites and also contribute in D-band intensity making its one-to-one correlation with the occurrence of the dark excitonic bands difficult.

While these data clearly confirm our assignment of the new emission band to result from introduction of disorder, no additional information on the details of the structural or chemical nature of the defect can be obtained. Besides the increase of the D/G-ratio, no other significant changes have been observed in the Raman spectra.

In conclusion we demonstrated that nominally dark excitonic states in carbon nanotubes can become emissive after exposure to high excitation intensities and by adsorption of gold. The lowest–lying PL emission band is attributed to the luminescence from triplet excitonic state never observed before. We suggest that local defects induce mixing of different excitonic states

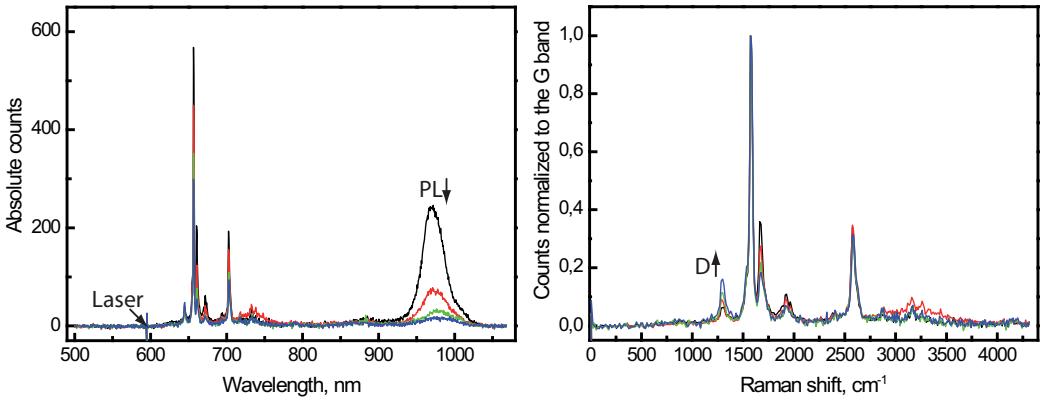

Figure 5.11: Bleaching of a (6,5) DNA-wrapped CoMoCat SWNT excited at 594 nm (cw) with an excitation power of 50 W. Each spectrum was obtained by integrating for 30 s.

and relaxation of selection rules via perturbation of the electronic structure. Our single nanotube measurements show that the recombination time of the excitons can be modified by the presence of disorder and that PL from the same nanotube can have decay rates varying by 2 orders of magnitude depending on the detected spectral range. In addition to fundamental interest, these results also have significant implications for nanotube opto-electronics because the approach provides a route of engineering SWNT optical properties in a manner not available previously.

Conclusions

The carbon nanotubes are unique systems that combine the well known properties of the solid state materials with those characteristic for the single molecules. The fascinating optical properties that emerge as a result of this combination lead to intriguing and sometimes unexpected and unusual phenomena. One of such surprising properties is the very low quantum yield (QY) of the nanotubes and a fast depopulation of its excited state, $\sim 10^4$ times faster than their radiative lifetime. However, despite such a low QY of the material we have succeeded in measuring time–resolved luminescence from single nanotubes at ambient conditions using a confocal microscopy. We have shown that exciton dynamics follow a fast monoexponential decay with varying time constants for different individual nanotubes. Our findings suggest that this fast decay is a result of multiple contributing factors. We have shown that the exciton lifetime correlates with the number of the available local, defect induced, vibrational modes through the PL spectral width. Thus, one of the channels of ground state recovery in the nanotubes was identified as a phonon-assisted mechanism. However, we have shown additionally that this is not the only non-radiative relaxation channel for the excitons. Our studies on samples with different average nanotube length have revealed a dependence of the excited state lifetime on the nanotube length. In agreement with the generally accepted picture of a mobile exciton randomly hopping along the nanotube axis we have attributed this dependence to the quenching of excitons at the ends of the nanotube where its band gap vanishes. Thus, the longer is the nanotube the longer "lives" the exciton.

The next fascinating property of the carbon nanotubes explored in this work is the possibility of tuning its optical properties by changing locally its structure. We have shown that those excitons that were thought to be non-emissive in ideal case due to the symmetry of their wave function or the total spin quantum number, can turn into emissive if there is a local perturbation of the electronic structure of the nanotube. The PL spectra of semiconducting nanotubes were modified and new emission bands were created by introducing disorder in the sidewalls of the nanotube due to intense laser excitation and by adsorption of metal atoms on nanotube surface. As in both of these cases not only the local symmetry of the excitonic wave function is altered but also spin polarized states are created we have identified the lowest PL band as an emission from triplet state. The nature of the state was further confirmed by measuring its lifetime which was up to two orders of magnitude longer than the decay time of the bright state. This finding explains the long standing issue in the literature on the origin of long lived components in the time–resolved PL measurements on ensemble samples. The existence of such components gave rise to many speculations and different models for the excited states dynamics. The main suggestion was that these long lifetimes with very small relative amplitudes should be attributed to the true radiative recombination of the bright state. However, our single molecule experiments have shown that different excitonic states from the same nanotube can have very different decay times. Additionally, we have shown that it is possible to modify the lifetime of the excitonic state. Upon introducing additional defect sites by intense pulsed laser irradiation the observed exciton decay times became faster than were initially, proving the importance of the defect concentration present in the nanotube as discussed in the first part of the work.

Appendix A

Rayleigh Imaging of Graphene and Graphene Layers

As discussed in the first two chapters of this work graphene is a parent material for carbon nanotubes. Here we present optical contrast measurements on graphene and graphene layers resting on a dielectric substrate. Using white-light elastic scattering (Rayleigh) microscopy we demonstrate that a single atomic layer can be "optically visible" due to interferometric enhancement of the signal. For a few layers the contrast is found to be linearly dependent on the number of layers indicating that the optical properties of graphene layers are not altered heavily by interlayer interactions.

Graphene is a newly emerging material with unique and fascinating properties and promising future applications [18]. Its electron transport is described by the (relativistic-like)Dirac equation, and this allows access to the rich and subtle physics of quantum electrodynamics in a relatively simple condensed matter experiment [116, 117, 118, 119]. The scalability of graphene devices to true nanometer dimensions [120, 121, 122] makes it a promising candidate for future electronics because of its ballistic transport at room temperature combined with chemical and mechanical stability. Remarkable properties extend to bilayers and few layers [123, 117].

Three main routes are possible for graphene sample preparation. The first

method is the micromechanical cleavage of graphite [116]. In this relatively straightforward method high quality graphite is placed between two pieces of adhesive tape and cleaved multiple times. Thus, among other thicker layers single layer graphene is also produced and can be identified if adhesive tape is solved in a solution and the material sticking to it is deposited on the substrate. The graphene samples used in the current study were produced by this procedure. Alternative methods include chemical exfoliation of graphite [124] or epitaxial growth by thermal decomposition of SiC [125].

Although being a very cheap way to obtain graphene the micromechanical cleavage has a very low yield as the graphene is a minority among thicker layers produced by this approach. Moreover, the identification of a single layer in an optical microscope is a very difficult and on most of the substrates an impossible task. Currently, optically visible graphene layers are obtained by placing them on the top of oxidized Si substrates with typically 300 nm SiO_2 and these substrates were used in the current work. For the unambiguous determination of the graphene flake thickness the AFM is used. However AFM measurements have several difficulties, including differences between the apparent and real height due to substrate interaction [116], that make other additional characterization of the layer thickness desirable. High-resolution transmission electron microscopy is the most direct identification tool [126], however, it is destructive and very time-consuming, being viable only for fundamental studies.

Optical detection relying on light scattering is especially attractive because it can be fast, sensitive, and not destructive. Light interaction with matter can be elastic or inelastic, and this corresponds to Rayleigh and Raman scattering, respectively. Raman scattering has recently emerged as a viable, nondestructive technique for the identification of graphene [127]. Depending on the shape of the G' (alternatively 2D) peak the thickness of up to 10 layers thick graphitic flake can be determined. However, Raman-scattered photons are a minority compared to those elastically scattered. Here, we show that the elastically scattered photons provide another very efficient and quick

means to identify single and multilayer samples and a direct probe of their dielectric constant.

Rayleigh scattering was previously used to monitor size, shape, concentration, and optical properties of nanoparticles, carbon nanotubes, and viruses [128, 129, 130]. Rayleigh scattering experiments can be performed by using two different strategies. In one, the background signal is minimized by making free-standing samples, as done in the case of carbon nanotubes [131, 132], or by dark-field configurations[133]. Alternatively, the background intensity is utilized as a reference beam, while the sample signal is detected interferometrically [128, 129, 130]. Here, we combine the second approach with the interferometric modulation of the contributing fields and show that the presence of a background is essential to enhance the detection of graphene over a certain wavelength range.

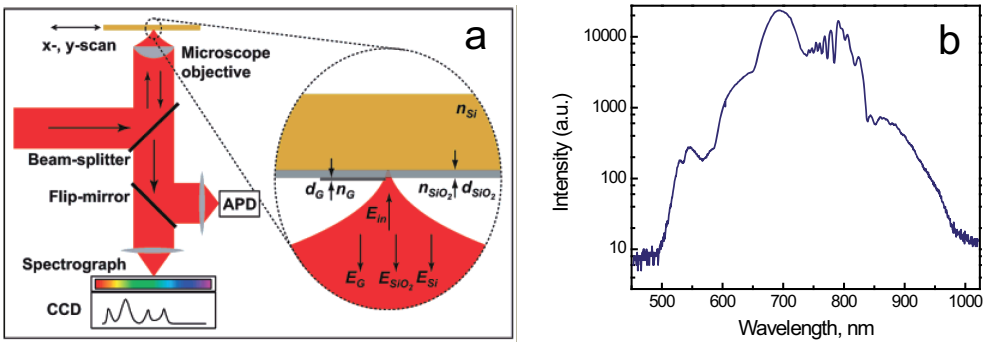

Figure A.1: a) Schematic experimental setup for Rayleigh scattering spectroscopy. The inset shows a cross–sectional view of the interaction between the optical field and graphene deposited on Si covered with SiO_2. b) A spectrum of the supercontinuum white-light laser source generated by the photonic crystal fiber

The schematics of the experimental setup used in these experiments is depicted in Fig. A.1. To measure the contrast of the graphene layers at different wavelengths the sample is illuminated with a collimated white-light supercontinuum. To generate the coherent white–light pulses a photonic crystal fiber(PCF) is placed in the excitation path and the output of the

Ti:Sapphire laser operated at 760 nm is focused by a focusing objective on the entrance facet of the fiber [134]. A cascade of nonlinear effects in the PCF give rise to a spectrum extending from the visible to the near infrared (Fig A.1 b). The divergent beam at the output of the fiber is collimated by two positive lenses in a telescope configuration. The beam is focused on the sample and the signal is detected by a spectrometer (CCD) and/or the APD as described in the experimental chapter. In the case of imaging with the CCD the full spectrum of the white–light reflected by the sample is acquired at each position during the raster scanning. The image is formed by integrating the intensity of the reflected light over the desired spectral window. The acquisition time per pixel is few milliseconds and the spatial resolution is $\sim 800nm$.

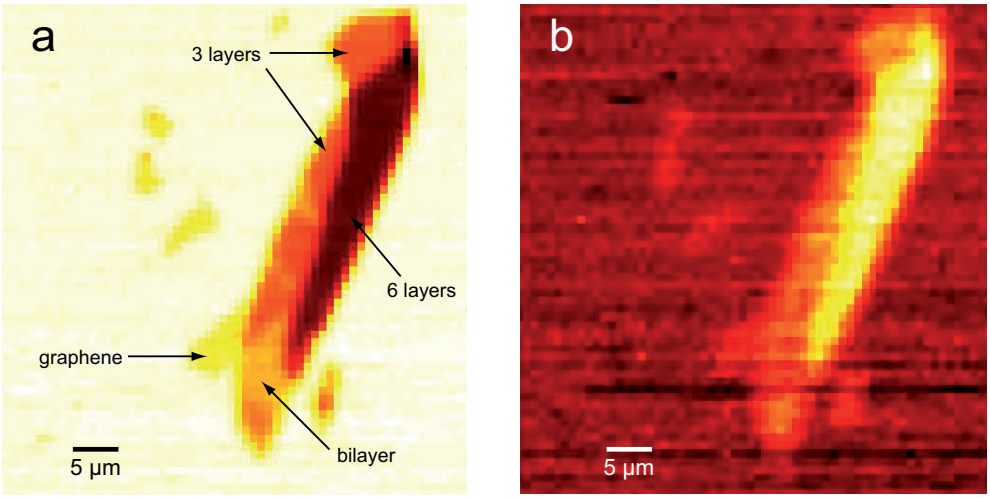

Figure A.2: Confocal Rayleigh imaging of graphene with white–light. a) Contrast at 546nm -585 nm, b) at 812nm - 850nm

The main difference in this experimental configuration is that one must use an air objective to illuminate the sample in contrast to the previous studies on SWNTs. As the substrate consists of Si covered with a 300 nm SiO_2 and the graphene resting on top of it, the illumination of the sample through the holder is no more possible due to the opacity of the Si. This makes the use of the oil immersion oil objective impossible for this experi-

ments reducing the NA to 0.95. However, the high NA is no more critical in these kind of experiments as the signal is not as small as in the case of single nanotube emission and can be arbitrarily enhanced by increasing the power of the excitation beam. Moreover, as numerical calculation show the decrease in NA increases the contrast in these type of experiments [12].

Fig. A.2 shows the image of a graphene flake integrated for two different spectral windows 546nm -585 nm a) and 812nm - 850nm b). The contrast of the flake depends on its thickness, smaller number of graphene layers having smaller contrast. This simple dependence of the contrast on the sample thickness does not hold for thicker flakes as will be discussed later. This is an important point and one should keep it in mind while identifying of the flake thickness by eye in the optical microscope. The color of the flake can be deceptive changing from blue to yellow to gray, i.e the darkness of the flake does not necessarily correlate with its thickness. The number of layers at different parts of the flake are indicated in the Fig. A.2 a) 1, 2, 3 and 6 layers, and were determined independently by AFM and Raman spectroscopy (by Dr. Cinzia Casiraghi, University of Cambridge). Thus, the contrast of the same flake can be negative (intensity from the flake is higher than from the substrate) or positive depending on the wavelength of the imaging beam.

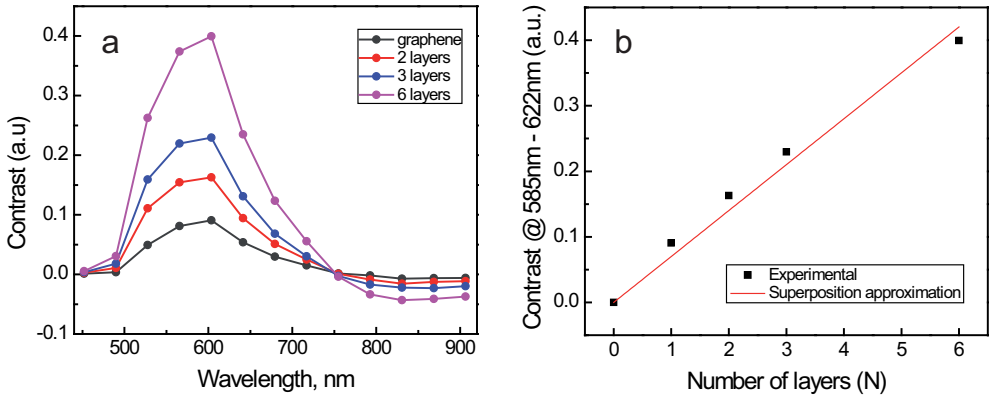

Figure A.3: White light imaging of graphene. a) Contrast 546nm -585 nm, b) 812nm - 850nm

Fig. A.3 shows the dependence of the graphene layers' contrast on the

imaging beam wavelength. The contrast δ is defined as the difference between substrate and sample intensity normalized to the substrate intensity (Eq. A.3). To increase the signal to noise ratio the intensity of the signal from 16 scan points were averaged for a given layer thickness. To minimize the inaccuracies arising from the white–light intensity instability the the reference (substrate) and signal intensity were taken from the same scan line. From the Fig. A.3 can be concluded that (i) the maximum of the single layer contrast is at 585nm - 622nm and is ~ 0.09, (ii) the contrast scales with the number of layers, (iii) there is no phase shift in this layer thickness range.

The formation of the contrast and its sign can be understood in the terms of interference from multiple reflections. The inset in Fig. A.1 shows a schematic of the interaction between the light and graphene on $Si + SiO_2$. When the light impinges on a multilayer, multiple reflections take place [135]. Thus, the detected signal (I) results from the superposition of the reflected field from the air–graphene (E_G), graphene–SiO_2 (E_{SiO_2}), and $SiO_2 - Si$ interfaces (E_{Si}). The background signal (I_{Bg}) results from the superposition of the reflected field from the air–SiO_2 interface and the Si substrate. Theses complete quantitative calculations can be found in our original publication [12] and its central result is depicted in Fig.A.4 b).

Here we present a simplified picture that captures the basic physics and illustrates why a single atomic layer can be visualized optically. The field at the detector is dominated by two contributions: the reflection by the graphene layer and the reflection from the Si after transmission through graphene and after passing through the SiO_2 layer twice. Thus, the intensity at the detector can be approximated as:

$$I \sim |\vec{E}_G + \vec{E}_{Si}|^2 = |\vec{E}_G|^2 + |\vec{E}_{Si}|^2 + 2|\vec{E}_G||\vec{E}_{Si}| \cos\phi \qquad \text{(A.1)}$$

where ϕ is the total phase difference. This includes the phase change due to the optical path length of the oxide, d_{SiO_2}, and that due to the reflection at each boundary, ϑ_{Si} and ϑ_G:

$$\phi = \vartheta_G - (\vartheta_{Si} + 2\pi n_{SiO_2} 2d_{SiO_2}/\lambda_0) \tag{A.2}$$

where n_{Sio_2} is the refractive index of the oxide and λ_0 is the wavelength of the light in vacuum. Assuming the field reflected from graphene to be very small, $|E_G|^2 \simeq 0$, the image contrast δ results from interference with the strong field reflected by the Si:

$$\delta = (I_{Si} - I)/I_{Si} \simeq -2|\vec{E}_G|/|\vec{E}_{Si}| \cos\phi \tag{A.3}$$

The sign of δ depends on the sign of $\cos\phi$, which is given by Eq.A.2. The reflectance, R, is the ratio between the reflected power to the incident power [135]. Assuming the Si reflectance as one, Eq. A.3 can be written as:

$$\delta = -2\sqrt{R_G \cos\phi} \tag{A.4}$$

where R_G is the reflectance of graphene. This is in turn related to the reflection coefficient r_G [135]:

$$r_G = \sqrt{R_G \, exp(i\vartheta_G)} \tag{A.5}$$

Eq. A.4 shows that the main role of the SiO_2 is to act as a spacer: the contrast is defined by the phase variation of the light reflected by the Si. Thus, the contrast for a given wavelength can be tailored by adjusting the spacer thickness or its refractive index.

Thus, from Eqs. A.2 and A.4 and assuming $\vartheta_{Si} = \pi$ (phase change upon reflection from optically denser medium [135]), the phase of graphene is $\vartheta_G \simeq \pi$, as expected for an ultrathin film where the absorption losses can be neglected [135]. The contrast decreases in the near IR because the wavelength becomes larger than twice the optical path length provided by the SiO_2 spacer. From Eqs. A.4 and A.5 and taking $\cos\phi = -1$ at maximum contrast (at $\lambda_0 \simeq 570nm$ Fig. A.3 a)) we get r_G= 0.05 and R_G=0.003.

Though this simple model is sufficient to describe qualitatively the optical properties of the few layers of graphene, it certainly needs additional

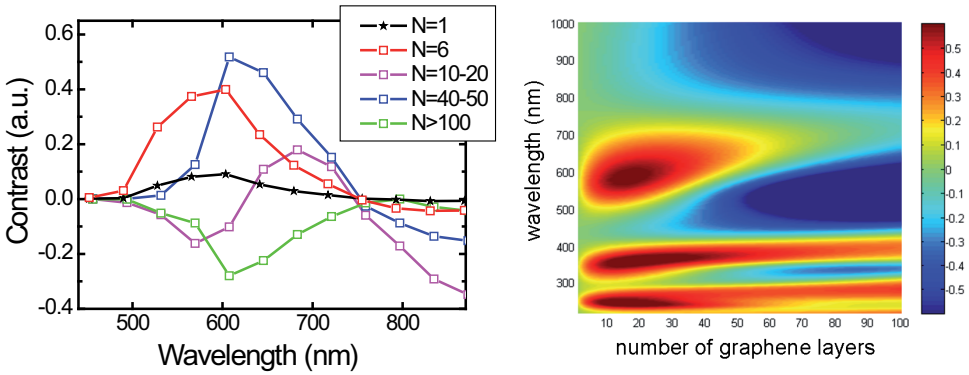

Figure A.4: a) Experimental contrast of the thicker graphene layers. b) Calculated contrast as a function of number of graphene layers (N) and excitation wavelength, from [12]

development to predict the quantitative behavior of the signal and the cases of the thicker layers. The contributions like the absorption losses within the layers, numerical aperture of the experiment, the Gaussian profile of the beams intensity has to be taken into account. Fig. A.4 a) visualizes the contrast dependence for graphene flakes thicker than 10 layers compared with the single and 6 layers. Here we see that a phase change due to the optical path in graphite emerges. As is evident from the theoretical calculations A.4 b) (Dr. E. Lidorikis, University of Ioannina) at the wavelength with maximum contrast for graphene, the contrast first saturates as N increases, then decreases and red-shifts, finally becoming negative, as found experimentally. It is also interesting to note that, for small N, the variation along the vertical (wavelength) axis is largely between zero and positive (i.e., reflectivity reduction only), while for a large number of layers, the variation is from positive to negative (i.e., both reflectivity reduction and enhancement). This points to two different mechanisms. For small N, the effect of the graphene layers is just to change the reflectivity of the air-SiO_2 interface, while they offer no significant optical depth. For large N, on the other hand, the reflectivity of the air-graphene interface saturates while the effect of the increasing optical path within the now thick graphite layer becomes significant. This change

is not a monotonic function of N. While these two effects are different, they both contribute to a shift of the reflectivity resonance condition, and thus explain the increasing visibility of thicker graphene layers, when measured for a fixed excitation energy.

In conclusion we showed that a single atomic layer can be visualized using elastic scattering microscopy due to interferometric enhancement of the signal. For a few layers (< 6), the contrast of the sample increases linearly with thickness indicating that the samples optically behave as a superposition of single sheets that act as independent two-dimensional electron gases. Thus, Rayleigh imaging is a general, simple, and quick tool to identify graphene layers.

Bibliography

[1] S. Iijima. Helical microtubules of graphitic carbon. *Nature*, 354:56–58, 1991.

[2] S. Iijima, T. Ichihashi. Single-shell carbon nanotubes of 1-nm diameter. *Nature*, 363:603–605, 1993.

[3] K. Hata, D. N. Futaba, K. Mizuno, T. Namai, M. Yumura, and S. Iijima. Water-assisted highly efficient synthesis of impurity-free single-walled carbon nanotubes. *Science*, 306:1362, 2004.

[4] A. Jorio, M. S. Dresselhaus, G. Dresselhaus, editor. *Carbon Nanotubes, Topics In Applied Physics (111)*. Springer, Berlin / Heidelberg, 2008.

[5] W. Lu, C. M. Lieber. Nanoelectronics from the bottom up. *Nat. Mater.*, 6:841, 2007.

[6] P. W. Barone, B. Seunghyun, D. A. Heller, M. S. Strano. Near-infrared optical sensors based on single-walled carbon nanotubes. *Nat. Mater.*, 4:86, 2004.

[7] T. K. Leeuw, R. M. Reith, R. A. Simonette, M. E. Harden, P. Cherukuri, D. A. Tsyboulski, K. M. Beckingham, R. B. Weisman. Single-walled carbon nanotubes in the intact organism: Near-ir imaging and biocompatibility studies in drosophila. *Nano Lett.*, 7:2650, 2007.

[8] F. Wang, G. Dukovic, L. E. Brus, T. F. Heinz. The optical resonances in carbon nanotubes arise from excitons. *Science*, 308:838–841, 2005.

[9] A. Hagen, M. Steiner, M. B. Raschke, C. Lienau, T. Hertel, H. Qian, A. J. Meixner, A. Hartschuh. Exponential decay lifetimes of excitons in individual single-walled carbon nanotubes. *Phys. Rev. Lett.*, 95:197401, 2005.

[10] S. Reich, C. Thomsen, J. Maultzsch. *Carbon Nanotubes*. Wiley-VCH, 2004.

[11] R. H. Baughman, A. A. Zakhidov, W. A. de Heer. Carbon nanotubesthe route toward applications. *Science*, 297:787, 2002.

[12] C. Casiraghi, A. Hartschuh, E. Lidorikis, H. Qian, H. Harutyunyan, T. Gokus, K. S. Novoselov, A. C. Ferrari. Rayleigh imaging of graphene and graphene layers. *Nano Lett.*, 7:2711, 2007.

[13] M.S. Dresselhaus, G. Dresselhaus, R. Saito, A. Jorio. Raman spectroscopy of carbon nanotubes. *Phys. Rep.*, 409:47, 2005.

[14] Y. Wu, J. Maultzsch, E. Knoesel, B. Chandra, M. Huang, M. Y. Sfeir, L. E. Brus, J. Hone, T. F. Heinz. Variable electron-phonon coupling in isolated metallic carbon nanotubes observed by raman scattering. *Phys. Rev. Lett.*, 99:027402, 2007.

[15] R. Saito, G. Dresselhaus, M. S. Dresselhaus. *Physical Properties of Carbon Nanotubes*. Imperial College Press (London), 1998.

[16] M. S. Dresselhaus, G. Dresselhaus, Ph. Avouris, editor. *Carbon Nanotubes: Synthesis, Structure, Properties and Applications*. Springer-Verlag Berlin Heidelberg, 2001.

[17] H. Kataura, Y. Kumazawa, Y. Maniwa, I. Umezu, S. Suzuki, Y. Ohtsuka, Y. Achiba. Optical properties of single-wall carbon nanotubes. *Synth. Met.*, 103:2555–2558, 1999.

[18] A. K. Geim, K. S. Novoselov. The rise of graphene. *Nat. Mater.*, 6:183, 2007.

[19] J. W. Mintmire, B. I. Dunlap, C. T. White. Are fullerene tubules metallic? *Phys. Rev. Lett.*, 68:631, 1992.

[20] X. Blase, L. X. Benedict, E. L. Shirley, S. G. Louie. Hybridization effects and metallicity in small radius carbon nanotubes. *Phys Rev. Lett.*, 72:1878, 1994.

[21] H. Qian, C. Georgi, N. Anderson, A. A. Green, M. C. Hersam, L. Novotny, A. Hartschuh. Exciton energy transfer in pairs of single-walled carbon nanotubes. *Nano Lett.*, 8:1363, 2008.

[22] P. H. Tan, A. G. Rozhin, T. Hasan, P. Hu, V. Scardaci, W. I. Milne, A. C. Ferrari. Photoluminescence spectroscopy of carbon nanotube bundles: Evidence for exciton energy transfer. *Phys Rev. Lett.*, 99:137402, 2007.

[23] M.J. O'Connell, S.M. Bachilo, C.B Huffman, V.C. Moore, M.S. Strano, B.H. Haroz, K.L Rialon, P.J. Boul, W.H. Noon, C. Kittrell, J.P. Ma, R. H. Hauge, R.B. Weisman, R.B Smalley. Band gap fluorescence from individual single-walled carbon nanotubes. *Science*, 297:593, 2002.

[24] S. M. Bachilo, M. S. Strano, C. Kittrell, R. H. Hauge, R. E. Smalley, R. B. Weisman. Structure-assigned optical spectra of single-walled carbon nanotubes. *Science*, 298:2361–2366, 2002.

[25] A. Hartschuh, H. N. Pedrosa, L. Novotny, T. D. Krauss. Simultaneous fluorescence and raman scattering from single carbon nanotubes. *Science*, 301:1354–1356, 2003.

[26] J. Lefebvre, Y. Homma, P. Finnie. Bright band gap photoluminescence from unprocessed single-walled carbon nanotubes. *Phys. Rev. Lett.*, 90:217401, 2003.

[27] J. Lefebvre, J. M. Fraser, P. Finnie, Y. Homma. Photoluminescence from an individual single-walled carbon nanotube. *Phys. Rev. B*, 69:075403, 2004.

[28] J. Lefebvre, D. G. Austin, J. Bond, P. Finnie. Photoluminescence imaging of suspended single-walled carbon nanotubes. *Nano Lett.*, 6:1603–1608, 2006.

[29] T. Ando. Excitons in carbon nanotubes. *J. Phys. Soc. Jpn.*, 66:1066–1073, 1997.

[30] C. D. Spataru, S. I. Beigi, L. X. Benedict, S. G. Louie. Excitonic effects and optical spectra of single-walled carbon nanotubes. *Phys. Rev. Lett.*, 92, 2004.

[31] V. Perebeinos, J. Tersoff, P. Avouris. Scaling of excitons in carbon nanotubes. *Phys. Rev. Lett.*, 92:257402, 2004.

[32] H. Zhao, S. Mazumdar. Electron-electron interaction effects on the optical excitations of semiconducting single-walled carbon nanotubes. *Phys Rev. Lett.*, 93:157402, 2004.

[33] M. S. Dresselhaus, G. Dresselhaus, R. Saito, A. Jorio. Exciton photophysics of carbon nanotubes. *Annu. Rev. Phys. Chem.*, 58:719, 2007.

[34] E. B. Barros, R. B. Capaz, A. Jorio, G. G. Samsonidze, A. G. Souza Filho, S. Ismail-Beigi, C. D. Spataru, S. G. Louie, G. Dresselhaus, M. S. Dresselhaus. Selection rules for one- and two-photon absorption by excitons in carbon nanotubes. *Phys. Rev. B*, 73:241406(R), 2006.

[35] R. S. Knox. *in Theory of Excitons, in Solid State Physics suppl. 5.* Academic Press, New York, 1963.

[36] M. Damnjanovic, T. Vukovic, I. Milosevic. Modified group projectors: tight-binding method. *J. Phys. A: Math. Gen.*, 33:6561, 2000.

[37] E. B. Wilson, J. C. Decius, and P. C. Cross. *Molecular Vibrations*. Dover, New York, 1980.

[38] E. B. Barros, A. Jorio, G. G. Samsonidze, R. B. Capaz, A. G. Souza Filho, J. Mendes Filho, G. Dresselhaus, M. S. Dresselhaus. Review on the symmetry-related properties of carbon nanotubes. *Phys. Rep.*, 431:261, 2006.

[39] V. Perebeinos, J. Tersoff, P. Avouris. Radiative lifetime of excitons in carbon nanotubes. *Nano Lett.*, 5:2495–2499, 2005.

[40] S. Tretiak. Triplet state absorption in carbon nanotubes: A td-dft study. *Nano Lett.*, 7:2201, 2007.

[41] E. Chang, D. Prezzi, A. Ruini, E. Molinari. Dark excitons in carbon nanotubes. *arXiv:cond-mat/0603085v1*, -.

[42] J. Maultzsch, R. Pomraenke, S. Reich, E. Chang, D. Prezzi, A. Ruini, E. Molinari, M. S. Strano, C. Thomsen, C. Lienau. Exciton binding energies in carbon nanotubes from two-photon photoluminescence. *Phys. Rev. B*, 72:241402(R), 2005.

[43] P. Y. Yu, M. Cardona. *Fundamentals of Semiconductors: Physics and Materials Properties*. Springer-Verlag Berlin Heidelberg, 2001.

[44] L. Luer, S. Hoseinkhani, D. Polli, J. Crochet, T. Hertel, G. Lanzani. Size and mobility of excitons in (6, 5) carbon nanotubes. *Nat. Phys.*, doi:10.1038/nphys1149, 2008.

[45] F. Wang, D. J. Cho, B. Kessler, J. Deslippe, P. J. Schuck, S. G. Louie, A. Zettl, T. F. Heinz, Y. R. Shen. Observation of excitons in one-dimensional metallic single-walled carbon nanotubes. *Phys Rev. Lett.*, 99:227401, 2007.

[46] J. Lefebvre, Paul Finnie. Excited excitonic states in single-walled carbon nanotubes. *Nano Lett.*, 8:1890, 2008.

[47] C. D. Spataru, S. Ismail-Beigi, R. B. Capaz, S. G. Louie. Theory and ab initio calculation of radiative lifetime of excitons in semiconducting carbon nanotubes. *Phys. Rev. Lett.*, 95:247402, 2005.

[48] H. Hirori, K. Matsuda, Y. Miyauchi, S. Maruyama, Y. Kanemitsu. Exciton localization of single-walled carbon nanotubes revealed by femtosecond excitation correlation spectroscopy. *Phys Rev. Lett.*, 97:257401, 2006.

[49] S. Berger, C. Voisin, G. Cassabois, C. Delalande, P. Roussignol. Temperature dependence of exciton recombination in semiconducting single-wall carbon nanotubes. *Nano Lett.*, 7:398–402, 2007.

[50] F. Wang, G. Dukovic, E. Knoesel, L. E. Brus, T. F. Heinz. Observation of rapid auger recombination in optically excited semiconducting carbon nanotubes. *Phys Rev. B*, 70:241403, 2004.

[51] Y. Z. Ma, L. Valkunas, S. L. Dexheimer, S. M. Bachilo, G. R. Fleming. Femtosecond spectroscopy of optical excitations in single-walled carbon nanotubes: Evidence for exciton-exciton annihilation. *Phys. Rev. Lett.*, 94:157402, 2005.

[52] L. Valkunas, Y.Z. Ma, G.R. Fleming. Exciton-exciton annihilation in single-walled carbon nanotubes. *Phys Rev. B*, 73:115432, 2006.

[53] J. S. Lauret, C. Voisin, G. Cassabois, C. Delalande, P. Roussignol, O. Jost, L. Capes. Ultrafast carrier dynamics in single-wall carbon nanotubes. *Phys. Rev. Lett.*, 90:057404, 2003.

[54] O. J. Korovyanko, C. X. Sheng, Z. V. Vardeny, A. B. Dalton, R. H. Baughman. Ultrafast spectroscopy of excitons in single-walled carbon nanotubes. *Phys. Rev. Lett.*, 92:017403, 2004.

[55] G.N Ostojic, S Zaric, J Kono, M.S. Strano, V.C. Moore, R.H. Hauge, R.B. Smalley. Interband recombination dynamics in resonantly excited

single-walled carbon nanotubes. *Physical Review Letters*, 92:117402, 2004.

[56] L. Huang, H. N. Pedrosa, T. D. Krauss. Ultrafast ground-state recovery of single-walled carbon nanotubes. *Phys. Rev. Lett.*, 93:017403, 2004.

[57] C. Manzoni, A. Gambetta, E. Menna, M. Meneghetti, G. Lanzani, G. Cerullo. Intersubband exciton relaxation dynamics in single-walled carbon nanotubes. *Phys. Rev. Lett.*, 94:207401, 2005.

[58] M. S. Arnold, S. I. Stupp, M. C. Hersam. Enrichment of single-walled carbon nanotubes by diameter in density gradients. *Nano Lett.*, 5:713–718, 2005.

[59] H. Y. Seferyan, M. B. Nasr, V. Senekerimyan, R. Zadoyan, P. Collins, V. A. Apkarian. Transient grating measurements of excitonic dynamics in single-walled carbon nanotubes: The dark excitonic bottleneck. *Nano Lett.*, 6:1757–1760, 2006.

[60] Z. Zhu, J. Crochet, M. S. Arnold, M. C. Hersam, H. Ulbricht, D. Resasco, T. Hertel. Pump-probe spectroscopy of exciton dynamics in (6,5) carbon nanotubes. *J. Phys. Chem. C*, 111:3831–3835, 2007.

[61] F. Wang, G. Dukovic, L. E. Brus, T. F. Heinz. Time-resolved fluorescence of carbon nanotubes and its implication for radiative lifetimes. *Phys Rev. Lett.*, 92:177401, 2004.

[62] T. Hertel, A. Hagen, V. Talalaev, K. Arnold, F. Hennrich, M. Kappes, S. Rosenthal, J. McBride, H. Ulbricht, E. Flahaut. Spectroscopy of single- and double-wall carbon nanotubes in different environments. *Nano Lett.*, 5:511–514, 2005.

[63] S. Reich, M. Dworzak, A. Hoffmann, C. Thomsen, M. S. Strano. Excited-state carrier lifetime in single-walled carbon nanotubes. *Phys. Rev. B*, 71:033402, 2005.

[64] M. Jones, W. K. Metzger, T. J. McDonald, C. Engtrakul, R. J. Ellingson, G. Rumbles, M. J. Heben. Extrinsic and intrinsic effects on the excited-state kinetics of single-walled carbon nanotubes. *Nano Lett.*, 7:300–306, 2007.

[65] L. Novotny and B. Hecht. *Principles of Nano-Optics*. Cambridge University Press, 2006.

[66] S. M. Bachilo, L. Balzano, J. E. Herrera, F. Pompeo, D. E. Resasco, R. B. Weisman. Narrow (n,m)-distribution of single-walled carbon nanotubes grown using a solid supported catalyst. *J. Am. Chem. Soc.*, 125:11186–11187, 2003.

[67] Y. Murakami, E. Einarsson, T. Edamura, S. Maruyama. Polarization dependence of the optical absorption of single-walled carbon nanotubes. *Phys. Rev. Lett.*, 94:087402, 2005.

[68] M. F. Islam, D. E. Milkie, C. L. Kane, A.G. Yodh, J.M. Kikkawa. Direct measurement of the polarized optical absorption cross section of single-wall carbon nanotubes. *Phys Rev. Lett.*, 93:037404, 2004.

[69] W. Becker. *The bh TCSPC Handbook*. Becker & Hickl GmbH, 2006.

[70] A. A. Green, M. C. Hersam. Ultracentrifugation of single-walled nanotubes. *Materials Today*, 10:59, 2007.

[71] M. S. Arnold, A. A. Green, J. F. Hulvat, S. I. Stupp, M. C. Hersam. Sorting carbon nanotubes by electronic structure using density differentiation. *Nat. Nanotech.*, 1:60–65, 2006.

[72] F. Hennrich, R. Krupke, K. Arnold, J. A. Rojas Sttz, S. Lebedkin, T. Koch, T. Schimmel, M. M. Kappes. The mechanism of cavitation-induced scission of single-walled carbon nanotubes. *J. Phys. Chem. B*, 111:1932, 2007.

[73] A. Hartschuh, H. N. Pedrosa, J. Peterson, L. Huang, P. Anger, H. Qian, A. J. Meixner, M. Steiner, L. Novotny, T. D. Krauss. Single carbon nanotube optical spectroscopy. *ChemPhysChem*, 6:577, 2005.

[74] A. Hartschuh, H. Qian, A. J. Meixner, N. Anderson, L. Novotny. Nanoscale optical imaging of excitons in single-walled carbon nanotubes. *Nano Lett.*, 5:2310–2313, 2005.

[75] F. Plentz, H. B. Ribeiro, A. Jorio, M. S. Strano, M. A. Pimenta. Direct experimental evidence of exciton-phonon bound states in carbon nanotubes. *Phys. Rev. Lett.*, 95:247401, 2005.

[76] V. Perebeinos, J. Tersoff, P. Avouris. Effect of exciton-phonon coupling in the calculated optical absorption of carbon nanotubes. *Phys. Rev. Lett.*, 94, 2005.

[77] H. Htoon, M. J. O'Conell, S. K. Doorn, V. I. Klimov. Single carbon nanotubes probed by photoluminescence excitation spectroscopy: The role of phonon-assisted transitions. *Phys Rev. Lett.*, 94:127403, 2005.

[78] X. Qiu, M. Freitag, V. Perebeinos, P. Avouris. Photoconductivity spectra of single-carbon nanotubes: Implications on the nature of their excited states. *Nano Lett.*, 5:749–752, 2005.

[79] O. Kiowski, S. Lebedkin, F. Hennrich, S. Malik, H. Rsner, K. Arnold, C. Sgers, M. M. Kappes. Photoluminescence microscopy of carbon nanotubes grown by chemical vapor deposition: Influence of external dielectric screening on optical transition energies. *Phys. Rev. B*, 75:075421, 2007.

[80] A. G. Walsh, A. N. Vamivakas, Y. Yin, S. B. Cronin, M. S. nl, B. B. Goldberg, A. K. Swan. Screening of excitons in single, suspended carbon nanotubes. *Nano Lett.*, 7:1485–1488, 2007.

[81] P. Finnie, Y. Homma, J. Lefebvre. Band-gap shift transition in the photoluminescence of single-walled carbon nanotubes. *Phys. Rev. Lett.*, 94:247401, 2005.

[82] H. Htoon, M. J. O'Connell, P. J. Cox, S. K. Doorn, V. I. Klimov. Low temperature emission spectra of individual single-walled carbon nanotubes: Multiplicity of subspecies within single-species nanotube ensembles. *Phys Rev. Lett.*, 93:027401, 2004.

[83] C. Galland, A. Hogele, H. E. Tureci, A. Imamoglu. Non-markovian decoherence of localized nanotube excitons by acoustic phonons. *Phys Rev. Lett.*, 101:067402, 2008.

[84] J. A. Misewich, R. Martel, P. Avouris, J. C. Tsang, S. Heinze, J. Tersoff. Electrically induced optical emission from a carbon nanotube fet. *Science*, 300:783, 2003.

[85] A. Hartschuh, E. J. Sanchez, X. S. Xie, L. Novotny. High-resolution near-field raman microscopy of single-walled carbon nanotubes. *Phys. Rev. Lett.*, 90:095503, 2003.

[86] J. Enderlein, R. Erdmann. Fast fitting of multi-exponential decay curves. *Opt. Commun.*, 134:371, 1997.

[87] J. Chen, V. Perebeinos, M. Freitag, J. Tsang, Q. Fu, J. Liu, P. Avouris. Bright infrared emission from electrically induced excitons in carbon nanotubes. *Science*, 310:1171, 2005.

[88] B. F. Habenicht, H. Kamisaka, K. Yamashita, O. V. Prezhdo. Ab initio study of vibrational dephasing of electronic excitations in semiconducting carbon nanotubes. *Nano Lett.*, 7:3260, 2007.

[89] V. Perebeinos, P. Avouris. Phonon and electronic nonradiative decay mechanisms of excitons in carbon nanotubes. *Phys. Rev. Lett.*, 101:057401, 2008.

[90] G. Zhou, Y. Kawazoe. Localized valence states characteristics and work function of single-walled carbon nanotubes: A first-principles study. *Phys. Rev. B*, 65:155422, 2002.

[91] J.C. Charlier, G.M. Rignanese. Electronic structure of carbon nanocones. *Phys. Rev. Lett.*, 86:5970–5973, 2001.

[92] A. De Vita, J.C Charlier, X. Blase, R. Car. Electronic structure at carbon nanotube tips. *Appl. Phys. A*, 68:283, 1999.

[93] J.C. Charlier, T.W. Ebbesen, P. Lambin. Structural and electronic properties of pentagon-heptagon pair defects in carbon nanotubes. *Phys. Rev. B*, 53:11108–11113, 1996.

[94] L. Cognet, D. A. Tsyboulski, J. D. R. Rocha, C. D. Doyle, J. M. Tour, R. B. Weisman. Stepwise quenching of exciton fluorescence in carbon nanotubes by single-molecule reactions. *Science*, 316:1465–1468, 2007.

[95] A. Rajan, M. S. Strano, D. A. Heller, T. Hertel, K. Schulten. Length-dependent optical effects in single walled carbon nanotubes. *J. Phys. Chem.*, 112:6211, 2008.

[96] S. Berciaud, L. Cognet, B. Lounis. Luminescence decay and the absorption cross section of individual single-walled carbon nanotubes. *Phys. Rev. Lett.*, 101:077402, 2008.

[97] J. Shaver, J. Kono, O. Portugall, V. Krstic, G. L. J. A. Rikken, Y. Miyauchi, S. Maruyama, V. Perebeinos. Magnetic brightening of carbon nanotube photoluminescence through symmetry breaking. *Nano Lett.*, 7:1851–1855, 2007.

[98] A. Srivastava, H. Htoon, V.I. Klimov, J. Kono. Direct observation of dark excitons in individual carbon nanotubes: Inhomogeneity in the exchange splitting. *Phys Rev. Lett.*, 101:087402, 2008.

[99] I. B. Mortimer, R. J. Nicholas. Role of bright and dark excitons in the temperature-dependent photoluminescence of carbon nanotubes. *Phys Rev. Lett.*, 98:027404, 2007.

[100] W. K. Metzger, T. J. McDonald, C. Engtrakul, J. L. Blackburn, G. D. Scholes, G. Rumbles, M. J. Heben. Temperature-dependent excitonic decay and multiple states in single-wall carbon nanotubes. *J. Phys. Chem. C*, 111:3601, 2007.

[101] O. Kiowski, K. Arnold, S. Lebedkin, F. Hennrich, M. M. Kappes. Direct observation of deep excitonic states in the photoluminescence spectra of single-walled carbon nanotubes. *Phys. Rev. Lett.*, 99:237402, 2007.

[102] H. Harutyunyan, T. Gokus, A. A. Green, M. C. Hersam, M. Allegrini, A. Hartschuh. Defect induced photoluminescence from dark excitonic states in individual single-walled carbon nanotubes. *arXiv:0812.1040v1*, 2008.

[103] T. Gokus, H. Harutyunyan, F. Hennrich, A. A. Green, M. C. Hersam, P. T. Araujo, M. Kappes, A. Jorio, M. Allegrini, A. Hartschuh. Exciton decay dynamics in individual carbon nanotubes at room temperature. *Appl. Phys. Lett.*, 92:153116, 2008.

[104] C. Georgi, N. Hartmann, T. Gokus, A. A. Green, M. C. Hersam, A. Hartschuh. Photo-induced luminescence blinking and bleaching in individual single-walled carbon nanotubes. *ChemPhysChem*, 9:1460, 2008.

[105] J. Lefebvre, P. Finnie, Y. Homma. Temperature-dependent photoluminescence from single-walled carbon nanotubes. *Phys. Rev. B*, 70:045419, 2004.

[106] K. Matsuda, T. Inoue, Y. Murakami, S. Maruyama, Y. Kanemitsu. Exciton dephasing and multiexciton recombinations in a single carbon nanotube. *Phys. Rev. B*, 77:033406, 2008.

[107] G. D. Scholes, S. Tretiak, T. J. McDonald, W. K. Metzger, C. Engtrakul, G. Rumbles, Michael J. Heben. Low-lying exciton states determine the photophysics of semiconducting single wall carbon nanotubes. *J. Phys. Chem. C*, 111:11139, 2007.

[108] H. Qian, P. T. Araujo, C. Georgi, T. Gokus, N. Hartmann, A. A. Green, A. Jorio, M. C. Hersam, L. Novotny, A. Hartschuh. Visualizing the local optical response of semiconducting carbon nanotubes to dna-wrapping. *Nano Lett.*, 8:2706, 2008.

[109] O. N. Torrens, M. Zheng, J. M. Kikkawa. Energy of k-momentum dark excitons in carbon nanotubes by optical spectroscopy. *Phys Rev. Lett.*, 101:157401, 2008.

[110] A. V. Krasheninnikov, A. S. Foster, R. M. Nieminen. Defect - mediated engeneering of the electron structure of carbon nanosystems. *NT08 Conference, Book of abstracts*, page 52, 2008.

[111] P.O. Lehtinen, A. V. Krasheninnikov, A.S. Foster, R.M. Nieminen. *Carbon Based Magnetism.* Elsevier, 2006.

[112] P.O. Lehtinen, A. S. Foster, A. Ayuela, A. Krasheninnikov, K. Nordlund, R.M. Nieminen. Magnetic properties and diffusion of adatoms on a graphene sheet. *Phys Rev. Lett.*, 91:017202, 2003.

[113] E. Durgun, S. Dag, S. Ciraci, O. Gulseren. Energetics and electronic structures of individual atoms adsorbed on carbon nanotubes. *J. Phys. Chem*, 108:575, 2004.

[114] A. E. Davies. The kinetics of the coagulation of gold sols. an investigation of the "thermo-senescence effect" exhibited at elevated temperatures. *J. Phys. Chem.*, 33:274, 1929.

[115] Y. Gan, L. Sun, F. Banhart. One- and two-dimensional diffusion of metal atoms in graphene. *Small*, 4:587, 2008.

[116] K.S. Novoselov, D. Jiang, F. Schedin, T.J. Booth, V.V. Khotkevich, S.V. Morozov, A.K. Geim. Two-dimensional atomic crystals. *Proc. Natl. Acad. Sci. U.S.A.*, 102:10451, 2005.

[117] K. S. Novoselov, A. K. Geim, S. V. Morozov, D. Jiang, Y. Zhang, S. V. Dubonos, I. V. Grigorieva, A. A. Firsov. Electric field effect in atomically thin carbon films. *Science*, 306:666, 2004.

[118] Y. B. Zhang, Y. W. Tan, H. L. Stormer, P. Kim. Experimental observation of the quantum hall effect and berry's phase in graphene. *Nature*, 438:201, 2005.

[119] K.S. Novoselov, A. K.Geim, S. V. Morozov, D. Jiang, M. I. Katsnelson, I. V. Grigorieva, S. V. Dubonos, A. A. Firsov. Two-dimensional gas of massless dirac fermions in graphene. *Nature*, 438:197, 2005.

[120] M. Y. Han, B. Ozyilmaz, Y. B. Zhang, P. Kim. Energy band-gap engineering of graphene nanoribbons. *Phys Rev. Lett.*, 98:206805, 2007.

[121] L. A. Ponomarenko, F. Schedin, M. I. Katsnelson, R. Yang, E. W.Hill, K. S. Novoselov, A. K. Geim. Chaotic dirac billiard in graphene quantum dots. *Science*, 320:356, 2008.

[122] Z. H. Chen, Y. M. Lin, M. J. Rooks, P. Avouris. Graphene nano-ribbon electronics. *Physica E*, 40:228, 2008.

[123] K. S. Novoselov, E. McCann, S.V. Morozov, V. I. Fal'ko, M.I. Katsnelson, U. Zeitler, D. Jiang, F. Schedin F, A.K. Geim. Unconventional quantum hall effect and berry's phase of 2 pi in bilayer graphene. *Nat. Phys.*, 2:177, 2006.

[124] Y. Hernandez, V. Nicolosi, M. Lotya, F. M. Blighe, Z. Sun, S. De, I. T. McGovern, B. Holland, M. Byrne, Y. K. Gun'ko, J. J. Boland, P. Nira, G. Duesberg, S. Krishnamurthy, R. Goodhue, J. Hutchison, V. Scardaci, A. C. Ferrari, J. N. Coleman. High-yield production of

graphene by liquid-phase exfoliation of graphite. *Nat. Nanotech.*, 3:563, 2008.

[125] C. Berger, Z. M. Song, X. B. Li, X. S. Wu, N. Brown, C. Naud, D. Mayou, T. B. Li, J. Hass, A. N. Marchenkov, E. H. Conrad, P. N. First, W. A. de Heer WA. Electronic confinement and coherence in patterned epitaxial graphene. *Science*, 312:1191, 2006.

[126] J. C. Meyer, A. K. Geim, M. I. Katsnelson, K. S. Novoselov, T. J. Booth, S. Roth. The structure of suspended graphene sheets. *Nature*, 446:60, 2007.

[127] A. C: Ferrari, J. C. Meyer, V. Scardaci, C. Casiraghi, M. Lazzeri, F. Mauri, S. Piscanec, D. Jiang, K. S. Novoselov, S. Roth, A. K. Geim. Raman spectrum of graphene and graphene layers. *Phys. Rev. Lett.*, 97:187401, 2006.

[128] K. Lindfors, T. Kalkbrenner, P.Stoller, V. Sandoghdar. Detection and spectroscopy of gold nanoparticles using supercontinuumwhite light confocal microscopy. *Phys. Rev. Lett.*, 93:037401, 2004.

[129] A. V. Failla, H. Qian, H. Qian, A. Hartschuh, A. J. Meixner. Orientational imaging of subwavelength au particles with higher order laser modes. *Nano Lett.*, 6:1374, 2006.

[130] F. V. Ignatovich, L. Novotny. Real-time and background-free detection of nanoscale particles. *Phys Rev. Lett.*, 96:013901, 2006.

[131] M. Y. Sfeir, F. Wang, L. Huang, C. C. Chuang, J. Hone, S. P. O'Brien, T. F. Heinz, L. E. Brus. Probing electronic transitions in individual carbon nanotubes by rayleigh scattering. *Science*, 306:1540, 2004.

[132] F. Wang, M. Y. Sfeir, L. Huang, X. M. H. Huang, Y. Wu, J. Kim, J. Hone, S. O'Brien, L. E. Brus, T. F. Heinz. Interactions between individual carbon nanotubes studied by rayleigh scattering spectroscopy. *Phys Rev. Lett.*, 96:167401, 2006.

[133] S. Schultz, D. R. Smith, J. J. Mock, D. A. Schultz. Single-target molecule detection with nonbleaching multicolor optical immunolabels. *Proc. Natl. Acad. Sci. U.S.A.*, 97:996, 2000.

[134] J. K. Ranka, R. S.Windeler, A. J. Stentz. Visible continuum generation in air-silica microstructure optical fibers with anomalous dispersion at 800 nm. *Opt. Lett.*, 25:25, 2000.

[135] M. Born, E. Wolf. *Principles of Optics.* Pergamon Press, 1959.

Publications

Journal Articles

H. Harutyunyan, T. Gokus, A. A. Green, M. C. Hersam, M. Allegrini, A. Hartschuh, "Defect induced photoluminescence from dark excitonic states in individual single-walled carbon nanotubes", arXiv:0812.1040v1, (2008).

T. Gokus, A. Hartschuh, H. Harutyunyan, M. Allegrini, F. Hennrich, M. Kappes, A. A. Green, M. C. Hersam, P. T. Araujo, A. Jorio, "Exciton decay dynamics in individual carbon nanotubes at room temperature", *Appl. Phys. Lett.* **92**, 153116 (2008).

S. Mackowski, S. Woermke, A. J. Maier, T. H. P. Brotosudarmo, H. Harutyunyan, A. Hartschuh, A. O. Govorov, H. Scheer, C. Brauchle, "Metal - enhanced fluorescence of chlorophylls in single light - harvesting complexes", *Nano Lett.*, **8**, 558, 2008.

C. Casiraghi, A. Hartschuh, E. Lidorikis, H. Qian, H. Harutyunyan, T. Gokus, K. S. Novoselov, A. C. Ferrari, "Rayleigh Imaging of Graphene and Graphene Layers", *Nano Lett.* **7**, 2711 (2007).

T.S. Kurtikyan, H. A. Harutyunyan, R. K. Ghazaryan and J. A. Goodwin, "Spectral study of the nitrogen monoxide interaction with sublimed layers of meso-mono-4-pyridyl-tri-phenyl- and meso-mono-3-pyridyl-tri-phenyl-porphyrinatocobalt(II) ", *J. Porphyrins Phthalocyanines*, **10**, 971 (2006).

Conference Presentations

H. Harutyunyan, T. Gokus, A. A. Green, M. C. Hersam, M. Allegrini, A. Hartschuh, "Photoluminescence from Low Lying Excitonic States in Individual Single-Walled Carbon Nanotubes Mediated by Localized Defects", Proc. of the XXIIIth Intern. Winterschool on Electronic Properties of Novel Materials, Kirchberg, Austria, Mar. 2009.

H. Harutyunyan, T. Gokus, F. Hennrich, A. A. Green, M. C. Hersam, P. T. Araujo, M. Kappes, A. Jorio, M. Allegrini, A. Hartschuh, "Exciton decay dynamics in individual carbon nanotubes at room temperature", NT08, Montpellier, France, Jul. 2008. *Contibuted talk.*

A. Hartschuh, H. Qian, C. Georgi, H. Harutyunyan, T. Gokus, M. C. Hersam, F. Hennrich, L. Novotny, "Exciton Dynamics, Localization and Transfer in Single Carbon Nanotubes", IWEPNM 2008, Kirchberg, Austria, Mar. 2008.

T. Gokus, H. Harutyunyan, F. Hennrich, M. Kappes, A. Hartschuh, "Time-resolved photoluminescence studies on individual single– walled carbon nanotubes", DFG Spring meeting, Berlin, Feb. 2008.

T. Gokus, H. Harutyunyan, A. Hartschuh, M. S. Arnold, M. C. Hersam, "Time-resolved photoluminescence from excitons in individual carbon nanotubes", NT07, Ouro Preto, Brazil, Jun. 2007.

C.Casiraghi, A. Hartschuh, E. Lidorikis, H. Qian, H. Harutyunyan, T. Gokus, K. S. Novoselov, A. C. Ferrari, "Rayleigh Imaging of Graphene and Graphene layers", NT07, Ouro Preto, Brazil, Jun. 2007.

A. Hartschuh, H. Qian, C. Georgi, T. Gokus, H. Haratyunyan, N. Anderson, L. Novotny, "Metrology of Carbon Nanotubes using Near-field Optical Spectroscopy", MSIN, Rio de Janeiro, Brazil, Jun. 2007.